Technical Memorandum No. 33-218

Lunar and Planetary X-Ray Diffraction Program

Progress Report of
Research and Instrument Development
July 1964 to March 1965

COINVESTIGATORS

H. H. Hess   R. C. Speed

Princeton University   Jet Propulsion Laboratory

jpl
JET PROPULSION LABORATORY
CALIFORNIA INSTITUTE OF TECHNOLOGY
PASADENA, CALIFORNIA
June 1, 1965

Technical Memorandum No. 33-218

Lunar and Planetary X-Ray Diffraction Program

Progress Report of
Research and Instrument Development
July 1964 to March 1965

COINVESTIGATORS

H. H. Hess   **R. C. Speed**

Princeton University   Jet Propulsion Laboratory

Edited by
R. C. Speed
J. A. Dunne
D. B. Nash

R. V. Meghreblian, Manager
Space Sciences Division

FOREWORD

This Report presents 21 papers which summarize scientific research and instrument development during the interval from July 1, 1964 to March 1, 1965, in the Lunar and Planetary X-Ray Diffraction Program at the Jet Propulsion Laboratory. The objectives and scope of this program are outlined in a proposal dated July 1, 1964, to the National Aeronautics and Space Administration by H. H. Hess of Princeton University and R. C. Speed of the Jet Propulsion Laboratory of the California Institute of Technology. The work by the JPL staff has been done under NASA Contract No. NAS 7-100. Research in this program at Princeton University, under Contract No. NSG 6-57, has been recorded elsewhere, chiefly in semiannual reports by H. H. Hess and G. Otálora. Dr. Otálora, however, has included a paper in this collection, and his contribution is gratefully acknowledged.

CONTENTS

CONTENTS (Cont'd)

I. INTRODUCTION

A. PROGRAM DEFINITION AND OBJECTIVES

The Lunar and Planetary X-Ray Diffraction Program consists of three concurrent efforts aimed at rapid development of a first-generation flight-instrument system, evaluation of potential advances in diffractometer components for a possible second-generation instrument, and full investigation of the capabilities and limitations of rock analysis by X-ray diffraction. More complete descriptions of each of these studies are given below; the papers which follow are grouped according to these subjects in Sections II through V.

B. CONCURRENT STUDIES

1. Mark 1 X-Ray Diffraction System

a. Mark 1 Diffractometer. The Mark 1 diffractometer is a modification of the instrument initially intended for Surveyor I; the original instrument was designed by Dr. W. Parrish[1] and was constructed by Philips Laboratories. The device consists of a conventional Bragg-Brentano geometry of reduced dimension, compared with usual laboratory instruments. The source is a miniaturized X-ray tube used with a proportional gas detector.

The goal of this portion of the program is to provide a flightworthy diffraction system in minimum time. To achieve this aim, efforts are directed toward redesign, fabrication, and testing of mechanisms and electronics so as to cause only minor change in optics. Parametric performance and environmental testing of the source, optical elements, detectors, and alignment are under way.

b. Mark 1 Sampler. The Mark 1 sampler is a subsystem designed to provide the diffractometer with satisfactorily selected and prepared rock samples. It will be capable of acquiring multiple samples of either surface dust or solid bedrock, or of bedrock beneath an overlayer of shallow dust. Functions of the device include simultaneous penetration and pulverization of solid rock, acquisition of bedrock powder and of natural particulate material, transportation of the acquired material to the diffractometer, then transfer of a portion of that material into position for diffraction analysis. The sampler will form an integral part of the diffractometer system. Several design schemes are being considered, and tests have been carried out with breadboard components; fabrication of three complete breadboard samplers, each of which will test different sampler concepts, is now under way.

The results and the conclusions derived from this study are presented in Section III.

2. Advanced Diffractometer Studies

The objective of this second part of the program is to generate a fund of knowledge concerning the performance characteristics and general engineering parameters of possible diffractometer configurations and, as appropriate, of ancillary instrumentation. The essential goal is the definition of engineering breakpoints as

---

[1] Philips Laboratories, Irvington-on-Hudson, New York, Division of North American Philips Co., Inc., New York City.

determined by the performance parameters that are required for the solution of given class of petrologic problems. In addition to consideration of well established techniques, investigation includes advances in the state of the art which show particular potential. Scientific objectives of the advanced diffractometer study interface strongly with the data-interpretation study.

3. Data-Interpretation Studies

This study is aimed at full evaluation of the extent to which rocks can be analyzed both by X-ray diffraction data, alone, and by diffraction plus partial X-ray spectra. Conclusions from the investigations will provide a background for interpretation of lunar and planetary diffraction data and, conversely, will indicate the optimum combination of diffractometer optics and operating mode for any given petrological goal.

II. MARK 1 X-RAY DIFFRACTOMETER

A. HIGH-VOLTAGE POWER-SUPPLY DESIGN

D. Spreng and A. C. Dunk

Many problems in the development of a lunar X-ray diffractometer have no parallel in the history of conventional laboratory diffraction instrumentation. These problems result largely from the very different environment in which the device must operate and from the limitations in extensive parameters imposed by the spacecraft. One critical problem of the lunar diffraction system is the efficient production of a high flux of primary X-rays.

The general requirements for a power supply for this X-ray source are the following:

1. The output voltage should be 25,000 V ±1%.

2. The anode current to the X-ray tube should be 1 mA ±0.1% under all operating conditions.

3. The high voltage must not arc under any combinations of environmental temperatures and pressures encountered during launch or space flight.

4. All high-voltage circuitry should be shielded for RF interference.

In addition to the above requirements, other design goals were established, which include the following:

1. The power conversion efficiency should be as high as possible, preferably above 80%.

2. The power supply package should be as small and as lightweight as possible.

3. Since long life, high reliability, and small size are of utmost importance, integrated circuitry should be used where applicable.

To eliminate the possibility of arcing and the need for high-voltage cabling and connectors, it was decided to integrate all the circuitry and the X-ray tube in a single hermetically sealed, oil-insulated unit. The unit has a bellows to permit the oil to expand or contract without producing a region devoid of oil. Figures 1 and 2 are views of the assembled power supply and of the circuit diagram, respectively.

The design shown has not been optimized for weight, size, or for power dissipation; however, a prototype unit is being fabricated and will be tested to demonstrate the feasibility of this approach to packaging a high-voltage power supply for a space mission.
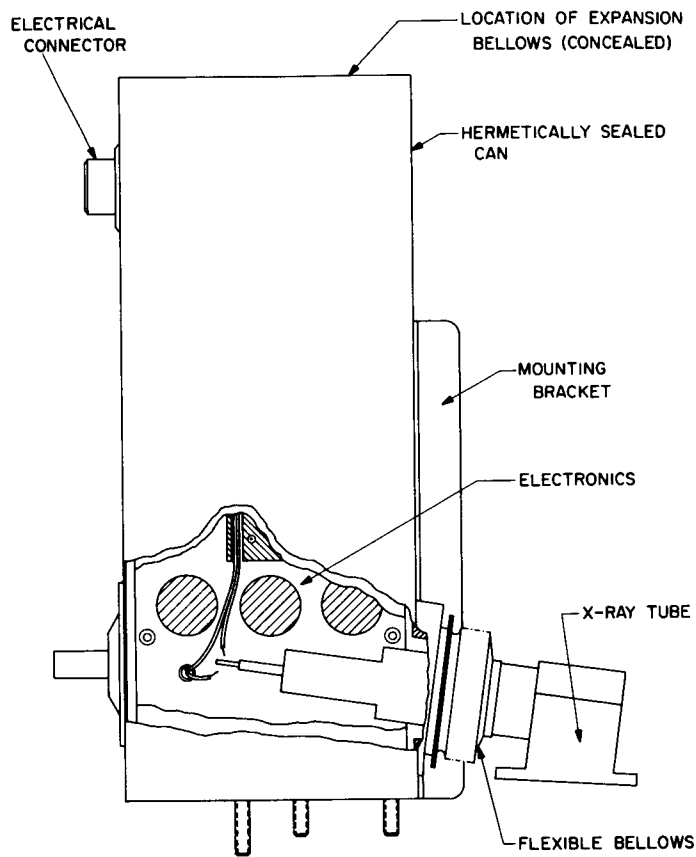
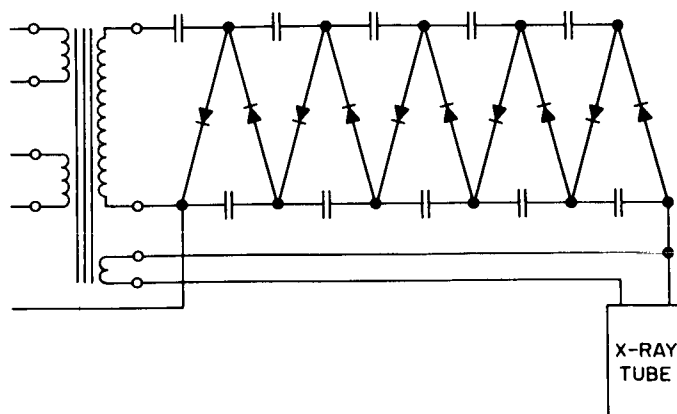Fig. 1.   High-voltage power-supply assembly

Fig. 2.   High-voltage power-supply
and circuit diagram

The X-ray tube is connected through a bellows to the power supply to eliminate the need for cables and connectors. The bellows will provide the capability for adjusting the alignment of the X-ray focus relative to the goniometer and will permit relative movement of the X-ray tube and power-supply components that are caused by temperature changes.

It was decided at the start that an attempt should be made to combine the filament and high-voltage transformers in order to save weight, cut bulk, and facilitate integration of the supply into a unit package. This approach, however, requires that some means of current regulation other than class A control of inverter input voltage must be used. The obvious choice is some form of pulse-width control, which allows the rms-responding filament temperature to be varied almost independently of the peak-sensitive rectifier-multiplier output. Figure 3 shows the idealized waveforms of the pulse duration modulation scheme. Figure 4 shows the block diagram of the entire high-voltage supply.

In order to use pulse-width control, the high-voltage transformer must be driven by a power amplifier instead of by a self-oscillating inverter. As an added benefit, this arrangement allows some power saving because it does not permit the transformer to saturate. The transformer is of special design, with the secondary pi wound to minimize interwinding and interturn capacity. This reduction of capacity allows faster switching and, therefore, results in greater efficiency. The rise-time of the waveform across the primary [Fig. 3(d)] is 500 nsec. The fall time is very slow (25 μsec), since the switching transistor is turned off prematurely and the transformer core is allowed to demagnetize naturally. Because the transistor is off during this fall time it does not contribute to power loss. The power amplifier transistors are transformer-driven for optimum impedance match; therefore, there is optimum power transfer and minimum loss. The preamp transistors are driven by an integrated circuit buffer amplifier. The on-off command, biphase drive, and pulse-width modulator output are mixed in an integrated circuit dual NOR gate. When an on command is received, the gate is unclamped and the power amplifier receives a square wave which initially has a high duty cycle (width) [Fig. 3(d)]. As the anode current starts to build up to 1 mA, the duty cycle approaches 50%. The duty cycle continues to lower as the anode current passes 1 mA. The device that translates anode current to pulse width is the pulse duration modulator. The modulator consists of three parts: the integrator, which changes the square wave clock input to a triangular wave; the preamplifier, which amplifies the error voltage derived from the

(a) CLOCK INPUT
8192 cps

(b) BIPHASE DRIVER
4096 cps

(c) PDM OUTPUT

(d) HIGH-VOLTAGE
TRANSFORMER PRIMARY

ANODE CURRENT
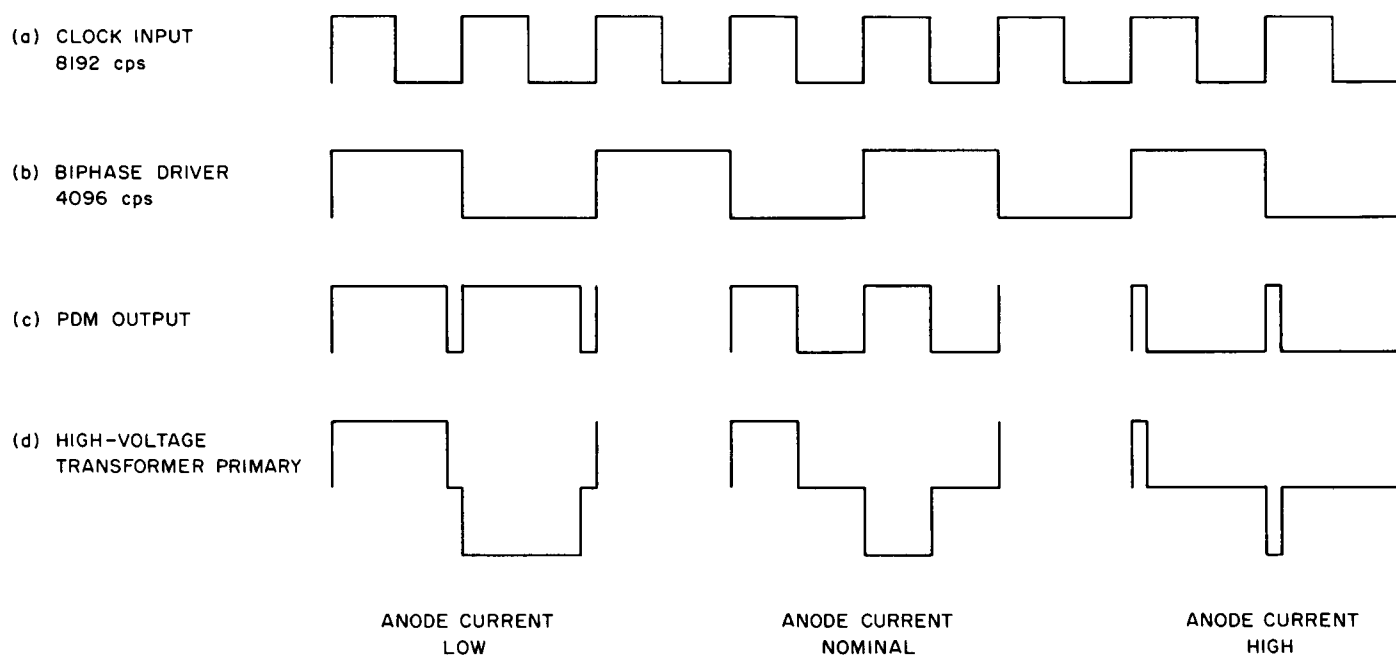LOW

ANODE CURRENT
NOMINAL

ANODE CURRENT
HIGH

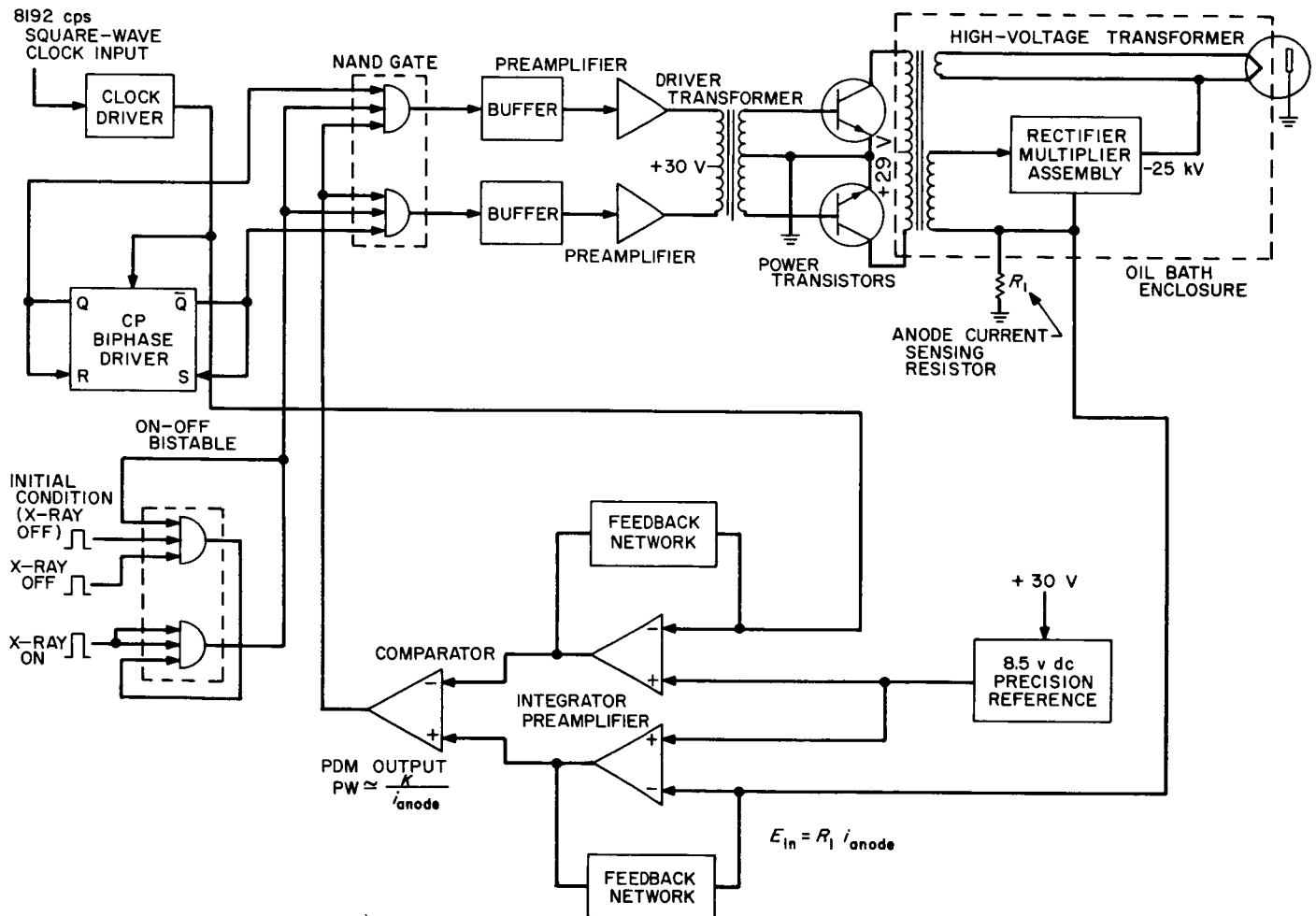Fig. 3. Idealized waveforms of 25-kV power supply

Fig. 4. Diagram of 25-kV power supply and regulator loop

comparison of the anode current to a precision reference voltage; and a comparator, which generates a square wave whose duty cycle is dependent upon the difference between the preamp dc level and the integrator peak voltage. The open-loop gain of the pulse duration modulation system is 4300 (see Table 1), which gives a 1 mA regulation accuracy of 0.023%.

Figure 5 shows the relationship between pulse-width duty cycle and anode current. Since the pulse-width duty cycle determines the rms voltage available across the filament, Fig. 5 can be considered a representation of the filament transfer function.

Figure 6 shows the performance of the anode current regulation system as a function of temperature. A total variation of 0.25% is observed over the range -50 to +100° C.

The free-air stud-temperature rise of the power transistors was measured. At a beginning room ambient of 85° F the high-voltage supply was operated for 1 hr at 1-mA anode current. The stud temperature of the transistors stabilized at 110° F, or at a rise of 25° F.

The conversion efficiency was measured as follows:

1. Total power consumed = 36.4 W (29 V at 1.25 A)

2. Transformer excitation only = 6.04 W (including power drop across transistors)

3. Filament power = 3.8 W (2 V rms at 1.9 A nominal for 1-mA anode current)

4. High-voltage power = 25.0 W (25 kV at 1 mA)

5. Efficiency = (filament power + anode power)/input power x 100 = (3.8 + 25)/36.4 x 100 = 79%

6. Total power lost = total power (anode power + filament power) = 7.6 W

This efficiency is short of the "better than 80%" goal, but there is still possibility of lowering the 6.04 W used to excite the transformer. In addition, work is needed on the selection of a more efficient lamination material than that which is presently used in the transformer.

Figure 7 is an oscilloscope trace showing the voltage and current waveforms of the high-voltage supply. The top trace is the voltage across one-half of the transformer primary with a vertical scale factor of 20 V/cm. The bottom trace is the current through the primary; here, the vertical scale is 2 A/cm. At the time the

Table 1. Open-loop gain calculations for the pulse duration modulator

Step	Assumptions and Calculations
1	Preamp gain = 100
2	Integrator E_{out} = 2 V P-P (triangular waveshape)
3	Therefore, a 2-V change in the preamp output results in a 100% duty-cycle change. Therefore, the input necessary to produce a duty-cycle change of 100% is 2 V/100, or 20 mV.
4	The change in current through the anode-current sensing resistor R_1 for a 20-mV change in voltage is: $$\frac{\Delta E_{in}}{R} = \frac{20 \times 10^{-3} \text{ V}}{8.5 \times 10^{3}\,\Omega} = 2.35 \times 10^{-6} \qquad A = 2.35\ \mu A$$
5	The slope of the X-ray tube transfer curve (Fig. 5) at 1 mA is nominally 10%/mA or, expressed as a function of preamp input voltage, the slope is 2 mV/mA. This represents a change in current through the anode current sensing resistor of 0.235 μA.
6	Therefore, the open-loop gain of the pulse duration modulation system is: $$\frac{10\%/mA}{0.235\ \mu A/mA} = \frac{\text{total anode-current change}}{\text{input change required to effect change}} = \frac{1\text{ mA}}{0.235\ \mu A}$$ $$\frac{1 \times 10^{-3}}{0.235 \times 10^{-6}} = 4300$$
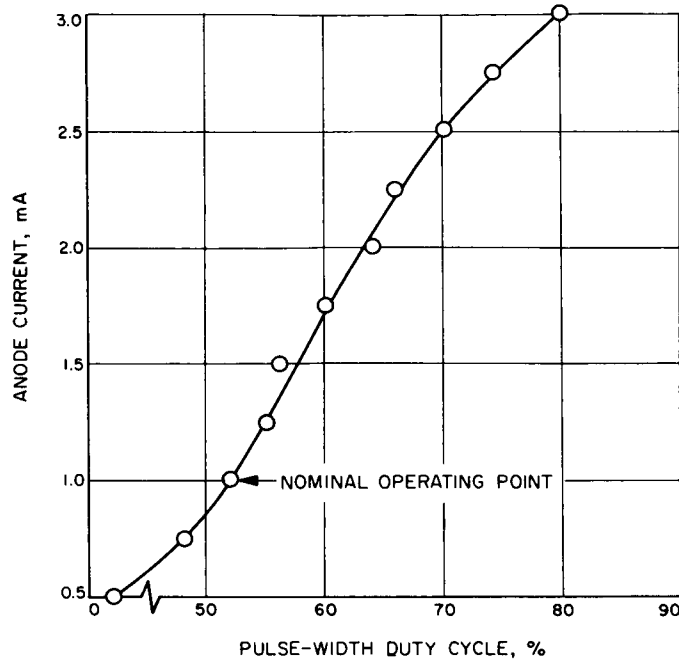
Fig. 5.   Pulse-width duty cycle vs
anode current (filament-transfer
function)
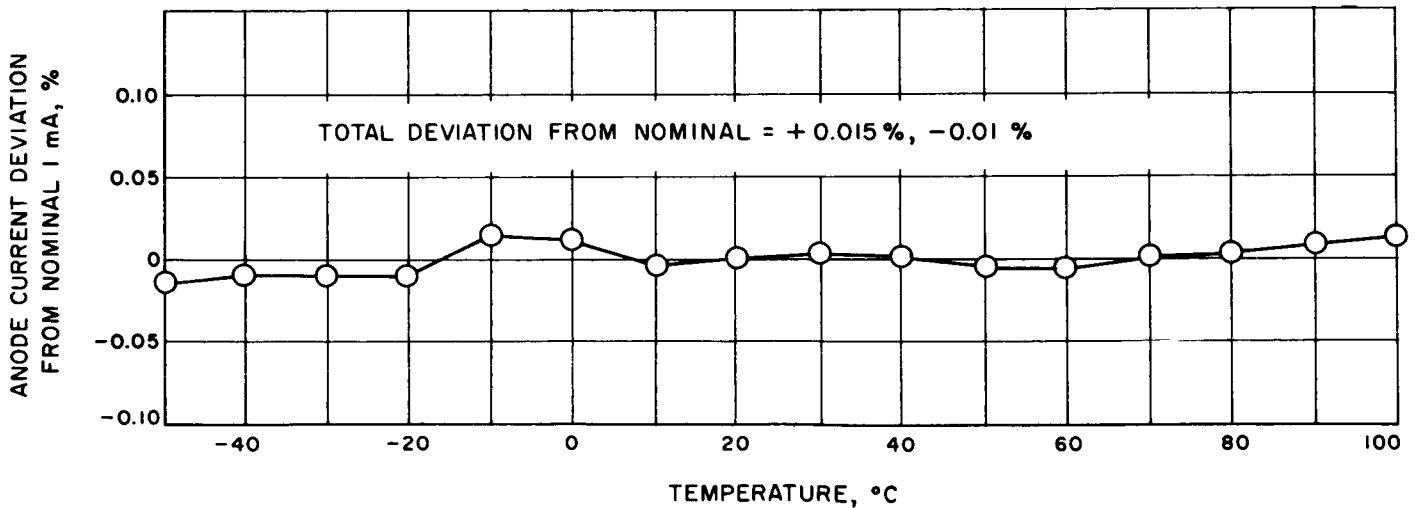
Fig. 6.   Results of temperature cycling of pulse-duration modulator
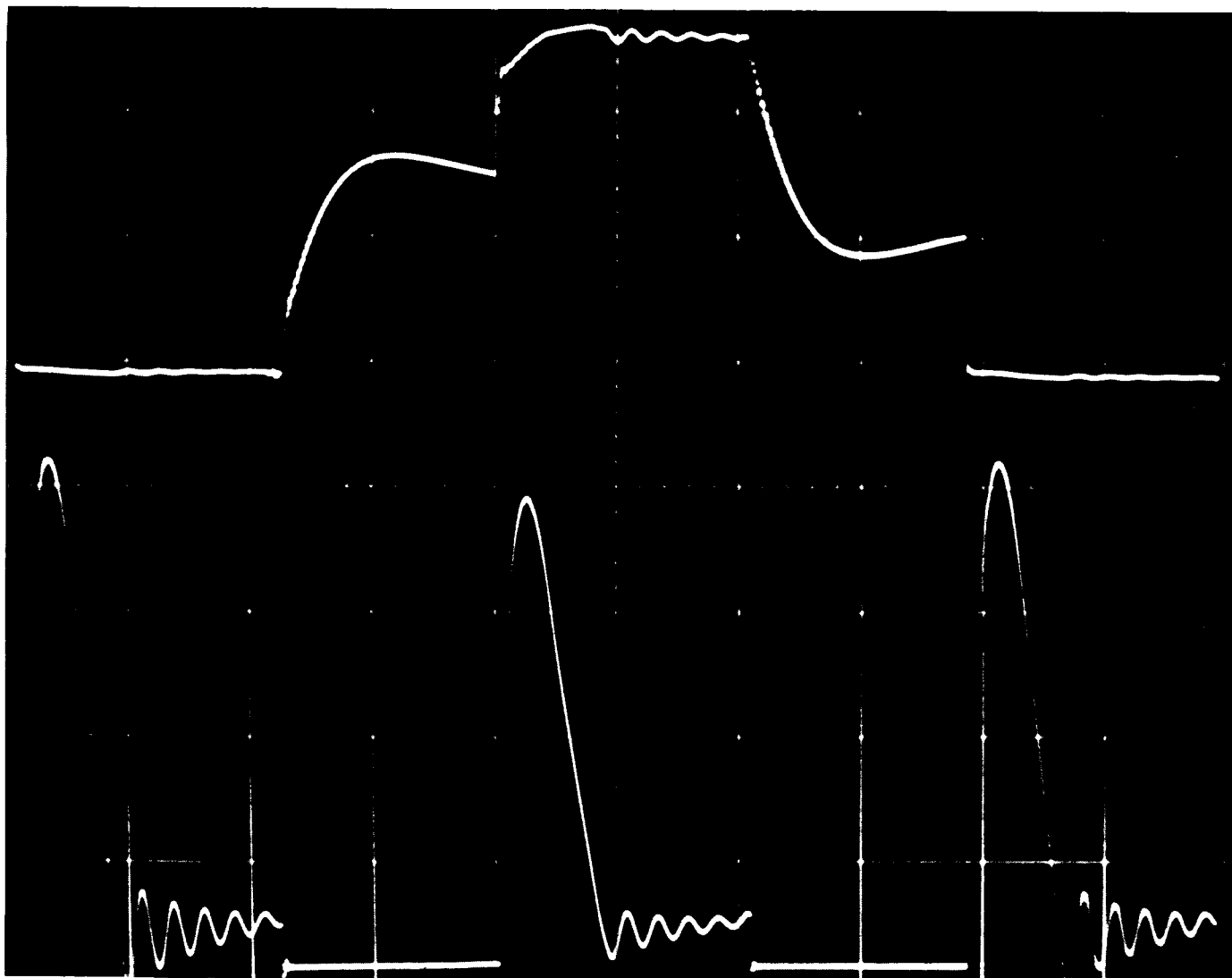
Fig. 7. Voltage and current waveforms of high-voltage supply

picture was taken, the supply was operating at 1 mA anode current with a pulse duration modulator duty cycle slightly greater than 50%. The large current spike is caused by the initial charging of the multiplier-block capacitors during each half-cycle.

In Fig. 8 a breadboard of the power supply immersed in oil is shown on the left, and the X-ray tube mounted on a breadboard diffractometer appears on the right. Each end of the high-voltage cable (at the points of connection) is immersed in oil. The cable is also shielded and grounded to bleed off the static charge.

Future effort will involve testing the above power supply in a simulated lunar environment; also, there will be further investigation of this method of packaging with various potting materials. Other high-voltage circuits will be designed in an attempt to increase the efficiency of the power supply and to reduce the size and weight of the unit.
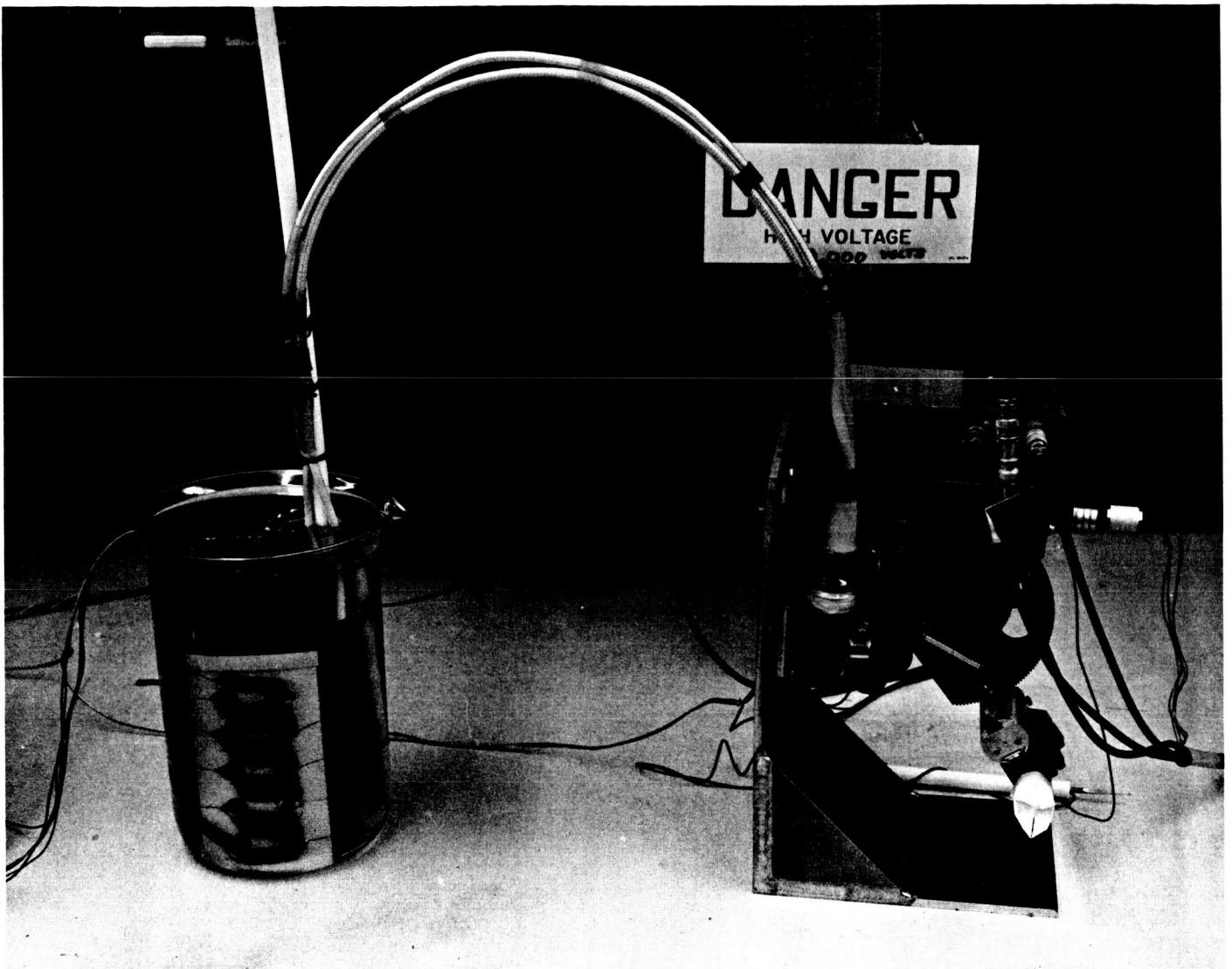
Fig. 8. Breadboard power supply immersed in oil

B. MARK 1 DIFFRACTOMETER ELECTRONICS

D. Spreng

The electronics equipment for the Mark 1 lunar X-ray diffractometer consists of three subsystems as shown in Fig. 1--power subsystems, motor-drive logic subsystem, and data-processing subsystem. The various power subsystems and the timing generator appear on the left side of the Figure. The power supply for the X-ray tube supplies 25 kV at 1 mA to the X-ray tube and 2.0 V rms at 1.9-A filament power. The counter-tube power supply generates the 2 kV necessary to operate the proportional detector. The low-voltage supply furnishes the power necessary to run the rest of the instrument electronics subsystems. The timing generator supplies the timing and gating functions for the entire instrument. The 8192-cps square wave is the clock frequency for the high-voltage supply. The 64-, 4-, and 0.8-cps frequencies, along with the scan-gate signal, are fed to the motor-drive logic subsystem. The data converters receive the scan gate signal and the 64-cps frequency signal.

The motor-drive logic subsystem is shown in the center of Fig. 1. Its function is to accept input commands from the spacecraft central computer and sequencer and to drive the goniometer stepper-motor in the appropriate direction at the correct speed. The motor is linked to the sample cup through the goniometer gear train. The logic system also acts in response to the internal automatic commands, such as the stop and the return-to-home functions.

The data-processing subsystem is illustrated on the right side of Fig. 1. It consists of the counter tube, preamp, pulse-height discriminator, and various telemetry processing mechanisms. The outputs of this subsystem go directly to the data automation system and are telemetered to Earth. The data processed by this subsystem include X-ray intensity, goniometer 2θ angle, and important engineering measurements--such as anode current, X-ray tube temperature, counter-tube temperature, and the scan-gate signal.

1. Scan Sequence and Data Handling

Three methods were considered for scanning and data handling for transmission. The first-described method of scanning and digital readout was chosen to obtain maximum data with minimum bandwidth. The diffractometer scans a total of 81.92 deg-2θ at a rate of 1 deg/125 sec. Each degree is divided into 100 discrete parts. Each time the stepper motor is pulsed, the goniometer advances 1/100 deg-2θ. The goniometer remains fixed at one position for 1.25 sec. The data converter
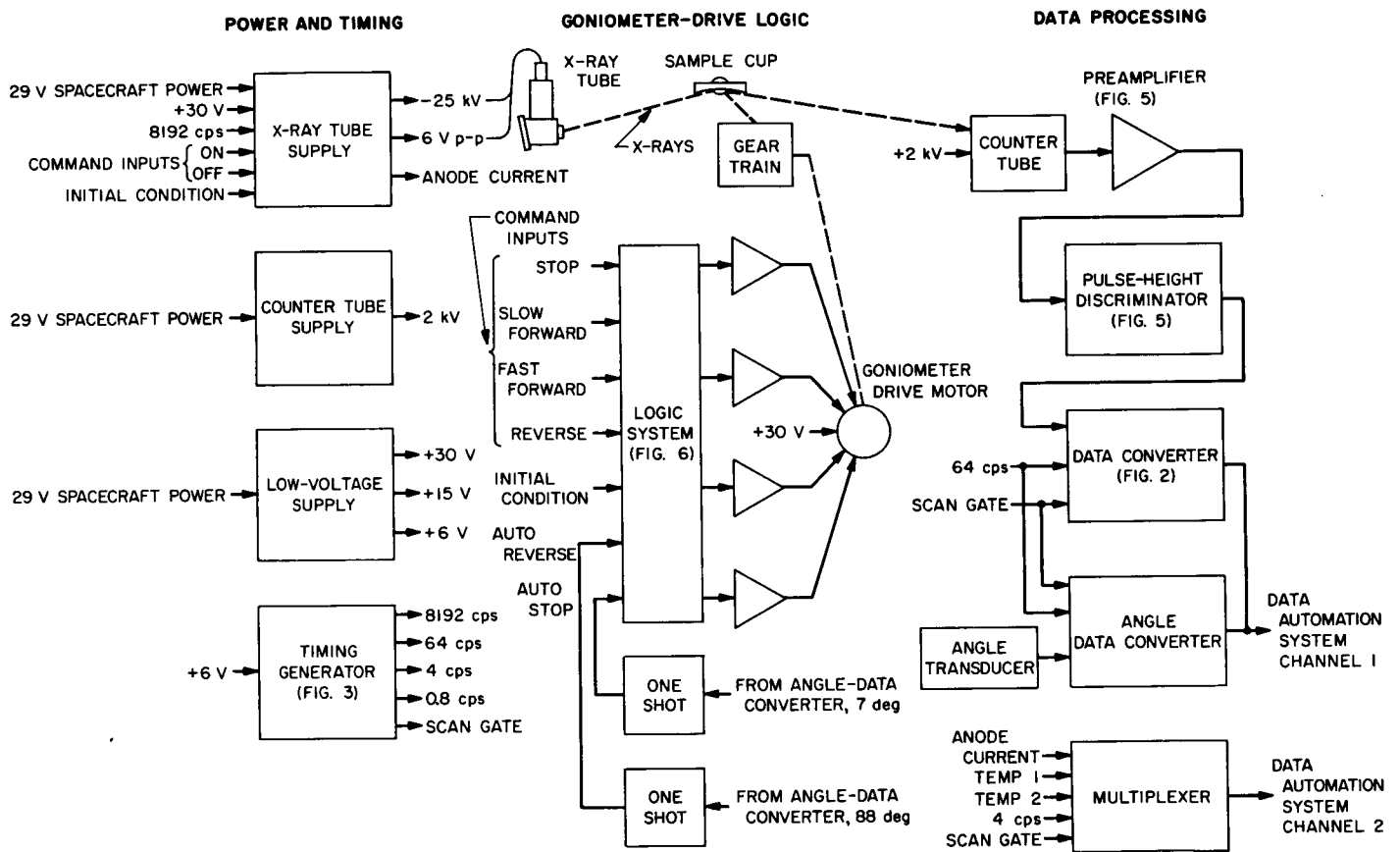
Fig. 1. Diffractometer-electronics block diagram

(Fig. 2) counts the number of pulses from the detector for 1.00 sec; the remaining 0.25 sec is spent reading out the count and advancing the goniometer the next increment. The time required for a complete scan is 170 min, 40 sec. The fast forward rate is 4 steps/sec, or 25 sec/deg, which is five times faster than slow forward. The reverse rate is 64 steps/sec; therefore, it would take 128 sec for the goniometer to return to home position. These rates are factors of the master-clock frequency of 8192 cps. The various rates are obtained by means of a binary countdown chain in the timing generator (Fig. 3).

In the second method described here, the first diffractometer prototype scanned continuously at a rate of 5.6 steps/sec (1/2 deg/min). The X-ray intensity was counted down by a factor of 8 and telemetered as a frequency-modulated square wave. The maximum count rate that has been obtained on the quartz(101) peak is approximately 5000 counts/sec; therefore, the maximum rate after the divide-by-8 chain would be 625 cps, requiring a 625-cps telemetry channel.

By comparison, the new digital system would return intensity data as a 13-bit binary word. Thirteen bits allow a maximum count of 8192 cps; since two bits are required to identify the word, the total length of the word is 15 bits. This word is sent during the 0.25-sec time lapse between counting periods, so the minimum bandwidth would be 15 half-cycles/0.25 sec (30 cps). This amount represents improvement in bandwidth requirements by a factor of 20 and allows an even larger number of words to be transmitted.

The third method would be to transmit continuously the full count, which may be as high as 5000 cps. The obvious disadvantage is the 5-kc-wide channel required for transmission, which may not be available.

The last-mentioned method would be the simplest to mechanize, followed by the continuous scan method and the digital method, in that order. The digital method, on the other hand, returns the most information for the smallest bandwidth. Figures 4, 5, and 6 are scans made on the Mark 1 lunar diffractometer that represent the three methods of data transmission. Figure 4 was made with the full-count approach; the scan in Fig. 5 was made with the divide-by-8 count method, and Fig. 6 was made with the digital method. Inspection of the three scans reveals no significant difference between the divide-by-8 scan and the full-count scan. This fact, combined with the relative simplicity of the divide-by-8 technique, suggests that, of the two, it would be preferable to use the latter method if adequate telemetry bandwidth is available.
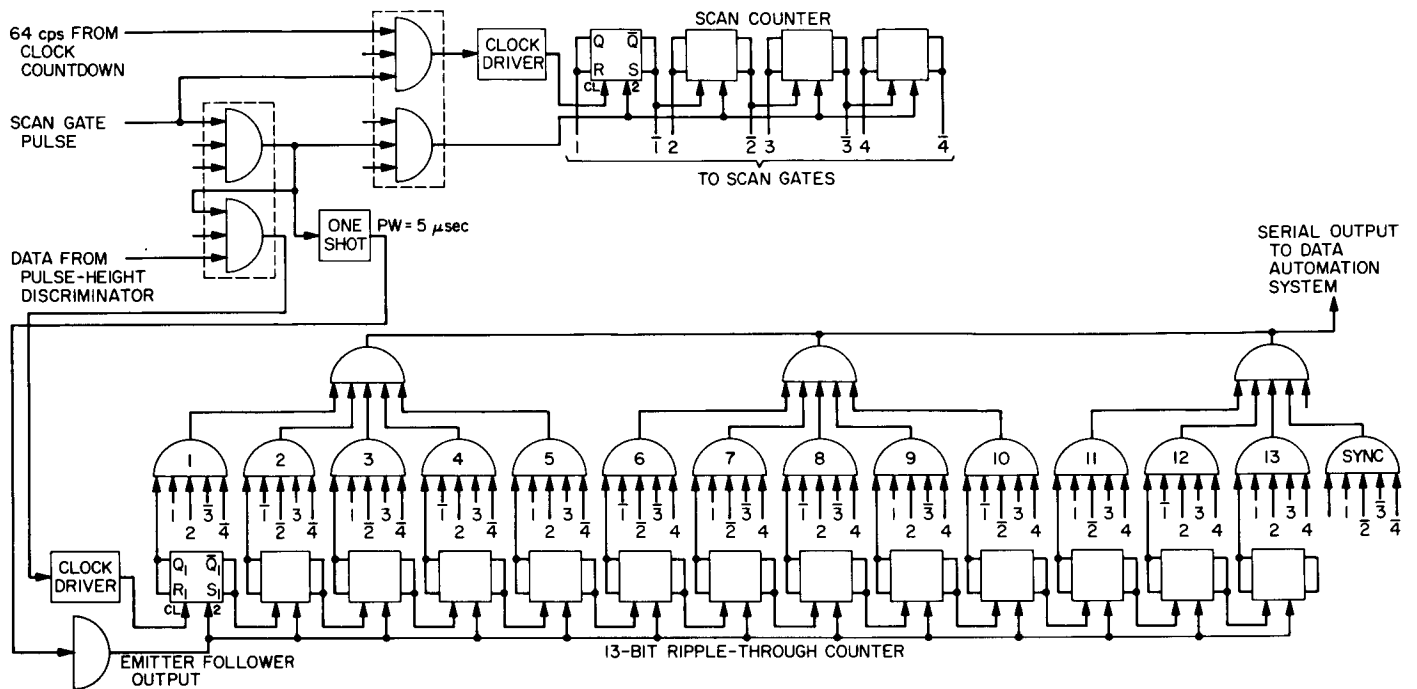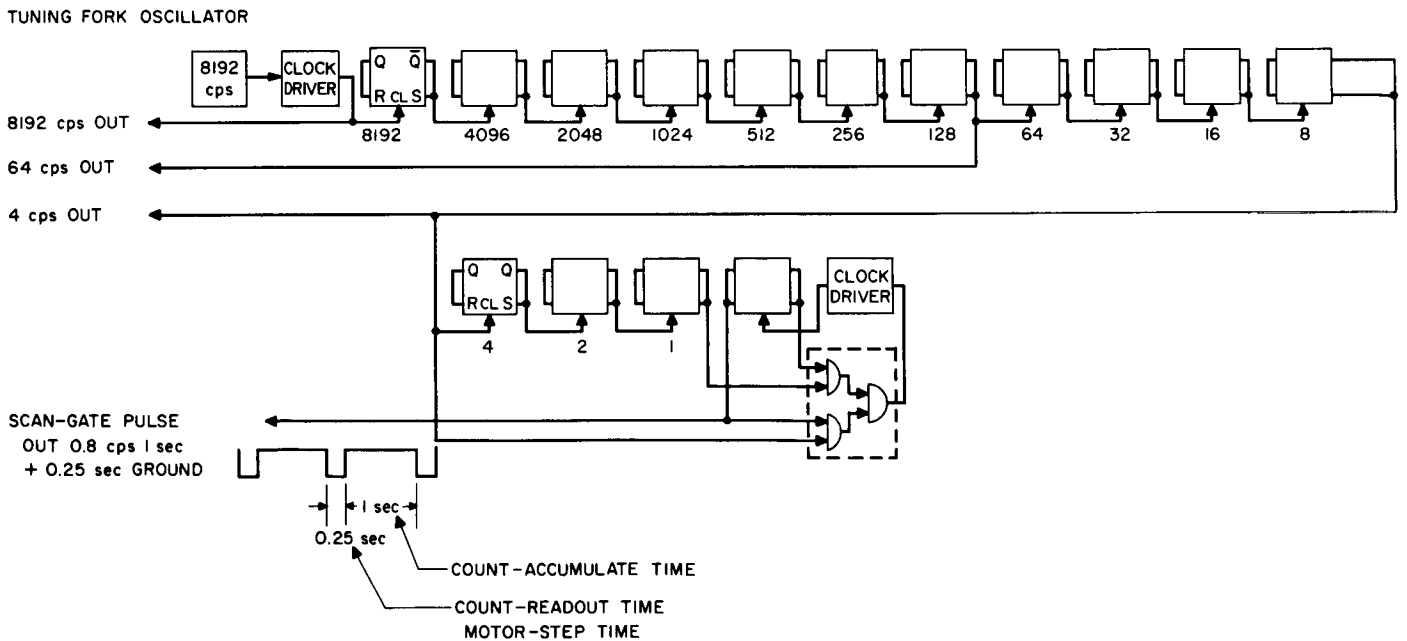
Fig. 2. Data-converter circuit diagram

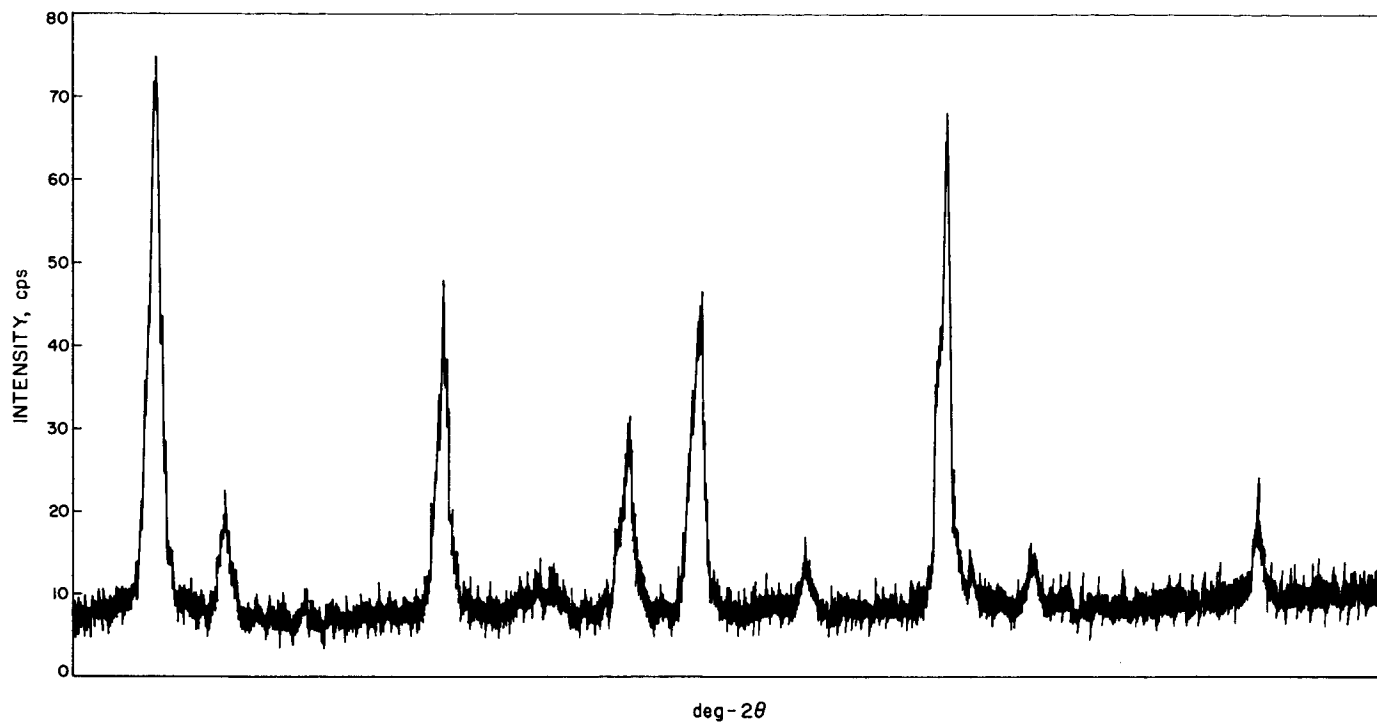Fig. 3. Timing-generator circuit diagram

Fig. 4. Diffractogram: full-scan count
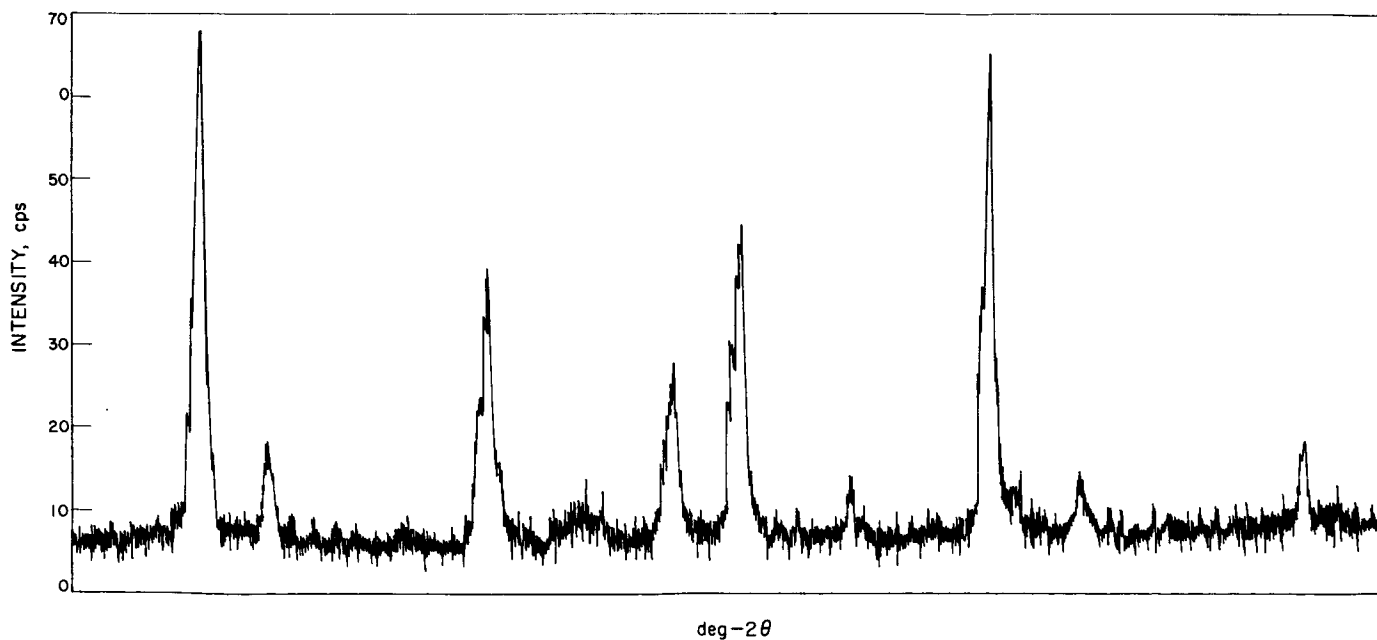
Fig. 5. Diffractogram: divide-by-8 scan
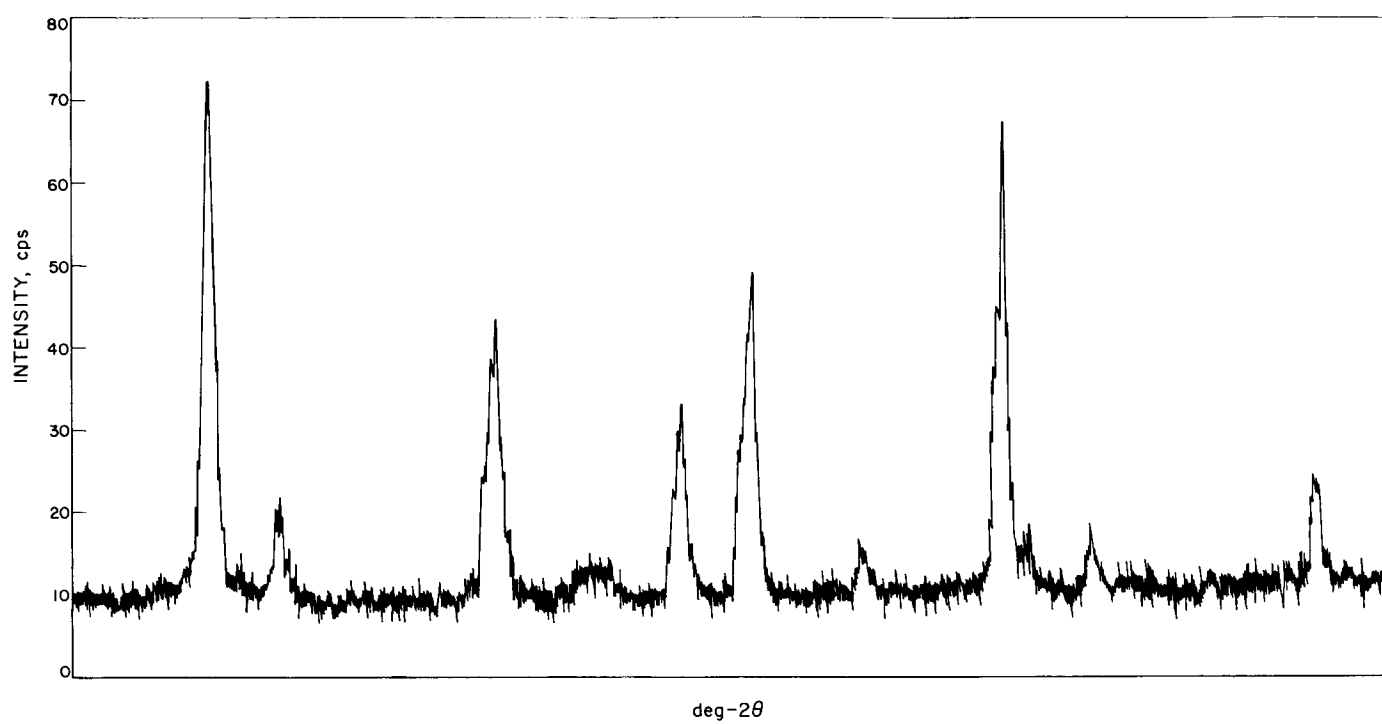
Fig. 6. Diffractogram: digital-step scan

A block diagram of the digital data converter is given in Fig. 2. The purpose of this device is to accumulate counts for 1 sec and, during the 1/4-sec period, to convert the total number into a binary word which is then telemetered to Earth. The converter consists of a 13-bit ripple-through counter sensed by NAND gates. During the counting period, the gates are inactive. Upon receipt of the scan signal from the timing generator, the scan counter starts and the data counter is inhibited by the lower NAND in the first SN514. The scan counter sequentially activates the gates, thereby sampling the data-counter outputs. In this manner, the parallel output of the counter is converted into a serial word starting with the two identification bits, then in sequence, the least significant bit through the most significant bit of the data word. The word appears as a changing voltage (NOR gate outputs) on the common output line which is fed to the spacecraft data automation system. A low voltage represents a one and a high voltage represents a zero. This may be seen in Fig. 7, the data-converter timing diagram.

At present, there are two basic methods under consideration for implementing the measurement of the goniometer 2θ angle. Both methods are digital in nature and will be mechanized with integrated circuits. The first entails mounting a digital shaft-angle encoder on the goniometer, which is coupled to the 2θ shaft. The output of the shaft encoder would be a 13-bit binary word expressing the angle to an accuracy of 0.01 deg-2θ. The output of the shaft-angle encoder is parallel in form, so it would be converted to serial form by an additional data converter, as shown in the system block diagram (Fig. 1). The number would be read into the data automation system between data scans while the data counter is counting for its 1-sec period. The alternate method would make use of an up-down counter (forward-reverse accumulator) which would count the number of voltage pulses fed to the stepper motor. This open-loop arrangement can provide an indication of shaft angle since the stepper motor output arm is mechanically linked to the goniometer through a gear train of precisely known reduction. The major source of error, assuming the system to be noise free, is the gear-train backlash which introduces a slight hysteresis between the measured and the actual angle. If the backlash can be kept to less than 0.01 deg, this error will be negligible. The up-down counter is similar to the data counter in that it consists of 13 bits, but unlike the data counter, it counts only one count per motor step. The counter has the capability of counting both up and down, so as the motor runs in reverse, the number will diminish back to zero as the goniometer runs to the home position. Like the data counter and the shaft encoder, the 13-bit word is
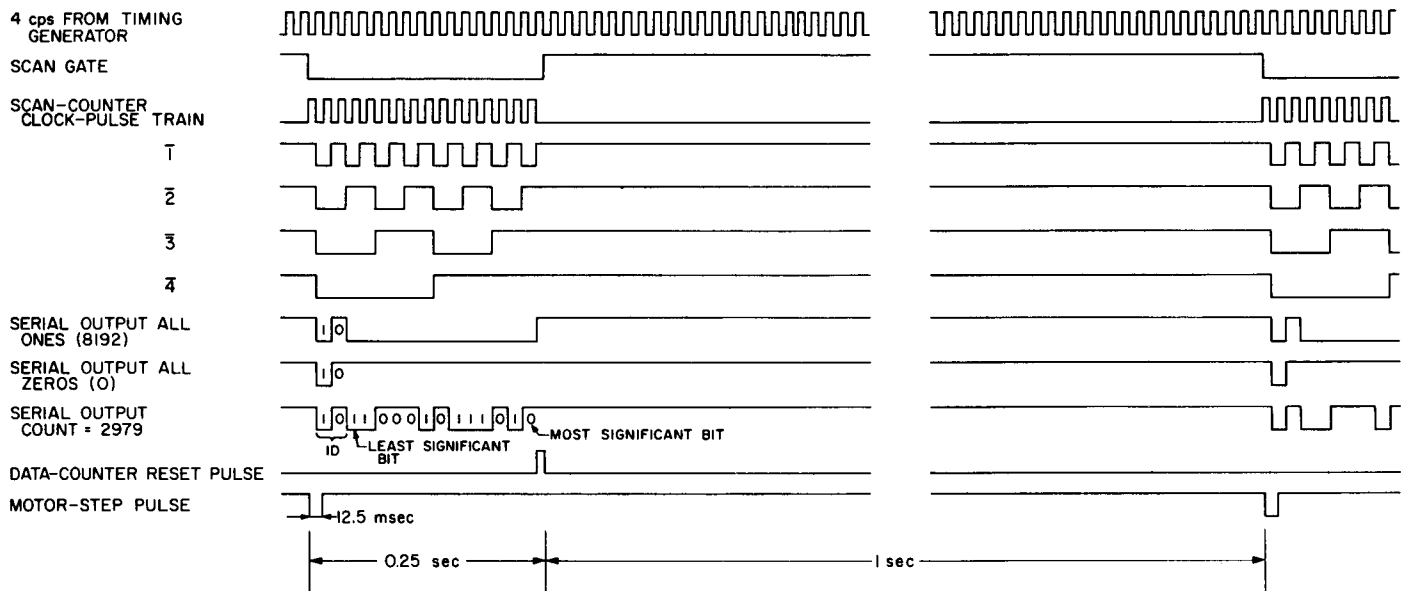
Fig. 7. Timing diagram for data converter

scanned and presented to the data automation system as a serial word. This operation occurs during the 1-sec data-counting period. The angle word is preceded by its own identification word consisting of two bits, similar to the two bits used to identify the data word; the angle ID-word consists of two ones, whereas the data ID-word consists of a one followed by a zero.

The anode current and temperature telemetry measurements may be time-division multiplexed and fed to a separate channel of telemetry. In the original Philips prototype, the second channel was used to transmit angle information, but since angle data is time-shared with diffraction data, this channel will become available for engineering measurements.

2. Proportional Preamplifier and Pulse Height Discriminator

The diffracted X-ray photons are detected in the proportional counter tube (Fig. 8), where they are converted to a small current pulse. This current pulse is applied to a two-stage integrated circuit amplifier where it is amplified to produce a voltage pulse sufficient to activate the pulse height discriminator.

The pulse height discriminator consists of two input comparators which compare the amplitude of the pulse to voltages that represent the threshold and window values required. If the pulse amplitude is less than the threshold voltage, neither comparator conducts. When the pulse amplitude is between the threshold and window references, only the threshold comparator conducts. As the pulse amplitude increases to a value that exceeds both the threshold and window values, both comparators conduct.

The output of the comparators is applied to a pair of output gates. The gates pass the pulse only if the threshold comparator is conducting. As the input pulse amplitude exceeds the window comparison voltage and the window comparator conducts, the gate is closed and no pulses pass through.

As in the case of the preamplifier, the pulse height discriminator is fabricated with integrated circuitry.

3. Motor-Drive Logic

Figure 9 is a block diagram of the motor-drive logic subsystem. Motor commands are inserted into the input memory. The memory has four stable states and will remain in the last stable state to which it was commanded until it receives a command representing one of the other possible stable states, at which time it will switch and remain until again commanded. Two of the commands are generated by sensors mounted on the goniometer. These commands are auto stop and auto reverse.
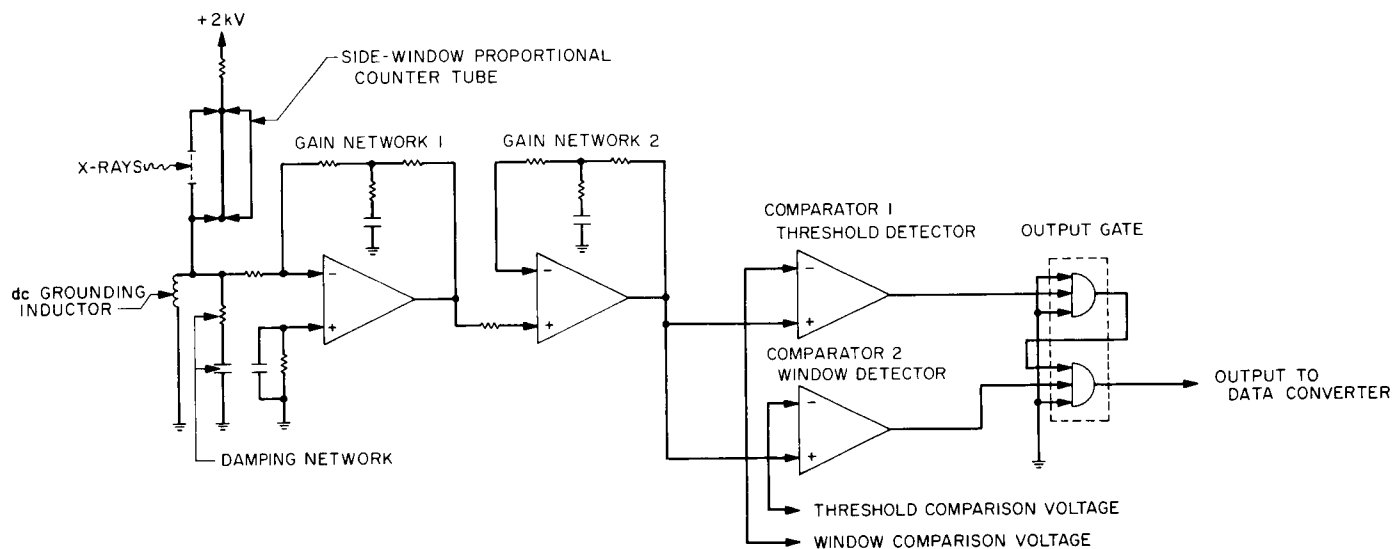
Fig. 8. Circuit diagram: proportional preamp and pulse-height discriminator
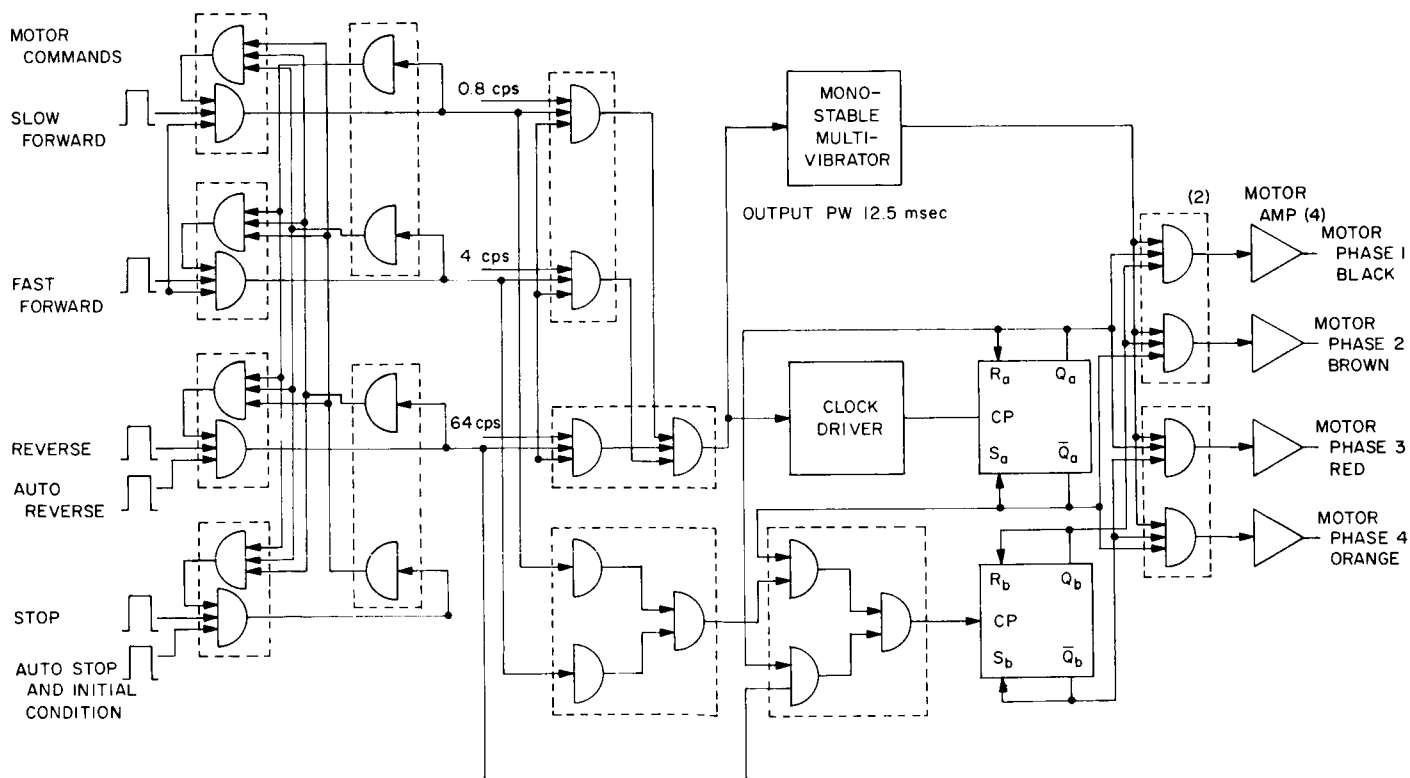
Fig. 9. Circuit diagram: motor-drive logic subsystem

Auto reverse is initiated upon completion of the 81.92 deg-2θ slow- or fast-forward goniometer sweep. The auto stop command occurs as the goniometer returns to the home position. The initial condition command is generated upon instrument turn-on and serves to keep the memory in the stop position.

The output of the memory is a low voltage for the commanded function and a high voltage for the remaining outputs. The memory outputs proceed to gates which also receive the appropriate rate of frequencies from the timing generator. In addition, the memory feeds gates which determine the rotational direction of the stepper motor. Rotational direction and rate information then feed a 4-bit up-down counter and a monostable multivibrator. The 4-bit up-down counter outputs, combined in gates with the pulse from the monostable multivibrator, then drive output amplifiers which apply power to step the motor. The purpose of the monostable multivibrator is to limit to 12.5 msec the time for which power is applied to the stepper motor. This time is sufficient to allow the motor to step; additional time merely wastes power.

C. DIFFRACTION PROFILES PRODUCED BY BERYLLIUM-WINDOW SAMPLE CUPS

N. Nickle

In general, beryllium-window sample cups produce a typical diffraction profile with the same peaks appearing for each cup (Fig. 1). The angular position and intensity of the peaks vary from cup to cup, depending upon the uniformity in manufacture, foil thickness, and degree of preferred orientation of the crystallites in the foil. All the CuK_α diffraction peaks of the foil are listed in Table 1.

In addition to the peaks listed in Table 1, there exists a very broad diffraction maximum similar in appearance to that produced by glass or other amorphous material. Its intensity reaches a maximum of 5 to 10 cps at 17 deg, and decreases to background level at approximately 10 deg- and 30 deg-2θ (Fig. 1). To determine the source of this maximum, a beryllium window was removed from a sample cup, mounted flat on a glass slide, and run in a standard Norelco diffractometer. The resulting pattern was identical to that produced by the lunar diffractometer, indicating that the source was the foil and not the beryllium frame or the sample carriage.

Superimposed on the diffraction maximum is an intense peak that appears at 16.5 deg-2θ, which is produced by the inner vertical beryllium walls of the cup. This peak does not occur when a sample is in the cup since the powdered material covers these surfaces. A sufficiently transparent specimen, however, may permit the transmission of sufficient X-rays to cause an increase in the counting rate at this angle. Therefore, it is suggested that all non-window surfaces of beryllium which are exposed to X-rays be covered with a heavy absorber, such as a foil of platinum, gold, or lead of an approximate 0.004- to 0.005-in. thickness. This technique should also reduce the background counting rate at all angles caused by scattering from these surfaces. Figure 2 presents a set of patterns which show the intensity variations of the 16.5-deg peak when the vertical beryllium walls are covered with an absorber.
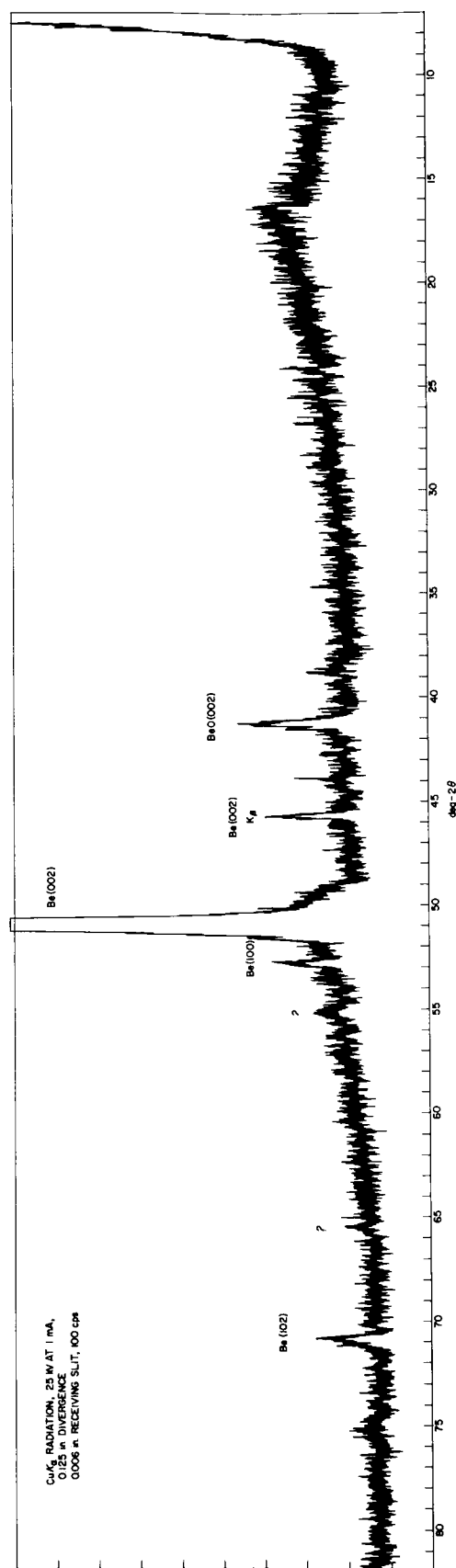
Fig. 1. Diffractogram of an empty, all-beryllium sample cup as produced by model P3D lunar diffractometer

Table 1. Diffraction peaks produced by beryllium foil with CuK_α radiation ($\lambda = 1.54$ Å)

Material	Reflection, hkl	Peak intensity I_p, cps	Interplanar spacing d, Å	Scattering angle 2θ, deg
BeO	(002)	22	2.19	41.2
Be	(002)	8	1.79	45.7 (K_β)
Be	(002)	2000	1.79	50.97
Be	(100)	5	1.73	52.9
?	?	10	1.66	55.2
?	?	10	1.42	65.5
Be	(102)	7	1.328	70.9
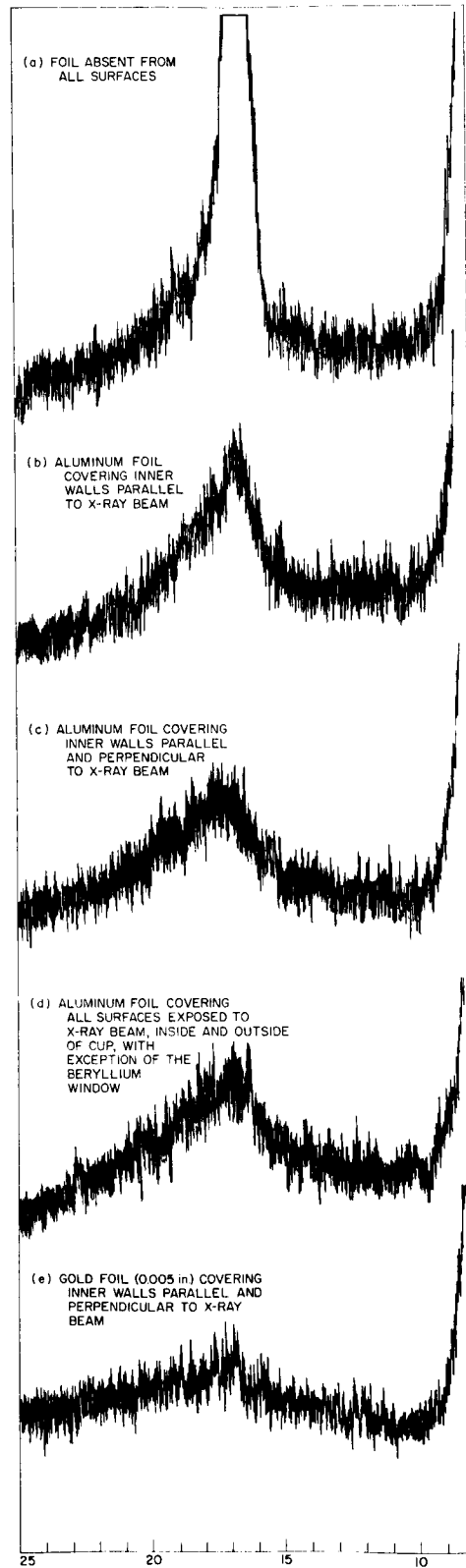
Fig. 2. Diffraction peaks pro-
duced for five conditions by
the inner vertical walls of
an empty, all-beryllium
sample cup

D. COMPARISON OF PERFORMANCE CHARACTERISTICS FOR BERYLLIUM (002) REFLECTION

N. Nickle

1. Testing Beryllium-Window Sample Cups

A test was made to show what differences exist in the Be(002) reflection parameters[1] between all available beryllium-window sample cups. The Be(002) reflection that exists as a strong peak ($\simeq 2,000$ cps) in all beryllium-window cups is intended to serve as an internal standard during modal analysis on the lunar surface. The centroid of this peak will act as a reference from which other peaks can be measured accurately.

Peak parameters of the Be(002) reflection are graphed in Fig. 1 for six all-beryllium and for five aluminum-frame sample cups. Each cup was scanned 10 times, reversed in the goniometer and scanned again.

The most pronounced difference existing between the two types of cups is in peak intensity; the aluminum cups average 19.6% greater intensity than the beryllium cups. The background intensity is essentially the same for both types. Resolution measurements are more consistent for the beryllium cups (deviation of 5.9% from the mean for $w/2$, and 5.5% for $w/10$) than for the aluminum cups (11.2% for $w/2$, and 11.0% for $w/10$). Symmetry measurements are also more consistent for the beryllium cups (deviation of 6.6% from the mean) than for the aluminum cups (9.1%).

The graph (Fig. 1) of degrees (deg-2θ) from reference mark vs type and number of cup refers to the angular separation of the centroid of the Be(002) peak to the nearest angle mark produced by the diffractometer. The centroid position for any one cup could be reproduced to ± 0.017 deg-2θ or less; this precision is considerably better than the design specification for centroid or peak reproducibility of 0.05 deg-2θ. The centroid position of different cups, however, varies considerably; the maximum difference among the cups tested was 0.19 deg-2θ.

2. Conclusions

The beryllium-window sample cups each display unique characteristics for the Be(002) reflection. The most significant variation is the 2θ angle at which the peak appears, since this is the reference from which all other peaks are measured. Therefore, each flight-model sample cup must be indexed and numbered and, also, its preflight peak-parameter characteristics recorded.

---

[1]Performance characteristics or peak parameters are defined in the Nomenclature at the end of the Report. See I_b, I_p, and $w/2$, $w/10$, and Sym.
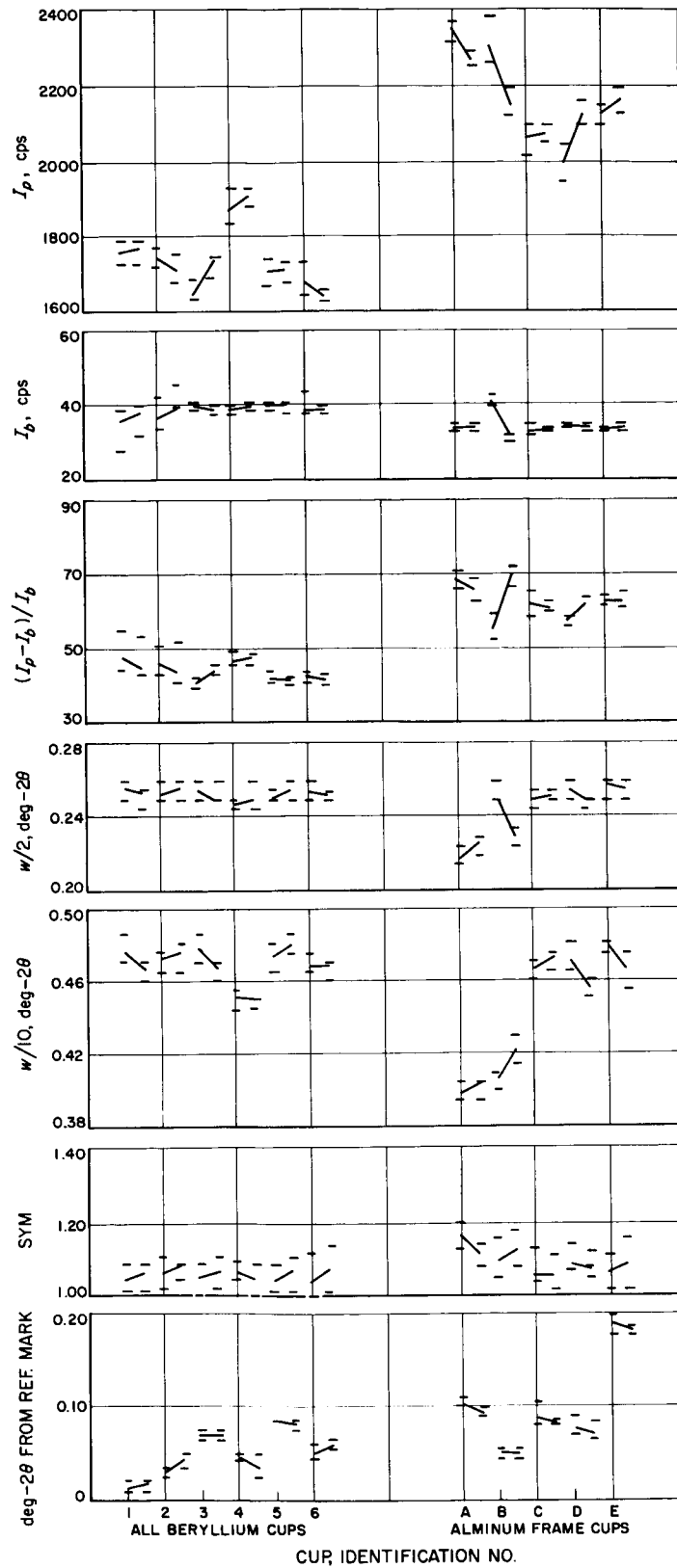
Fig. 1. Peak parameters of the
Be(002) reflections for all-
beryllium and aluminum-
frame sample cups

E. QUARTZ AND BERYLLIUM PEAK PARAMETERS VS TEMPERATURE OF BERYLLIUM FOIL

N. Nickle

An all-beryllium sample cup packed with quartz particles < 37μ was heated in the diffractometer by means of an heating element attached to the sample carriage. The results of these tests, as illustrated in Fig. 1, may be due in part to a slight heating of the preamplifier. The preamplifier, situated above the sample carriage, is subject to a portion of the heat supplied to the sample cup.

Changes in the peak parameters for the quartz(100), quartz(101), quartz(312), and Be(002) reflections were consistent, although the magnitude of the changes varied. Table 1 lists the changes in the peak parameters for a ΔT of 100°C.

Diffraction is caused by scattering of X-ray photons by the outer-shell electrons of the atoms in the crystal lattice. Intensity of a given reflection is dependent upon a structure factor of the crystal that, in turn, depends on the position of the atoms, the number and distribution of the electrons in the atom, and on the scattering angle θ. Heating the crystal increases the thermal motion of the atoms and, thereby, reduces coherence between diffracted waveforms--which may account for the 22 to 45% loss in the peak intensity.

Resolution increased slightly with the 100°C temperature change, ranging from 2.7 to 9.8%. The 2.7% increase represents the smallest measurable change in the resolution.

Peak symmetry showed a significant and systematic change when the cup and sample were heated from 25 to 125°C. For each peak measured, the symmetry became skewed toward lower 2θ angles. If the change in symmetry can be related to changes in the configuration of the sample surface through heating, then the magnitude of the change may be attributed to the length or area of the surface irradiated (i.e., $\ell = 2aR/\sin\theta$, where a = half-angle of divergent slit in radians, and R = radius of goniometer). At low angles, a greater surface is irradiated, and a greater symmetry shift is noted (Table 1). Additional peaks throughout the 2θ range of the lunar diffractometer must be measured, however, before a definite trend is established.

The most significant change is the shift in the centroid of the peak. The majority of the displacement can be attributed to the expansion of the hardware holding the sample (i.e., the sample carriage and sample cup). Calculations of Fig. 2 show how the displacement of the sample surface will shift the angular position of the
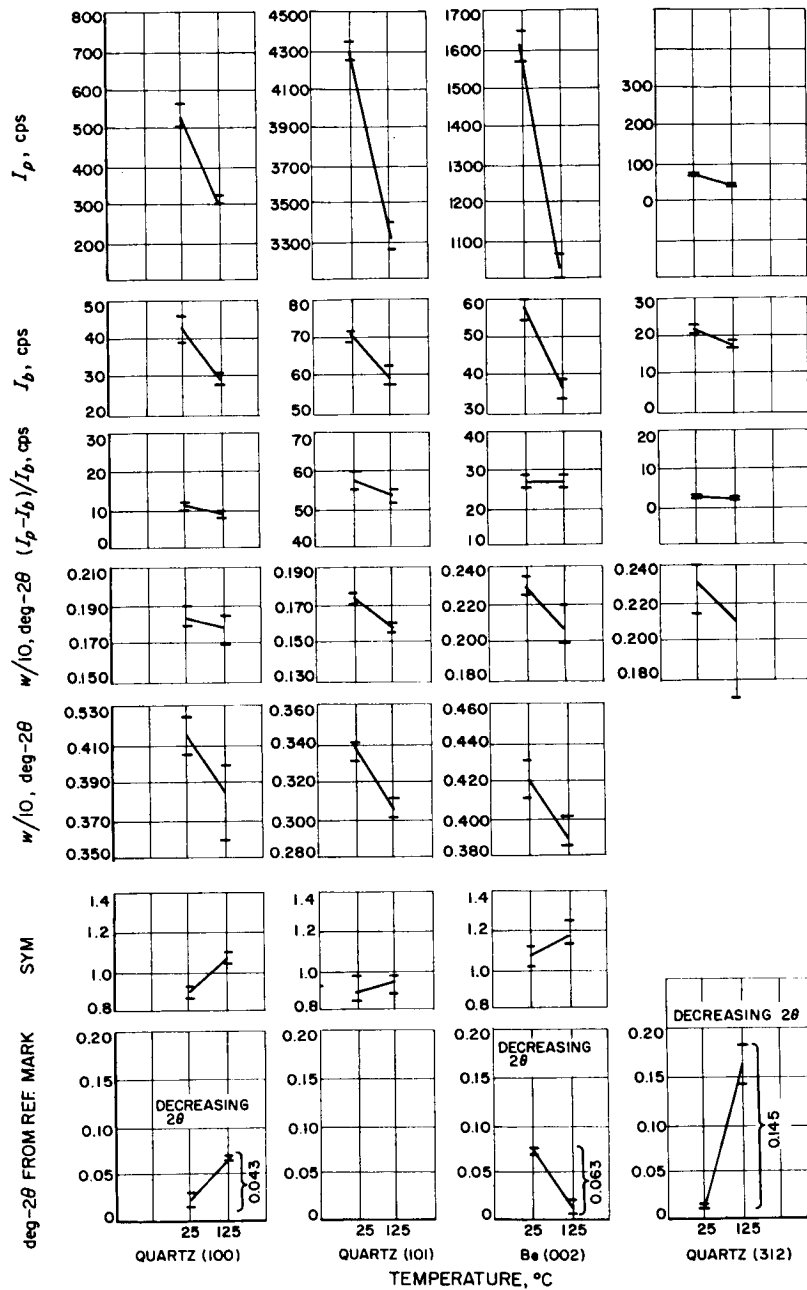
Fig. 1. Results of heating on an all-beryllium
sample cup packed with <37-μ quartz
particles from 25 to 125°C

Table 1. Changes in the peak parameters as a result of heating
the beryllium foil and sample from 25 to 125° C

Parameter	Quartz(100)	Quartz(101)	Be(002)	Quartz(312)
Peak intensity I_p, %	-43.5	-22.5	-36.0	-45.0
Background intensity I_b, %	-31.4	-15.8	-36.3	-17.9
$(I_p - I_b)/I_b$, %	-17.5	- 6.4	0	-48.2
Resolution w/2, %	+ 2.7	+ 8.7	+ 9.6	+ 8.6
Resolution w/10, %	+ 7.2	+ 9.8	+ 7.4	--
Symmetry	0.99	0.05	0.10	--
Peak shift, deg-2θ	- 0.043	--	- 0.063	- 0.145
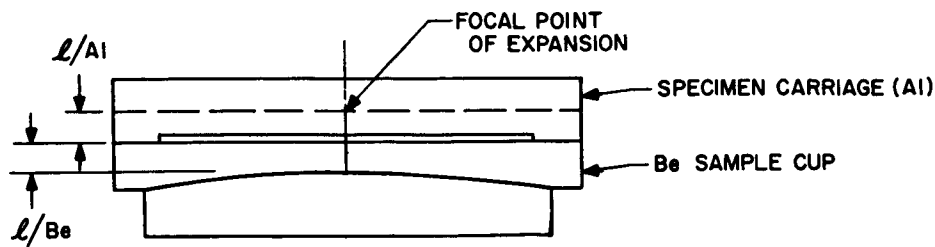
Material	Original dimension ℓ, in.	Coefficient of thermal expansion	$\Delta\ell$ from 100°C temperature change (25 to 125°C), in.	Total displacement $\Delta\ell$
Aluminum	0.096	25×10^{-6}	2.4×10^{-4}	3.66×10^{-4} in.
Beryllium	0.090	14×10^{-6}	1.26×10^{-4}	9.30×10^{-4} cm

The top of the beryllium foil, or the critical surface of the sample, will be displaced a total 9.30×10^{-4} cm when ΔT is 100°C.

Lower scanning limit
$$\Delta 2\theta = \frac{2s \cos\theta}{R}$$
$$= \frac{2(9.3 \times 10^{-4}\ \text{cm}) \cos 3.5\ \text{deg}}{8.5\ \text{cm}}$$
$$= 0.00022\ \text{rad}$$
$$= 0.0125\ \text{deg-}2\theta$$

Upper scanning limit
$$\Delta 2\theta = \frac{2s \cos\theta}{R}$$
$$= \frac{2(9.3 \times 10^{-4}\ \text{cm}) \cos 45\ \text{deg}}{8.5\ \text{cm}}$$
$$= 0.00015\ \text{rad}$$
$$= 0.0089\ \text{deg-}2\theta$$

If the diffractometer were heated from 25 to 125°C, the sample cup and carriage would expand so that a peak located at 7 deg-2θ would be displaced +0.0125 deg-2θ, and a peak at 90 deg-2θ would be displaced +0.0089 deg-2θ.

d of Be(002) reflection = 1.79 Å 2θ = 50.9743 deg at 25°C

Δd = +2.506 $\times 10^{-3}$ Å for ΔT = 100°C 2θ = 50.8985 deg at 125°C

$\therefore \Delta 2\theta$ = -0.0758 deg-2θ for Be(002) reflection when the foil is heated 100°C

The net a priori displacement of the centroid of the Be peak is:

$\Delta 2\theta$ for specimen carriage and sample cup at 50 deg-2θ = +0.008 deg

$\Delta 2\theta$ for expansion of unit cell = -0.076 deg

Net 2θ = -0.068 deg-2θ

Fig. 2. Centroid-peak displacement calculated from sample-surface displacement

peak at various scattering angles. No explanation is offered for the large shift in the quartz(312) reflection since a displacement at this high angle (91 deg-2θ) should be at a minimum, and those at low angles at a maximum (a cosine function). However, agreement is noticed in the total displacement of the Be(002) reflection in Figs. 1 and 2, approximately 0.06 deg-2θ to a lower scattering angle.
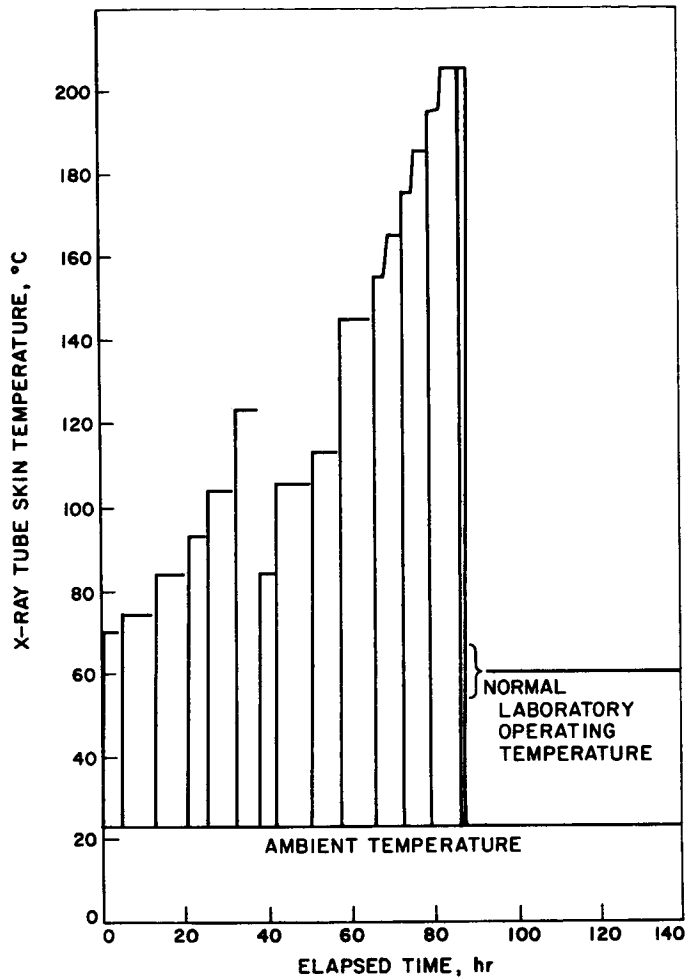
Fig. 1. History of induced heating of
one tube during operation on P3D
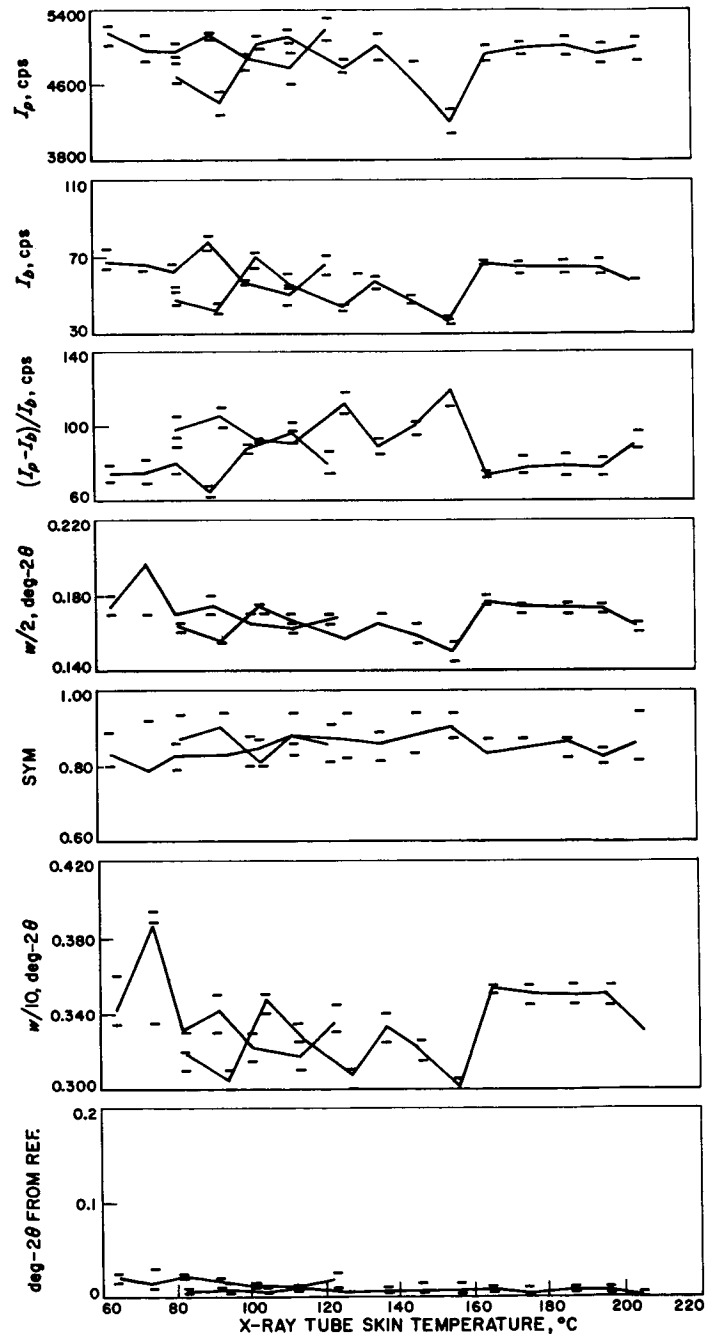
Fig. 2. Results of temperature tests
on the Mark 1 X-ray tube

F. OPERATION OF THE MARK 1 X-RAY TUBE AT ELEVATED TEMPERATURES

N. Nickle

A new miniaturized X-ray tube (No. PW 1103/10, P4261) was allowed to overheat during operation (25 kV, 1 mA) in order to determine the maximum operating-temperature limit when the tube is integrated with the lunar X-ray diffractometer. Changes in the peak parameters of the quartz(101) reflection were used as an indication of tube failure; the parameters were measured at 10° temperature intervals, ranging from 60 to 205°C, after thermal equilibrium had been established at each interval.

The tube survived 90 hr of operation at temperatures greater than those experienced during normal laboratory operation, and 7 hr at temperatures exceeding 200°C (Fig. 1). The variations of peak intensity, peak/background ratio, resolution, and symmetry of quartz(101) during these tests were within the error of measurement (Fig. 2). The two curves on each graph of Fig. 2 represent the data collected from two different detectors--one detector was inadvertently destroyed during the tests. The wide spread of the peak intensities was caused by problems in the test equipment and does not reflect faulty operation of the X-ray tube.

The tests were discontinued before X-ray tube failure to prevent destruction of other parts of the diffractometer. The proportional detector reached a maximum of 46°C, which is too warm for efficient performance, and the wiring insulation of the head electronics in the vicinity of the X-ray tube showed signs of overheating.

Since the tube did not fail at these elevated temperatures, there is an indication that the specific loading currently used is somewhat less than the maximum allowable value. Under present operating conditions, the specific loading is calculated to be 7.8 w/mm^2 for a focal spot size of 8 x 0.4 mm. A measure of the tolerable increase in specific loading would be the difference in the temperature of the focal spot and the melting point of pure copper.
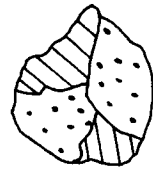
The focal spot temperature may be estimated by drilling one or more holes into the base of the tube, normal to, and within several thousandths of an inch of, the anode surface into which a thermocouple may be placed. Or, the beryllium window may be removed and the tube placed in a vacuum chamber, allowing the focal spot to be viewed with an optical pyrometer. These methods could then permit the

calculation of the increase in specific loading by either increasing the power to the X-ray tube or decreasing the focal spot size.

The upper operating-temperature limit for the Mark 1 X-ray tube is not known. If the tube were subjected to sufficient temperatures for failure, it is believed that other parts of the diffractometer would fail first. It is significant that no change in the peak parameters was noted when part of the goniometer casting was heated. This fact indicates little or no warping of the goniometer.

III. MARK 1 SAMPLING SYSTEM

Table 1. Various kinds of particles and particle aggregates encountered in pulverized rock samples

	Material	Homogeneity	Example
Particles	Monophase or monocrystalline particles	Each particle composed of a single mineral grain	
	Polycrystalline particles	Composed of two or more crystal grains (may be monophase or polyphase)	MONOPHASE POLYCRYSTALLINE / POLYPHASE POLYCRYSTALLINE
	Polyphase particles	Composed of two or more mineral grains of different composition	
Aggregates	Monophase aggregate	All particles composed of a single mineral phase (may be monocrystalline or polycrystalline, or both)	
	Polyphase aggregate	Particles of two or more mineral phases (may be monocrystalline, polycrystalline, or both)	

A. GUIDELINES FOR THE DEVELOPMENT OF A LUNAR SAMPLE PREPARATION SYSTEM

D. B. Nash

N65-34957

1. Introduction

The purposes of this paper are to discuss the problem of sample preparation for the X-ray diffractometer (XRD) and to summarize the guidelines for proper selection and handling of lunar-rock samples for X-ray analysis. Minimum sample requirements and sampler-design constraints are presented, as are model lunar surfaces for testing sampler mechanisms.

To achieve the experimental objectives of analyzing lunar composition, a selectively obtained and properly prepared sample must be delivered to the diffractometer. For a diffraction experiment on an unmanned spacecraft, dependence must necessarily be on a special device to acquire, prepare, transport, and emplace a sample into the goniometer.

Critical factors in the X-ray diffraction system are (1) the acquisition of lunar-rock samples that are representative of the mineral and chemical character of the rock unit from which they came and (2) the proper preparation of such petrological samples for analysis; both the precision and the significance of the data produced by the experiment rely on these fundamental operations. An analysis, no matter how thoroughly carried out, is no better than the quality and significance of the sample. The philosophy of those concerned with the diffraction experiment is based on these assumptions: Sample quality is more important than analytical quality, the proper selection of the sample is more important than its preparation, and a single good sample is the bulwark of a successful experiment. The fundamental criterion of a good lunar X-ray diffraction experiment is the clarity with which the resulting data concern the Moon, uniquely; capability to obtain random data is secondary.

2. Sample Source

Considering characteristics that we know of the Moon--such as its density, its terrain features, and its lack of atmosphere--it is expected that the kinds of materials to be encountered in sampling the Moon's surface, in general, will be similar chemically and mineralogically to known Earth and meteoritic rocks. They may consist of monophase or polyphase aggregates (see Table 1 for definitions) composed of silicate minerals, silicate glass, sulphides, oxides, and free iron and nickel.

These materials will be found in two distinct forms: lunar bedrock and lunar dust. Bedrock, part of the solid body of the Moon, was formed by processes originating within the Moon. Dust,[1] on the other hand, may consist of accumulated materials of diverse origin, including meteoritic debris.

It is expected that lunar bedrock will have mechanical properties not unlike those of terrestrial bedrock and meteorites. However, because of different surface environments and processes on the Moon, the dust layer may have mechanical properties quite different from those familiar on Earth.

X-ray analysis on lunar bedrock will indicate the nature of lunar rock-forming processes, which determination is the overall objective of this experiment. X-ray analysis of dust, however, will be exceedingly difficult to interpret in regard to processes by which the dust formed, because the dust will most likely be a disequilibrium assemblage of mineral and/or glass phases.

The depth to which a sample acquisition device must penetrate dust in order to reach lunar bedrock must be established in order to fix the design and operational mode of the device. In a sense, this depth must be a compromise one, based on consideration of the maximum probable average depth of lunar dust. From consideration of recent observational, experimental, and theoretical studies of possible lunar dust-forming processes (Refs. 1 through 3), it is proposed here to use a limiting depth of 25 cm, which provides a sufficient probability of obtaining a lunar bedrock sample and, at the same time, permits keeping the expected weight, complexity, and power consumption of the sampling device within tolerable limits. If the sampling device does not reach bedrock at this established depth, penetration will be stopped, a dust sample acquired, and analysis will be made only on the dust material.

3. Sample Requirements

a. Particle size. In order to yield an X-ray diffraction pattern with sharp maxima of greatest reproducibility whose relative intensities represent the concentration of phases in a polyphase aggregate, a sample must be composed of a large number of randomly oriented grains. This is best achieved by reducing the sample to fine powder. It is well known (Ref. 4) that for precise diffraction analysis the ideal particle size is from 1 to 10μ in maximum dimension. This does not mean,

---

[1] Arguments for the existence of a widespread lunar-dust layer are well known (Ref. 1) and will not be reviewed here.

however, that samples containing particles larger than 10μ are unacceptable. On the contrary, it has been found in our work on the lunar diffraction system that samples with maximum particle size of 1000μ can give useful results as long as they also contain a large number of fine particles. In any comminuted particle aggregate that has not been fractionated, there is a size-distribution that includes particles in the submicron range. Regardless of the maximum particle size, there will always be fine particles present that will occupy the interstices between the large particles and, therefore, some will lie smoothly along the inner surface of the beryllium window of the lunar sample cup, as shown in Fig. 1. Thus, even though many large particles are present, the specimen surface upon which X-rays are incident will be composed primarily of the finer size-fractions from which most of the diffraction will occur. In Fig. 2 is illustrated the relative character of diffraction patterns obtained with the lunar diffractometer from samples of both coarse and fine maximum particle size. Qualitatively, the patterns have similar peak intensities, except for several peaks which increase in intensity because of preferred orientation (see below) in the coarser size-fractions.

The presence of abundant coarse particles can result in loss of peak intensity due to extinction effects (Ref. 4, p. 129). For monophase samples, these effects are relatively insignificant; for polyphase samples, they may introduce errors in interpretation of relative peak intensities of two or more phases. Extinction effects are greatest when there is strong preferred orientation of particles. In general, however, extinction effects are small and can be ignored for most diffraction work.

Serious degradation of data can result, however, from the presence in the sample of too many extremely fine particles, which condition results from over-comminution or overgrinding of the sample. As the particles are reduced to below 0.1μ, diffraction lines are broadened. This effect is caused by: (1) reduction of the number of parallel diffracting planes within each particle below a minimum necessary for strong X-ray interference, (2) increased lattice disorder on the grain surface due to partial fusion and a higher volume proportion of surface lattice disorder, and (3) excessive coldworking, bending, or otherwise stressing of the tiny crystals. An example of severe loss of peak intensity caused by overcommunition is shown in Fig. 3.

b. Grain shape and preferred orientation. The shapes of monocrystal grains encountered in crushed-rock samples are equant, lath, or platy, depending upon the number and relative perfection of cleavage surfaces in the crystals. When crushed
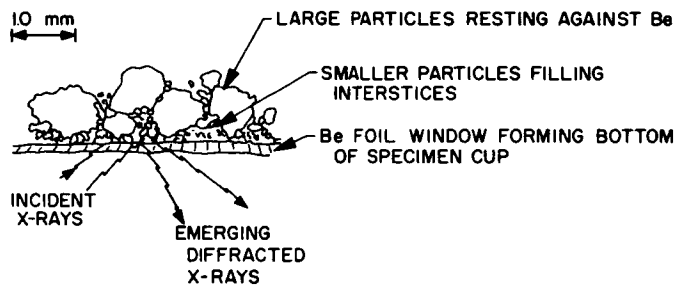
Fig. 1. Cross section through Be-
window sample cup containing
coarse powder of maximum
particle size

XRD PARAMETERS: CuK_α, 25 kV, ImA ; PROPORTIONAL DETECTOR, 2000 V ;
0.006-in. RECEIVING SLIT ; SCAN 1/2 deg 2θ/min

QUARTZ: PARTICLE SIZE < 37μ
(400 MESH)

QUARTZ: MAXIMUM PARTICLE
SIZE <1000μ
(16 MESH)

BASALT: PARTICLE SIZE < 37μ
(400 MESH)

BASALT: MAXIMUM PARTICLE SIZE <1000μ
(16 MESH)
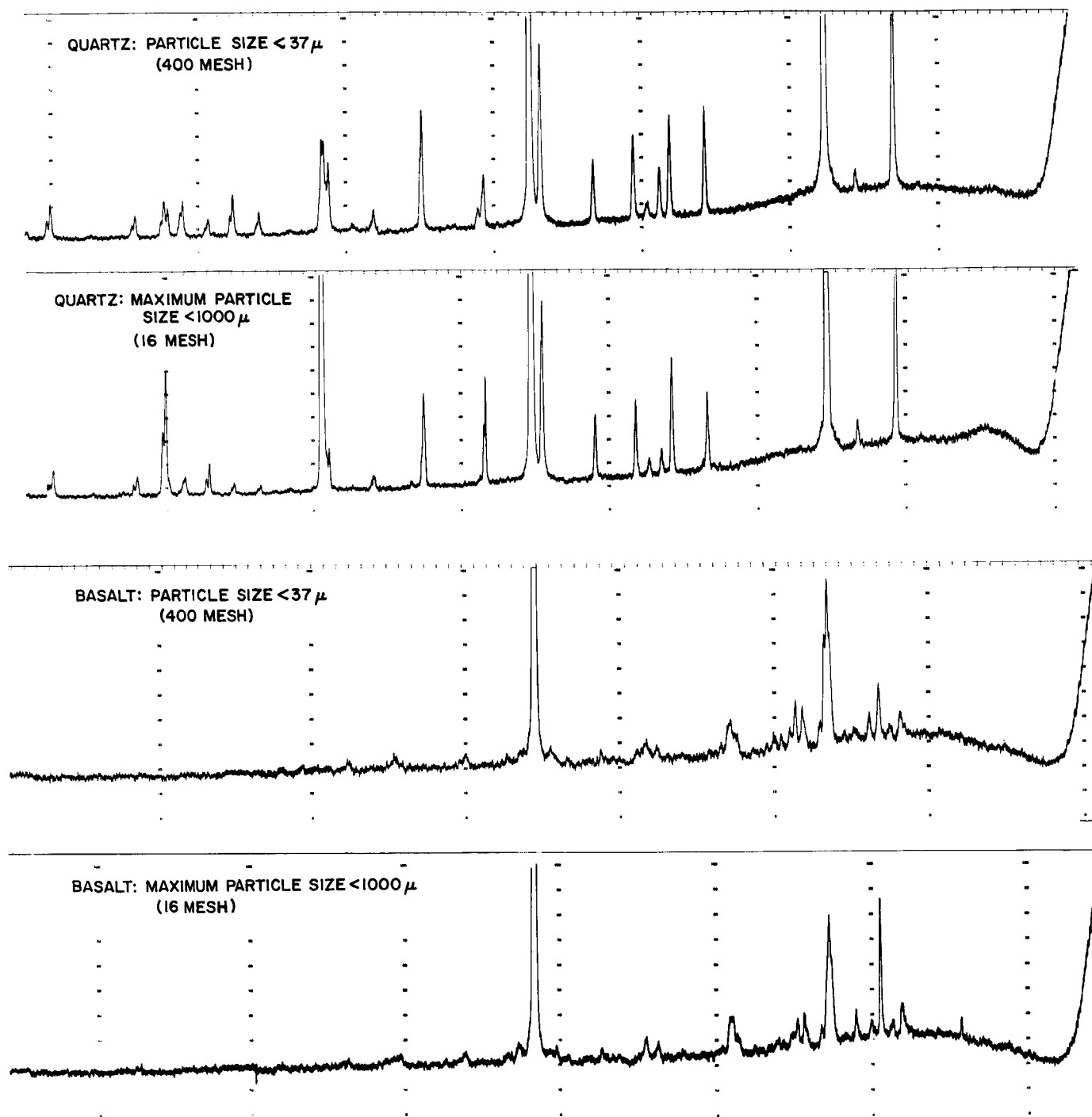
Fig. 2. Effects of maximum particle size on diffraction patterns of
pulverized-rock specimens
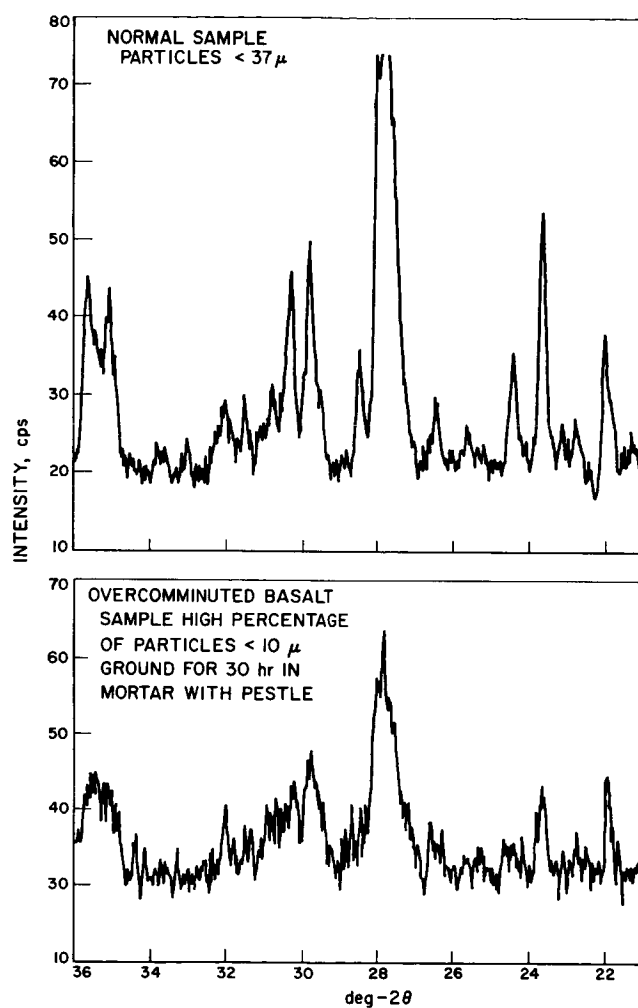
Fig. 3. Comparison of samples to show
the effects of overcomminution
of basalt

crystals with only one or two prominent cleavages tend to form two-dimensional particles that lie with their flat surfaces approximately parallel to the surface of the mounted sample. This condition can result in stronger peak intensities than those caused when the particles are in random orientation, because reflections from lattice planes parallel to the flat cleavage surfaces of the crystals will be abnormally strong, while those from planes not parallel to cleavage will be weak. Reduction of particle size aids greatly in reducing these preferred orientation effects; in general, particles 1 to 10μ in maximum dimension will have nearly a statistically random orientation. However, in spite of great size reduction, crystals with extreme cleavage (such as mica and tremolite) will still orient preferentially, and this fact must be taken into account when these materials are being analyzed or when their presence is indicated in a polyphase rock sample.

c. Porosity. Aggregates of particles of sizes suitable for reliable diffraction analysis do not naturally compact under gravity to the greatest possible bulk density; there are various inhibiting surface effects such as electrostatic charge, Van der Waals bonds, and absorbed gas molecules (if pulverization occurred in an atmosphere). High particle density is desirable for diffraction samples, first, in order to obtain the highest possible density of diffracting planes and the consequent maximum peak intensity, and second, to reduce the required thickness of sample (see below) necessary for minimum diffraction-peak width and asymmetry. The relationship of these factors is illustrated in Fig. 4, which shows that aggregates with low porosity yield diffraction peaks of higher intensity for a given sample thickness than do aggregates of higher porosity; therefore, some degree of compaction of the sample is desired to reduce sample porosity. The amount of compaction and, in particular, the method by which it is achieved must be properly chosen. Excessive or improper compaction, though resulting in favorable increased particle density, can result in unfavorable preferred orientation of lath or platy particles and in excessive bending of flexible crystals in such substances as mica.

Although little work has been done on measuring suitable porosities for X-ray samples, a working value of 50% porosity has been used as a guideline in our lunar X-ray work. This number was determined for a hand-pressed sample of quartz of $< 37\mu$ particle size mounted in the beryllium-window sample cup; the compaction reduced bulk volume by 75%. Quartz powder can be compressed this amount without preferred orientation of grains, but other materials such as micas could not be compressed without extreme preferred orientation.
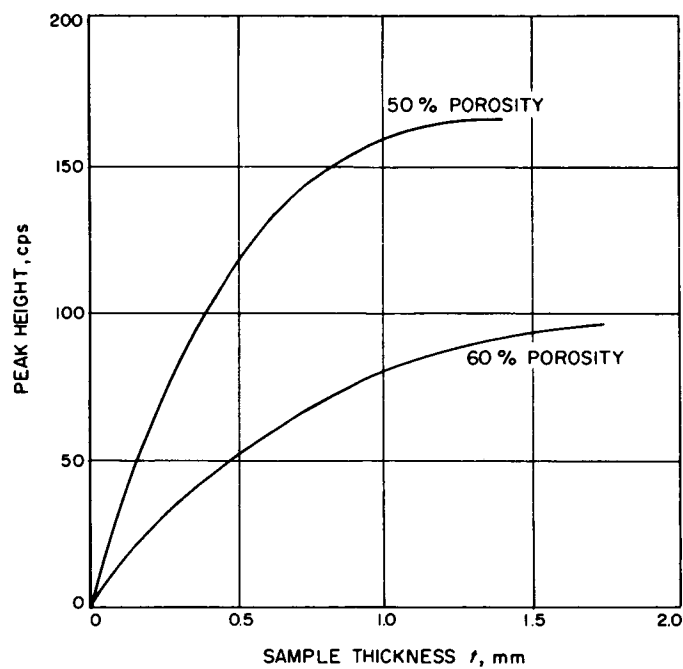
Fig. 4. Schematic relationship between
sample porosity, thickness, and peak
intensity, based on data for quartz
at 30 deg-2θ

For compaction, the best results can be obtained by simple compression of the sample powder. A shear type of motion would tend to "smear" the particles and to orient non-equant particles parallel to one another and to the sample surface. Vibratory compaction is considered undesirable, because it relies on gravity and tends to fractionate particles by size, shape, and density (see paragraph g. below).

d. Homogeneity. Only the particles in the thin layer closest to the irradiated surface of the sample contribute to diffraction. This is because the absorption coefficients of rock-forming minerals are large enough that all incident radiation is absorbed or diffracted within a few-hundred microns in the sample (see discussion on sample thickness below). Therefore, for a meaningful analysis, the thin surface layer that intercepts the X-rays must contain the same relative mineral abundances as does the bulk sample. Furthermore, the surface layer itself must have lateral homogeneity because (for a Bragg-Brentano geometry at constant divergence) the area of the sample irradiated varies with θ, thus causing the brightness of the irradiated specimen area to change constantly. Consequently, unless the layer is homogeneous, the relative diffraction-peak intensities on a given pattern cannot be compared.

e. Sample thickness. Because incident X-rays can penetrate into the sample, diffraction will occur at various depths within the sample. The depth to which useful diffraction occurs, and thus the minimum sample thickness that is practical, depends on sample transparency and the angle θ. Sample transparency is a function of two independent parameters--sample porosity and the absorption coefficients of the sample particles. These functions can be related by the expression here modified from Klug and Alexander (Ref. 4):

$$t \geq \frac{3.2}{\mu} \frac{\sin\theta}{1 - p} \tag{1}$$

where t is sample thickness, μ the linear absorption coefficient of the particles, and p the porosity of the sample. If t does not satisfy Eq. (1), then diffraction-peak intensity will be degraded, because some of the beam will pass through the sample before being absorbed or diffracted.

For a given porosity, then, the minimum required sample thickness depends on the absorption coefficient and will be large for particles of low absorption and small for particles of high absorption; this relationship is shown in Fig. 5. A minimum thickness must be based on the expected (lowest) absorbing particles. Absorption coefficients for various common rock-forming minerals (for CuK_α X-rays) are
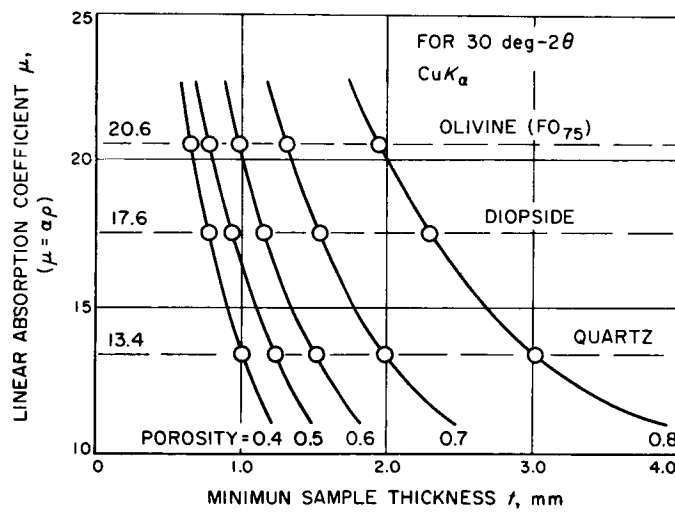
Fig. 5.   Relationships between minimum
optimum-sample thickness and
absorption coefficient of
sample particles for
aggregates of dif-
ferent porosities

listed in Table 2. For a quartz sample of porosity 0.5, the minimum thickness according to Eq. (1) for various θ angles is shown in Fig. 6; for maximum peak intensity at all angles 2θ up to 60 deg, the minimum sample thickness is 2.4 mm.

Table 2. Mass absorption coefficients of common rock-forming minerals and iron for CuK_α X-rays

Material	Mass absorption coefficient
Forsterite	32
Enstatite	33
Albite	33
Quartz	35
Sanidine	49
Anorthite	53
Diopside	58
Basalt Glass	72
Fayalite	191
Magnetite	237
Iron	324

In the lunar XRD sample cup (with 0.002-in. Be window) the depth of penetration of usable CuK_α X-rays at 30 deg-2θ in quartz is shown in Fig. 7, where it can be seen that less than 10% of the usable diffracted X-rays reach a depth of 1.0 mm.

Diffraction at deep levels, however, causes a shift in diffraction-peak position and an asymmetric peak broadening (toward the lower 2θ side). These effects are most pronounced for samples of low absorption and at lower 2θ. There may have to be some trade-off, then, between line intensity and line symmetry at low 2θ angles, and the optimum sample thickness chosen accordingly.

f. Contamination. Sample contamination consists of two types: cross-contamination between two or more consecutively processed samples, and bias-contamination resulting from addition of material to the sample from the sampler mechanism.
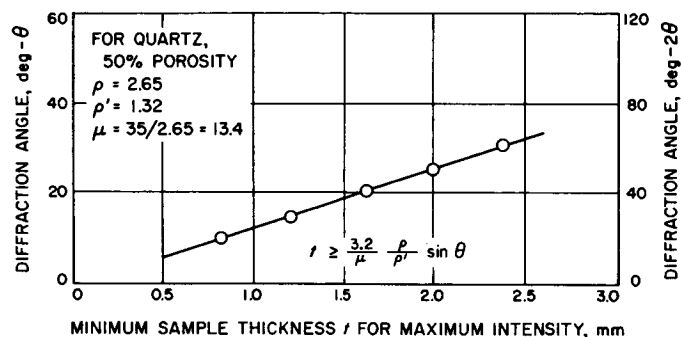
Fig. 6. Minimum thickness for quartz samples required to achieve maximum diffraction intensity at various 2θ angles
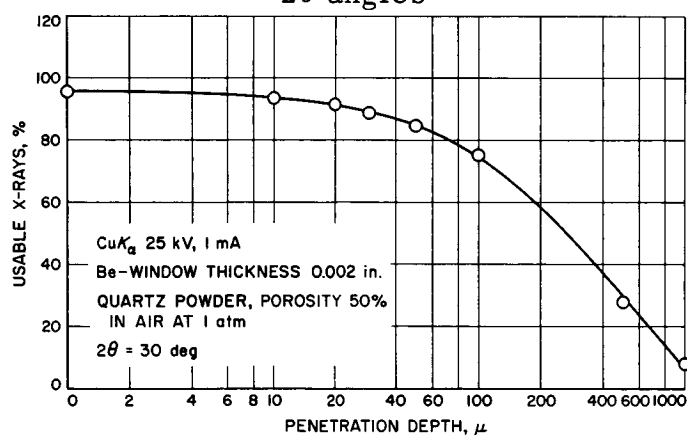
Fig. 7. Depth of penetration of CuK_α X-rays in lunar sample cup containing powdered-quartz sample with porosity of 50% for 30 deg-2θ

Cross-contamination results when the sampling mechanism is not adequately cleaned between preparation of successive samples. Thus, only the second or following samples will be affected, each containing a portion of all preceding samples. Cross-contamination can occur during sample selection; it is required that the lunar sampling device be capable of acquiring a bedrock sample from below a 25-cm overlayer of dust. Thus, contamination of the drilled bedrock sample by dust from the overlayer is possible and must be avoided by suitable mechanism design. Cross-contamination can result if the same beryllium-foil sample cup is used for consecutive samples, or if a continuous-flow sample over a single beryllium port is used without adequate means for cleaning the foil between samples; this is particularly important since the X-rays diffract from only that portion of the sample closest to the beryllium.

The results of cross-contamination are to introduce mineral phases into the sample that either are not present or are present in lesser amounts in the original rock. If the contaminant amounts to less than 1% by volume, its presence is unlikely to be detected by diffraction unless it is a very strong reflector, such as quartz. If the absorption coefficient of a contaminant phase is large or if constituent elements are easily fluoresced by the working radiation (CuK_α) the result may be a loss of intensity of diffraction peaks from the original phases (by dilution and absorption) and an increased background intensity (secondary fluorescence), even though the contaminant may produce no detectable diffraction peaks of its own. Metallic iron and iron-oxide could be such contaminants.

Bias-contamination results when material from the sampling mechanism becomes mixed with the sample being processed. Examples for the proposed lunar sampler would be chips from the drill bit and metallic grit from the abrasive action of sample particles during manipulation. The effect of this type of contamination is to dilute the sample with a high-density, highly absorbing, and usually strongly fluorescing material (i.e., iron, steel, cobalt, tungsten, etc.) with consequent loss of diffraction-peak intensity and marked increase in background level. Bias contamination by iron or other such materials is particularly undesirable for a lunar diffraction experiment because of the very strong possibility that at least one of the lunar samples, the surface dust-layer sample, may contain metallic iron derived from meteorites; in such a case, the diffractometer will not be able to distinguish between small amounts of meteoritic iron and carbon steel.

g. Fractionation. Fractionation of a sample is a change in relative phase abundance during sample preparation, which is due to selective removal of part or all of one or more phases of a polyphase aggregate (for definition see Table 1); the result is a sample that no longer has the same phase abundances as the original rock. Fractionation will most likely occur during two stages of sample preparation: acquisition and transport. The effects may or may not be cumulative.

During acquisition, the sampling device may selectively acquire only a limited size-range of particles from the previously drilled or pulverized material. Because some mineral grains are naturally smaller than others and because some, during drilling or crushing, will be reduced in size more than others (due to different hardness, cleavability, etc.), each size-fraction of the resulting aggregate may have phase abundances different from the others; consequently, selective sizing may leave behind a portion of, or even all of, one or more constituent phases. The mode of acquisition, therefore, should be such that all of the drilled or otherwise pulverized material, or a total volume unit of previously comminuted material (e. g., lunar dust), is acquired. If the volume unit acquired is too large for the subsequent preparation scheme or for the final sample, then it should be split into parts containing equal phase abundances.

During transport, motion of a polyphase particle aggregate relative to some confining structure, to a fluid medium, or to gravity, magnetic or electric fields can quickly fractionate its particles if they have different properties such as size, shape, density, magnetic susceptibility, and dielectric constant. Rock-forming minerals have a wide range of these properties, and polyphase particle aggregates can be severly fractionated prior to analysis by one or all of the above mechanisms (for an example, see results of fractionation test (Section III-F). Movement of polyphase particle aggregates, therefore, must be accomplished by means which minimize fractionation of any kind.

The effect of fractionation will vary, depending on the number and type of phases present in the original rock and, also, upon the kind of fractionation. For example, severe size fractionation of a monophase sample would not change the relative mineral abundance, but might yield excessively fine or coarse particles, either of which might result in degraded X-ray data. Density or shape fractionation of a polyphase sample would yield a sample that either is deficient in, or contains an excess of, one or more phases, to yield X-ray data that does not quantitatively represent the original rock.

h. Excessive temperature. During drilling or pulverization, friction between sample particles and the drill may cause the temperature of the particle to exceed the stability temperature of the mineral phase or phases making up the particle. Phase transitions are then possible that might permanently (i. e., for the duration of the analysis period) alter the sample character. Examples of temperature-induced phase transformations are the following:

1. Dehydration of hydrates and micas (100-500°C)
2. Structural transformation of low-temperature to high-temperature polymorphs, such as orthoclase $\longrightarrow$ sanidine ($\sim$750°C)
3. Decomposition of carbonates yielding CO_2 (800°C)
4. Solution of two or more exsolved phases such as perthitic microcline $\longrightarrow$ sanidine ($\sim$1000°C)
5. Fusion of silicates (1150-1710°C)
6. Reduction of iron oxides

Such modifications would yield X-ray data that erroneously suggest a high-temperature, rapid-cooling origin for the sampled rock.

4. Lunar-Sampler Requirements

The previous discussion attempted to point up the importance of careful control of the parameters for X-ray diffraction samples. Because of the necessary simplicity and reliability required of any unmanned system designed to provide the XRD with a sample, it would be ludicrous to expect the system to provide a perfect sample; thus, some compromise must be made in specifying the minimum requirements of the sampler device. Since the relative effects of variations in sample parameters differ widely, only those parameters most critical to the goals of the experiment will be specified; obvious exclusions are to be optimized.

a. Sample parameters. Minimum sample requirements are based on the present definition of objectives for the XRD experiment. These requirements, listed below, may be subject to change with future developments in the course of our research, in mission objectives, and with our increasing knowledge of the environment and materials on the lunar surface.

1. Grain size: Average maximum particle size to be less than 0.1 mm (Aggregate may contain some particles as large as 1.0 mm. Majority of particles should be between 1 and 20μ.)

2. Sample volume: Enough to cover the beryllium window to a minimum compacted depth of 1.5 mm (This amounts to an uncompacted volume of about 2 cm^3.)

3. Porosity: 60% or less

4. Contamination: Cross contamination less than 5 vol %; bias contamination less than 1 wt %

5. Fractionation: Minimum possible, preferably less than 15 vol %

6. Preferred orientation and excessive temperature-rise: Held to a minimum within design constraints

b. Acquisition requirements. The sampler system must be able to acquire and present to the XRD a satisfactory sample (as outlined above) from the following test models:

1. Basalt (solid) at surface

2. Pumice (solid) at surface

3. Basalt dust (< 37μ) at surface

4. Basalt sand (1/2 to 1 mm) at surface

5. Basalt under 25 cm of quartz dust (< 37μ)

6. Basalt under 25 cm of quartz sand (1/2 to 1 mm)

7. Basalt under 25 cm of quartz rubble (dust, sand, and pebbles from 5 to 10 mm)

8. Pumice under 25 cm of basalt dust

9. Pumice under 25 cm of basalt sand

10. Pumice under 25 cm of basalt rubble

Performance of the system will be evaluated by comparing the quality of diffraction (in terms of peak intensity, resolution, background intensity and contamination) achieved from the test samples with that of laboratory-prepared specimens of the same material.

c. Design constraints. The following list summarizes practical limits on system design:

1. A minimum of two lunar samples plus one Earth standard are to be provided. The lunar samples are to be (a) bedrock or a 25-cm-depth sample, and (b) dust at surface if it exists.

2. Pulverization, when required, must be simultaneous with sample acquisition (i.e., by the same mechanism) and be achieved solely by bit-to-particle and particle-to-particle crushing.

3. Particles should not be screened for particle-size separation.

4. Gravity should not be relied on to move the sample powder or facilitate transfer of powder from one subsystem to another.

5. Power requirements, weight, and complexity of the system should be as low as possible.

REFERENCES

1. Kopal, Z., Physics and Astronomy of the Moon, Academic Press, Inc., New York, 1962.

2. Orrok, G. T., Meteoritic Infall and Lunar Surface Roughness, Preliminary Report, Bellcomm, Inc., Washington, D. C., 1963.

3. Gibson, J. E., "Lunar Surface Characteristics Indicated by the March, 1960, Eclipse and Other Observations," Astrophysical Journal, Vol. 133, No. 3, May 1961, pp. 1072-1080.

4. Klug, H. P., and Alexander, L., X-Ray Diffraction Procedures for Polycrystalline and Amorphous Materials, John Wiley and Sons, Inc., New York, 1954.

B. DRILLING TEST PROGRAM

G. M. Hotz

1. Introduction

A rock-drill development program was carried on concurrently with an investigation into means of sample acquisition, transport, and transfer for a sampling system for a lunar X-ray diffractometer to be used on unmanned landers. Drilling was selected as the means of simultaneously fragmenting, processing (i.e., particle sizing), and acquiring the sample. Both rotary and rotary-impact drilling were investigated. Rotary drilling was found to be an adequate means of fragmenting hard rock but a marginal processing (particle sizing) method under the limitations imposed; on the other hand, rotary-impact drilling proved to be a much more dependable and efficient means of fragmenting and reproducibly processing hard rock. A mechanical rotary-impact breadboard drill of low power requirements and high efficiency was developed; this drill is shown in Fig. 1. Conclusions as to drilling parameters for lunar samples are discussed.

2. Drill Constraints and Design Goals

The principal design constraint of the drill-type sampler is the reaction force against a Surveyor spacecraft, which is limited to about 50 lb. Drill travel of 10 in. was specified, but the actual drill penetration required in dense rock was only of the order of 1/2 in.; this depth of penetration would produce enough powder (2 cm^3) for a diffraction sample, with a fair margin for losses. If solid rock were not encountered at the surface, a surface dust sample was also desired.

Weight of the sample acquisition unit would be about 10 lb. The drill should produce, process, and acquire a sample in rock types ranging in mechanical properties from solid basalt to a very porous pumice; further, there should be capability to acquire a sample in rubble, cohesive particulate material, and noncohesive, as well. Solid-bit drilling was established early as the preferred method of simultaneous acquisition and processing for bedrock materials; besalt was specified as a suitable test material.

Two methods of drilling, rotary and rotary-impact, were investigated. For rotary drilling, test variables were normal force, rotary speed, bit material and bit design; for rotary-impact drilling, variables were normal force, rotary speed, hammer energy, hammer frequency, and bit material. Penetration rate and power consumption were recorded.
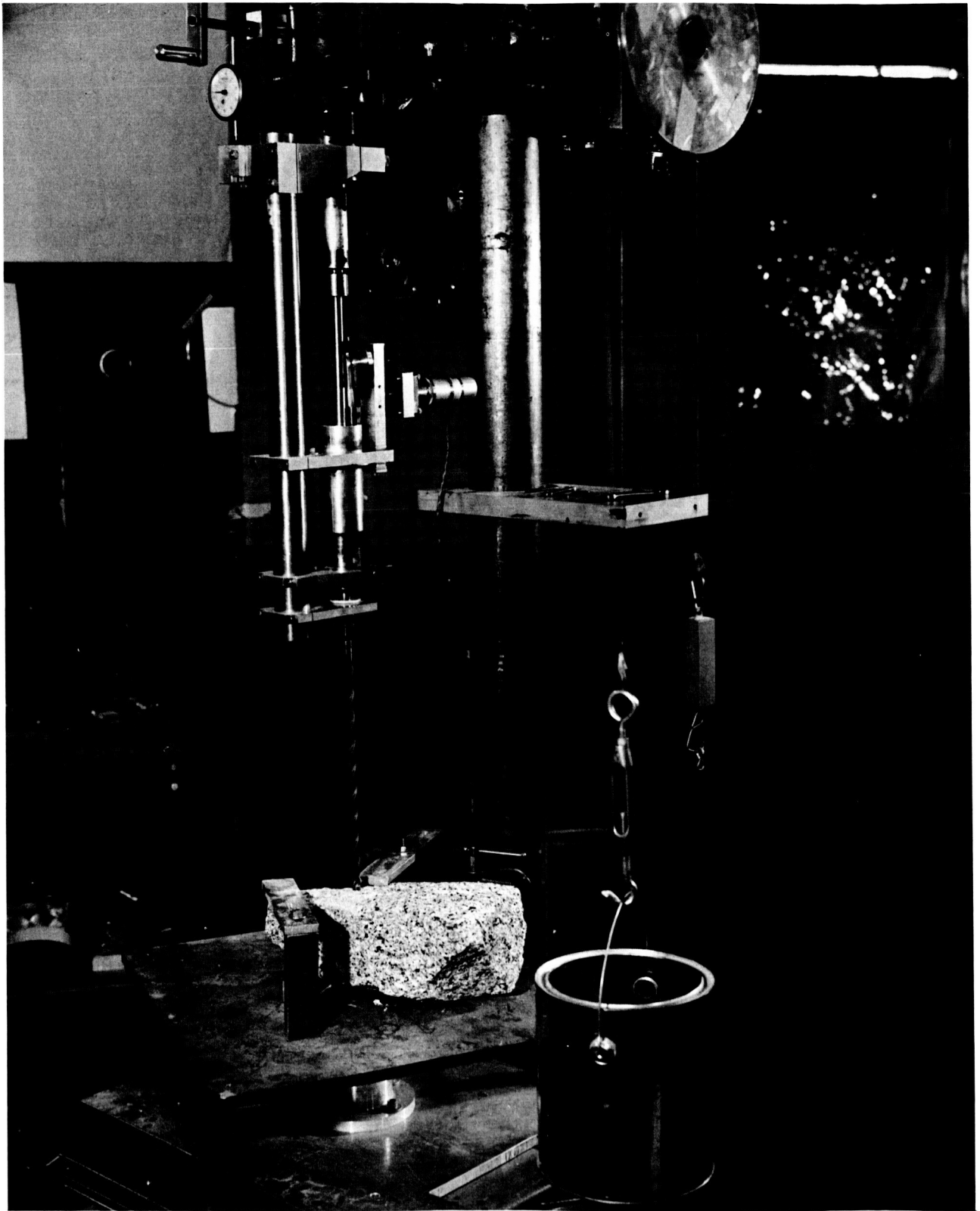
Fig. 1. Breadboard rotary-impact drill

The powders produced in the tests were analyzed without further processing on a standard laboratory X-ray diffractometer. The primary considerations in rating the effectiveness of the drill combinations were: the quality of the diffraction results compared with a laboratory standard of the same basalt, the rate of penetration, and the total energy per sample.

3. Drill Test Procedures

All drilling tests were performed with 1/2-in-diam bits. Most tests were run in basalt; tests in softer rocks (serpentine and pumice) indicated no problem in attaining high penetration rates nor in satisfactory processing of these materials as determined by X-ray diffractograms. Rotary drill tests were performed on a conventional drill press that was modified to allow bit speed to be varied over a wide range. The sample was mounted on a balance so that normal force was measured, and a torque meter permitted computation of input power. The rotary-impact tests were similarly conducted but included a mechanical device that also permitted impact frequency and energy, bit speed, and normal force to be varied over a wide range.

4. Rotary Test Results

Rotary test results verified, for the present design parameters, the conclusion which can be inferred from earlier lunar drill testing by Hughes Tool Company, Texaco Inc., and Armour Research Foundation, that is, penetration rate for rotary drilling at low normal forces is marginal. It was found, however, that other possible operating conditions could provide acceptable penetration rates.

There were other limitations to this kind of drilling; it was found that rotary drilling provides powder samples which give highly degraded diffraction data. The degradation is probably attributable to over-communition of the sample. Therefore, the operating limits for rotary drilling under the constraints of this program are bound by minimum penetration rate, by allowable normal force, and by penetration rate vs rpm field at which powder diffraction quality is acceptable. These relations are shown in Fig. 2.

5. Rotary-Impact Test Results

In the rotary-impact drill mode, sufficient stress to cause fragmentation can be produced by the addition of dynamic forces to a static normal force. In rotary drilling, on the other hand, the stress can be produced only through high normal force and small bit contact area (i. e., sharp drill).
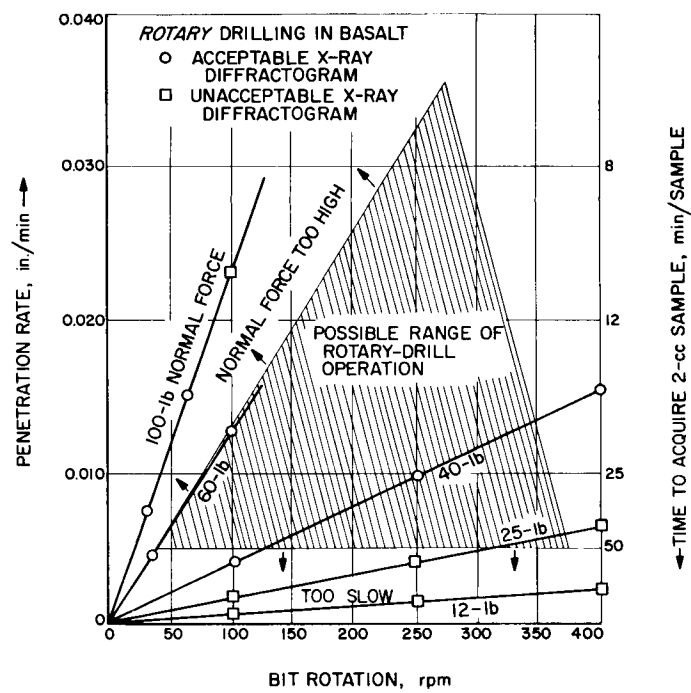
Fig. 2. Possible range of rotary-drill
operation in basalt

Rotary-impact drilling generally provided more reproducible test data, gave superior X-ray diffraction quality from the drill powders, and produced samples with less expenditure of energy than did straight rotary drilling. Some of the results and conclusions are as follows:

The X-ray diffraction quality from samples secured by rotary-impact drilling varies as follows:

1. Independent of impact frequency within the range tested (Fig. 3)

2. A function of impact energy, increasing with increasing energy (within the limited range of energies tested)

3. Not clearly related to normal force, but not degraded by increased normal force if the ratio of impact energy to rotational energy is high

4. Degraded by a high ratio of bit-rotation rpm to impact frequency; the higher this ratio, the more nearly the result approaches rotary drilling (If the ratio is small --say less than 1:3 but preferably less than 1:10--there appears to be no effect upon XRD quality.)

Penetration rate of rotary-impact drilling varies as follows:

1. A function of impact frequency, increasing with increasing frequency (Fig. 4)

2. A function of impact energy, increasing with increasing energy (Fig. 4)

3. A function of normal force, increasing with an increase in normal force (Fig. 5)

4. Beyond a minimum rpm, independent of bit rpm

Power consumption is as follows:

1. Proportional to impact frequency

2. Proportional to impact energy (Fig. 6)

3. Almost independent of normal force (Fig. 5)

4. Almost independent of bit rpm

QUALITY DEFINITIONS:

1. EXCELLENT   ALL PHASES (INCLUDING MINOR
              BIOTITE) CLEARLY DISTINGUISHABLE
2. GOOD   ALL PHASES RECOGNIZABLE,
              GOOD RESOLUTION, LESS
              INTENSITY, GOOD DETAIL
3. FAIR   RECOGNIZABLE AS BASALT
4. POOR   BARELY RECOGNIZABLE, SOME
              AMBIGUITY
5. BAD   PATTERN VERY AMBIGUOUS
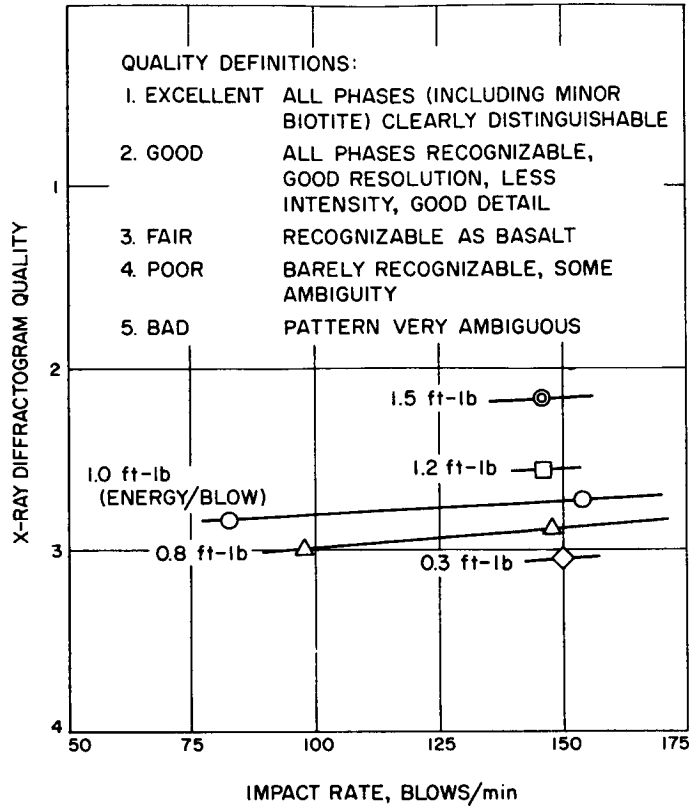
Fig. 3. Rotary-impact drilling in
basalt, diffractogram quality vs impact rate
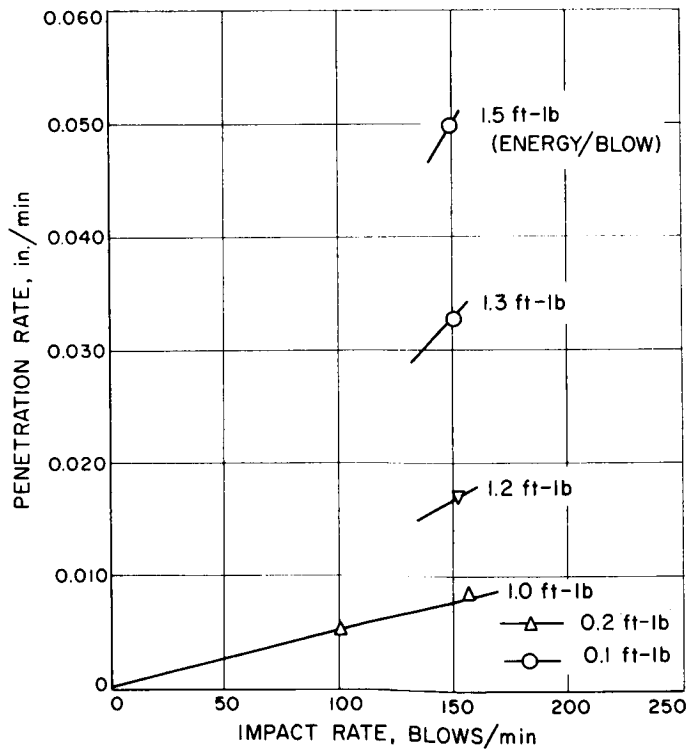
Fig. 4. Rotary impact drilling in
basalt, penetration rate vs impact rate
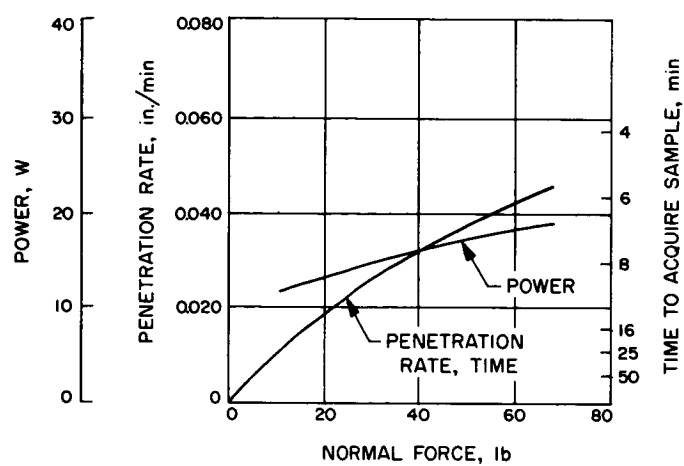
Fig. 5. Rotary-impact drilling in
basalt, power and penetration
rates vs normal force
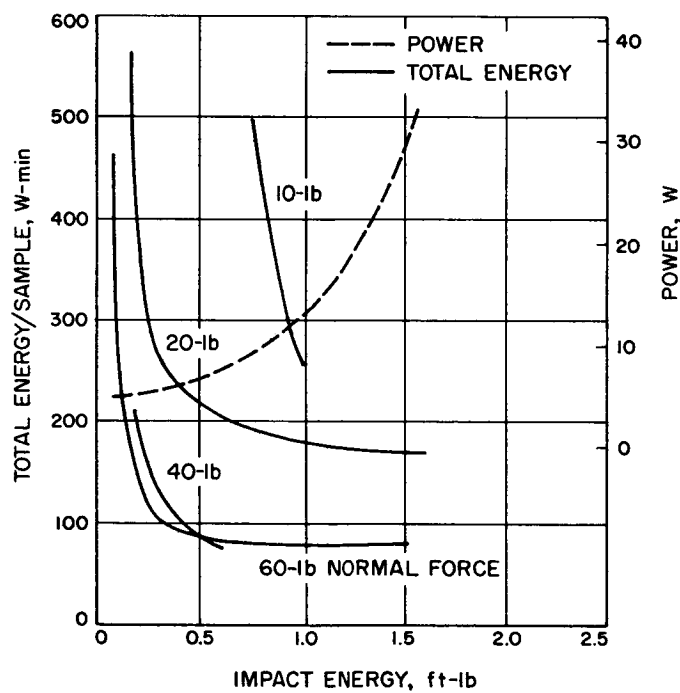
Fig. 6. Rotary-impact drilling in
basalt, power and total energy
vs impact energy

6. Conclusions

It appears, therefore, that a lunar X-ray diffractometer sampling drill should function as follows:

1. Employ the rotary-impact mode.
2. Operate at the highest normal force possible.
3. Operate at a low bit rpm relative to impact rate (e.g., rpm = impact rate/min x 10^{-1}).
4. Operate at a relatively high impact energy per blow (e.g., for a 1/2-in.-diam drill, a minimum of 1 to 1-1/2 ft-lb, depending upon bit weight).
5. Operate at an impact rate commensurate with desired power rate (with corresponding penetration rate).
6. Employ lightest feasible drill and impact anvil to achieve maximum peak force for the selected impact energy.

The results of this study indicate that a drill designed for the objectives given above should have the following characteristics:

1. Power rate: 40 W
2. Penetration rate (in basalt): 0.6 in./min (8 min/sample)
3. Normal force: 40 lb
4. Impact rate: 200 impacts/min
5. Impact energy/blow: 1 to 1-1/2 ft-lb
6. Bit rotational speed: 20 rpm
7. Bit diam: 1/2 in.
8. Cutter material: tungsten carbide

C. ACQUISITION AND TRANSPORT MECHANISM

F. Teeple

N65-34959

1. Introduction

A test program was conducted to evaluate several devices proposed as acquisition and transport components of an XRD sampler breadboard. The devices were tested for acquisition efficiency (volume of material picked up per centimeter of penetration), transport (lifting of sample from hole to XRD tray level), contamination between samples, and fractionation of the sample by the acquisition and transport operations. To a lesser extent, the devices were evaluated for mechanical performance and compatibility with other sampler components.

Two of the devices tested, the hollow bit with an internal valve and the sleeved screw were found to best meet the XRD-sampler functional requirements and exhibited satisfactory mechanical performance.

2. Sampler Function

The function of the sampler is to obtain 2 cc of bedrock if bedrock is within 25 cm of the surface and 2 cc of overlay material if it exists. Contamination between the two samples is to be less than 5%. Maximum bedrock particle size is to be 0.1 mm, assuming that the size frequency distribution follows natural comminution laws.

The test models (see Section III-A) were selected to represent a wide range of mechanical properties of rock materials and, also, to produce distinct X-ray diffraction patterns.

3. Sampler Devices

The devices tested (Figs. 1 and 2) are the screw or auger, screw with sleeve, hollow bit, hollow bit with valve, and belt conveyors. For sample acquisition, all devices feed downward into the material to be sampled; impact is added for penetration.

Transport is accomplished in the following ways: the simple screw and hollow bit retract from the hole up to XRD tray level. The conveyor belt raises material to the XRD tray level without bit retraction. The screw and sleeve may transport by retraction or by continuous flow of material up through helical passages in the screw.
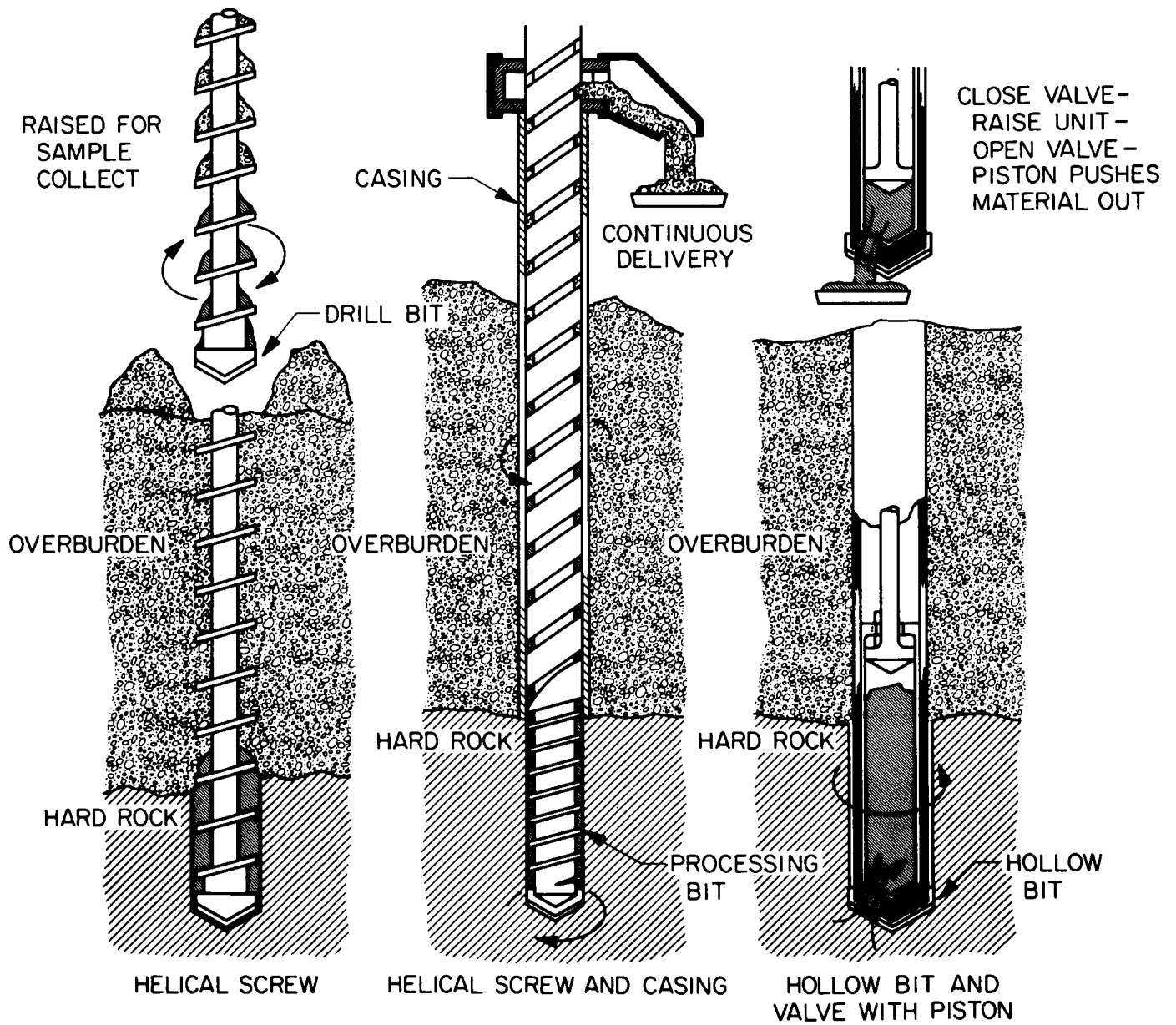
Fig. 1. Sample transport methods
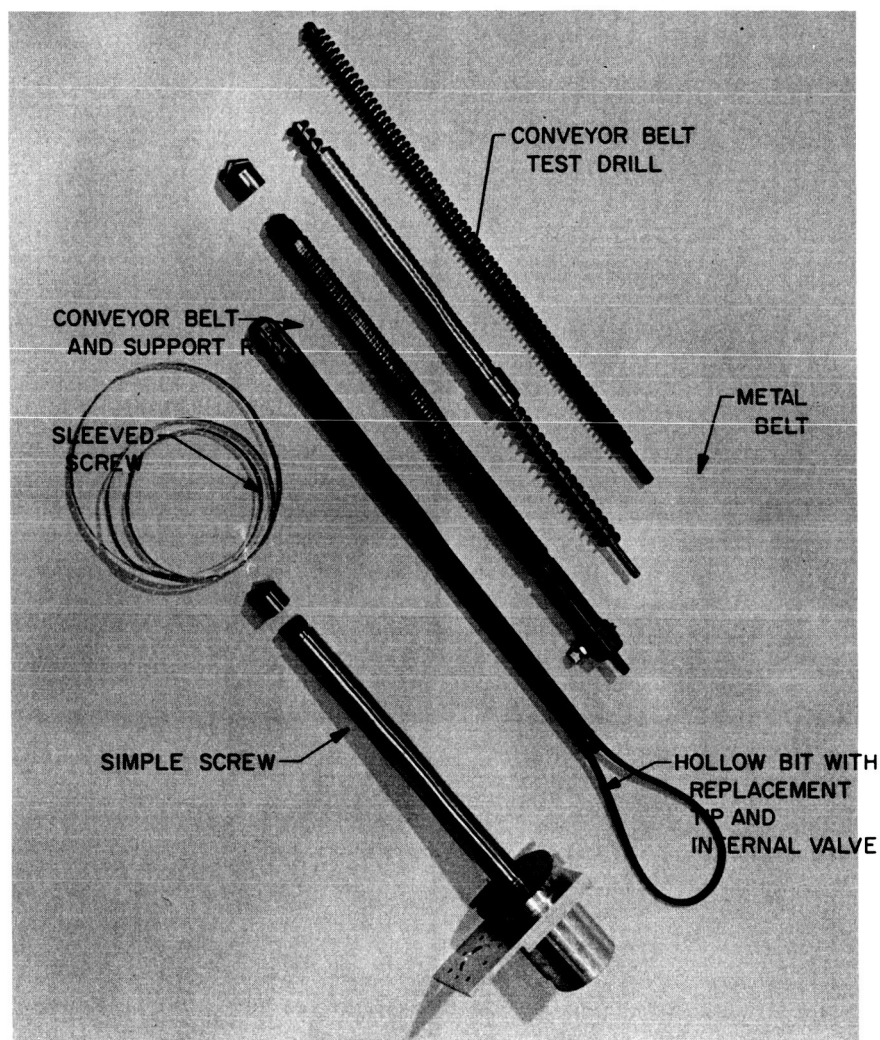
Fig. 2. Sampler devices

4.   Performance and Recommendations

a.   Screw.   Twelve screws with different thread shapes and leads were tested at various rotational speeds and feed rates.   Acquisition and transport were marginal in noncohesive models.   Contamination greatly exceeded 5% in several of the test models.   This device is not recommended for XRD sampling.

b.   Sleeved screw with independent sleeve feed and rotary drive.   This device (Fig. 3) acquires a relatively large sample per centimeter of penetration in over-burden by counterrotating the sleeve in order to feed overlay material down to the tip of the screw.   The sample is then conveyed up the screw rotating inside the sleeve. By proper choice of root diameter at the screw tip, coarse material is processed by grinding between screw and sleeve.   The power required for processing is less than 10 W.   The small root diameter of the screw and the counterrotation section prevent overlayer material from entering the screw when penetrating to bedrock through an overlayer.   The sleeve is seated in bedrock to seal off the overlayer, and the screw then continues drilling into the bedrock for the bedrock sample;   drilled material is conveyed up the screw threads into the sleeve.   Tests to determine contamination by overlayer material were limited, but indications were that contamination was less than 5%.   Transport of material up the column may be accomplished by rotating the sleeve at 200 rpm, and the screw at 275 rpm in the same direction; the centrifugal-force component then forces the material against the sleeve, and the material moves up the screw like a nut.   Attempts at low-frequency vibratory transport were not successful.   This device, the sleeved rotary-screw with counter-rotating sleeve, is recommended as a possible acquisition and transport mechanism for the XRD sampler.

c.   Hollow bit with piston.   The piston permits closing of bit openings when penetrating an overlayer, but does not permit closing of openings after acquisition. If bit holes are shaped for good acquisition (Fig. 4) in all the rock test-models, sand-like (noncohesive) material is lost on retraction.   This device is not recommended for sampler use.

d.   Hollow bit with valve and piston (Figs. 2 and 4).   The valve prevents loss of the sample during retraction and limits contamination during penetration of the overlayer.   The largest bit openings that bit strength would permit were used to ensure efficient acquisition.   To acquire a sample of overlayer material, a greater depth of penetration is required with this device than with the sleeved screw;   also, the maximum particle size admitted is about the same size as the bit openings.

Fig. 3. Sleeve-screw test rig
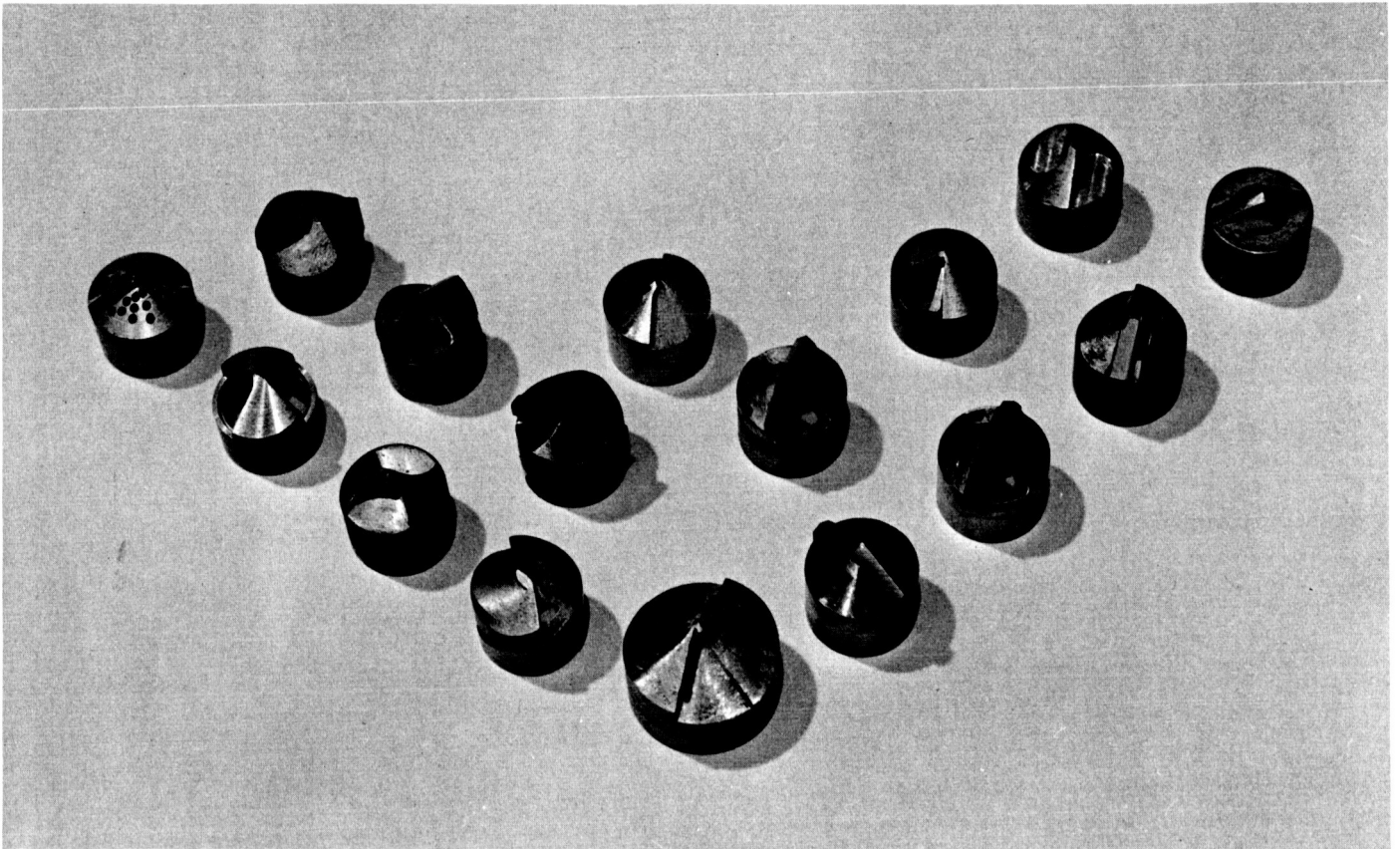
Fig. 4. Tips for the hollow bit

Some device would be required to remove these large particles from the XRD tray. Contamination, from information based on a limited number of tests, is less than 5% Material was removed from the bit by running the impactor and operating the piston. No difficulty was experienced with valve jamming. This device is recommended as a possible XRD sampler.

e. Conveyor belt. Two types of belt conveyors were tested: metal belts with integrally formed buckets, and reinforced elastomer belts with slits which open (to admit material) when rounding the bottom roller. Both types require control of the maximum particle size admitted to the belt (see Fig. 4 for tips tested to limit particle size to belt). Slight vibrations of the metal belt during transport tend to shake material out of the buckets. The elastomer belt tends to sort by particle size, favoring transporting of the larger particles. A relatively large drill-column diameter is required to contain the belt. Considering the limitations of, and the alternatives to, belt transport noted above, a belt conveyor is not recommended.

5. Conclusions

Two of the devices tested are recommended for further investigation and possible use--the hollow bit with valve, and the sleeved screw. The hollow bit with valve meets the functional requirements of the sampler in the test models specified. Acquisition is marginal in some of the models, although at least 2 cc of the sample material was acquired in all models, well within the 25-cm travel limitation of the device.

The sleeved screw also meets the functional requirements of the XRD. In addition, this device processes coarser materials by grinding, and it is possible to cycle the device to transport material by screw-conveying without retracting the unit from the hole. The screw bit can be made stronger than the hollow bit and is smaller in diameter; however, this device is more apt to jam than the hollow bit and is mechanically somewhat more complex.

The following devices tested either did not meet sampler functional requirements, or are not recommended for the reasons stated:

1. The simple screw allows excessive contamination; in addition, acquisition is marginal in some of the test models.

2. Hollow bits (without valves) that have holes sized and shaped for good acquisition permit leakage of the non-cohesive test models during retraction.

3. Conveyor belts require control of maximum particle
    size to the extent of making acquisition submarginal
    when used with hollow bits; also, for the elastomer
    belt the sample was sorted to the larger sizes, and
    for the metal belt transport efficiency was very sensi-
    tive to vibration. The advantage of continuous trans-
    port over retraction of a device for transport is out-
    weighed by these limitations, plus the added mechanical
    complexity of a conveyor belt.

D. A VIBRATORY SAMPLE EXTRACTOR

A. C. Dunk and U. A. Pineda

N65-34960

1. Introduction

This paper discusses the design and development work being conducted on an extractor subsystem which may be used in the Mark 1 sampling system.

Many mechanical operations must be performed by the sampling system prior to analysis of the sample by the diffractometer. The sampling system can be operated as either a batch process or a continuous process. Each approach will have its advantages and disadvantages. Ideally, in either approach, all material must be extracted from the drilled hole; a mechanism with this capability must be provided.

If the hole is cleared by the batch process, then it appears desirable to leave a casing in the hole to prevent overburden from entering the hole while the drill is being retracted. The mechanism required to operate the casing and the drill in this approach appears excessively complex, and additional length of mechanism must be used to accommodate the retraction of the drill stem. Therefore, the continuous removal of powdered rock from the hole is a more attractive approach.

In the continuous-removal approach, the powdered rock must enter the extractor at the bottom of the hole and leave the top of the extractor at a point above the lunar surface. This extraction method is the subject of this paper. Once the powdered rock is delivered to the top of the extractor, it is possible to use either continuous-sample transfer and presentation or batch transfer and presentation. Each of these presentation methods is discussed in Section III-E of this Report.

2. Extractor Design

Throughout the development program, two important constraints must be considered carefully. First, the sampling system should be completely automatic; second, it must operate in the lunar environment. To meet the requirement of automatic operation, the designer will be forced to use a fairly complex approach. However, to provide a design that can operate without failure in the lunar environment, complexity should be minimized. Relative motion either between the sampler components, themselves, or between the lunar soil and any sampler component should be studiously avoided. Simple motions and mechanisms should be used in preference to more complex mechanisms, even though the complex mechanism appears to provide a more desirable functional performance.

To follow the design philosophy of optimizing simplicity, it was decided early in this program to combine into one mechanism the capabilities of rock cutting (chipping, drilling), pulverization, powder acquisition (collection), and transportation of powder to the top of the hole. It was assumed (and later verified by Hotz and Teeple of this Laboratory) that sufficient particle-size reduction (pulverization) could be accomplished at the rock-cutting site by the same tool bit; no separate pulverizer was to be provided. Some sacrifice in sample quality may result from this dual operation, particularly for the lunar dust sample; however, considerable complexity is avoided. The design and function of this device, called an extractor, are considered below.

a. Rock cutting. On the basis of test data, which are shown qualitatively in Fig. 1, it was decided to use the impact mode for the rock cutting, or chipping. The rock is chipped by a sharp chisel-pointed bit. No bit rotation is required for this function; however, rotation of the bit between impacts is provided to bring the cutting edge of the bit into contact with a new region of the rock.

According to Hotz (see Section III-B), X-ray analyses of samples produced by an impactor indicate less sample degradation than do the analyses of samples produced by rotary drilling. Fig. 1 also indicates that, to achieve a given penetration rate at low applied loads, the required static load is much lower for the impact mode than for the rotary mode. Hence, the impactor cutting mechanism is best suited for meeting the performance requirements and design constraints of the XRD sampler.

Several commercial impactor designs exist (in the range above 250 W of power). The simplest approach uses a synchronous solenoid. One of these units,[2] was purchased and modified for mounting purposes. The impactor consists of an especially designed bit which is held against the rock surface by a static load (nominally 50 lb for Surveyor) and a hammer, which is reciprocated by the solenoid at a specific frequency. Ideally, the hammer should strike the impactor bit when the hammer has attained its maximum velocity, so that a maximum amount of energy can be transferred to the bit on each stroke. Neither the hammer nor the bit (which oscillates axially) has exact sinusoidal motion when the static load is applied, but these motions are more nearly sinusoidal when the bit load is removed.

b. Powder transport. For the present, we will assume that the problems of sample acquisition in an environment of high vacuum and very little gravity can be solved by bit entrance design, and will proceed to the problem of elevating or transporting the sample to the top of the hole. Many approaches and schemes -- such

---

[2] Syntron electric hammer drill Model No. 10 A-RO
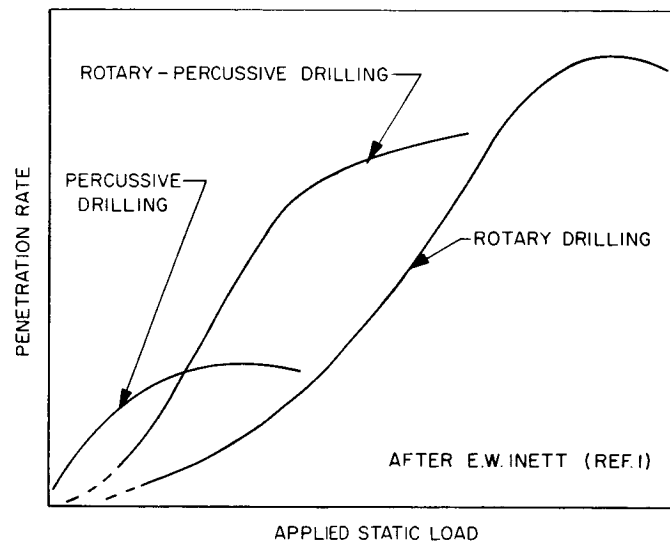
Fig. 1. Curves of penetration rate
vs applied static load for various
modes of rock drilling

as counterrotating screws, conveyor belts, and sample cavities or cells which must be opened and closed--have been considered and tested (see Section III-C); but a simpler and, possibly, more reliable approach is that of a vibrating helical conveyor. Functionally, this approach is attractive because a small force is applied directly to each particle by the conveyor. No compression is required such as would occur in a piston and cylinder pump. Conveyors of this general type are commercially available. However, none are small enough or have been designed to operate in the lunar environment.

The mode of operation can be described by considering that the helical conveyor has a sinusoidal helical motion such that each point on the conveyor traces a helix in space. To simplify the discussion, we shall replace the helical conveyor by the inclined-plane conveyor of Fig. 2. Because of the type of drive, points A and B on the conveyor will move sinusoidally in the vertical direction (Fig. 3) and sinusoidally in the horizontal direction.

Let us assume that particle P, located at A (and accelerated vertically upward by contact with the tray), has reached the same vertical velocity as the tray and is slowing down at a rate equal to the gravity acceleration g; at the same time, the tray is decelerating vertically at a rate greater than g. The particle will continue vertically until its upward velocity reaches zero at C; then it will fall, due to gravity, until it contacts the tray at B (shown in Fig. 3). If the particle does not bounce, it will have zero relative velocity perpendicular to the tray. However, it will have a component relative to the tray surface until the friction force reduces this to zero at D. The particle again leaves the tray (point B) at point E of Fig. 3.

In the lunar application (low gravitational acceleration), it is necessary to modify this motion by providing an upper surface in the tray to force the particles to rebound to the tray floor. Let us assume that the particle strikes the tray upper surface at G (Fig. 4) and rebounds to meet the tray bottom surface at B. The particle verticle-displacement time then will be as shown in Fig. 4. The successful operation of this type of conveyor can thus be achieved for any value of gravitational acceleration.

3. Sample Extractor Test Rig

A sample extractor test rig with a minimum number of moving parts (Fig. 5) was designed and built to demonstrate the feasibility and effectiveness of powdered-rock acquisition and vertical transportation from a hole by vibration. Cross-sectional views of the extractor and vibrator drive are shown in Figs. 6, 7, and 8. Although these sketches show the extractor with a drill-bit cutter, no cutting and processing of
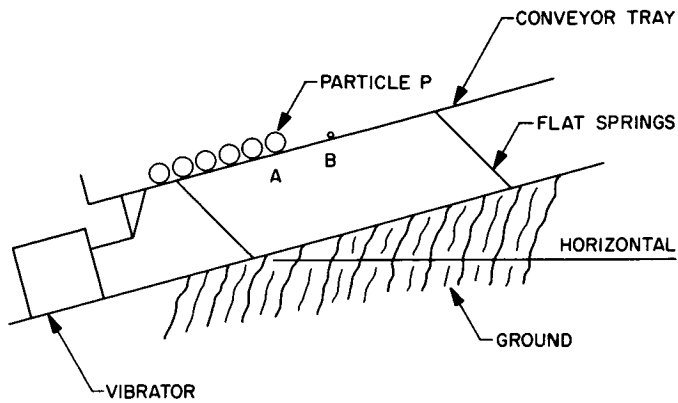
Fig. 2. Schematic of a vibratory
inclined-plane conveyor
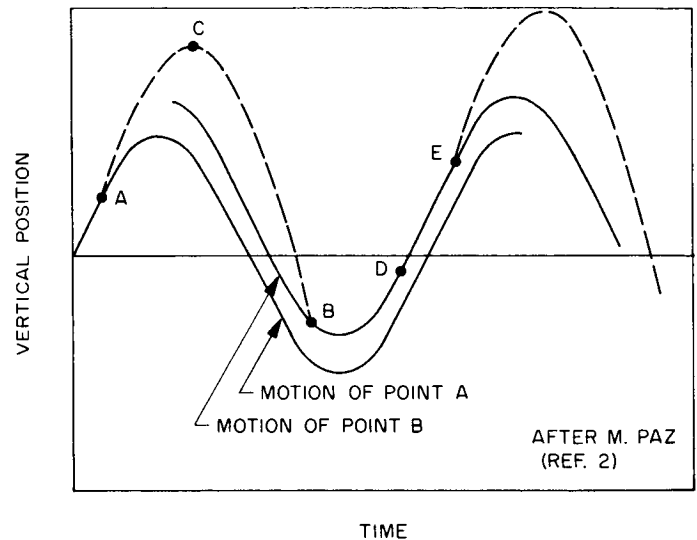
Fig. 3. Displacement-time diagram
of the vertical motion of an
unconfined particle on a
vibrating, inclined
plane
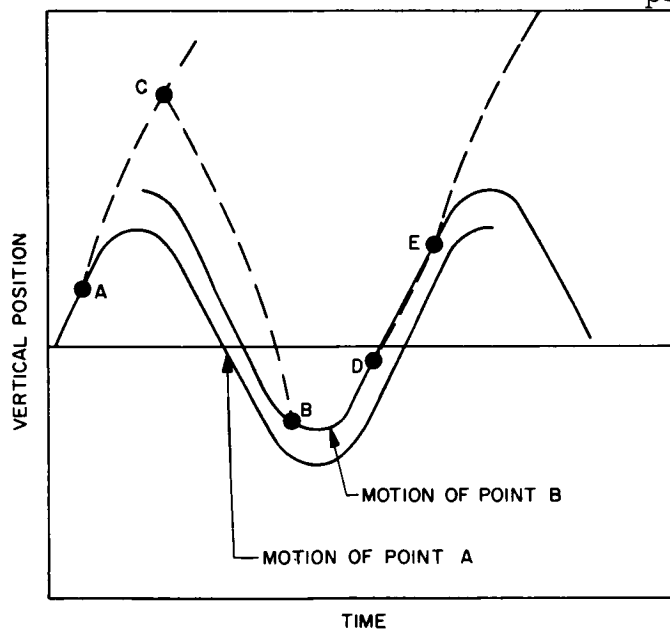
Fig. 4. Displacement-time diagram
of the vertical motion of a confined
particle in a vibrating tray
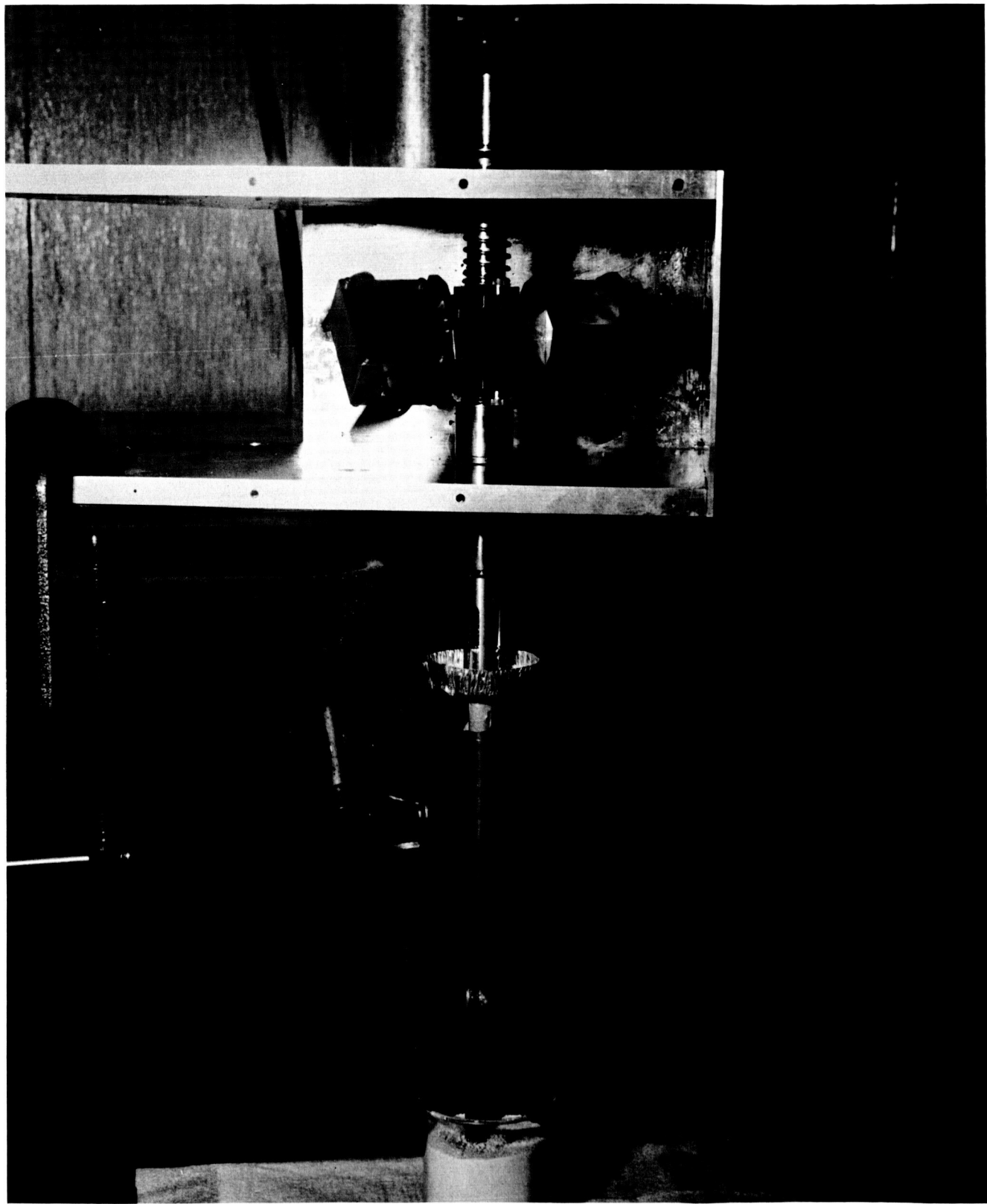
Fig. 5. Vibratory-extractor test rig
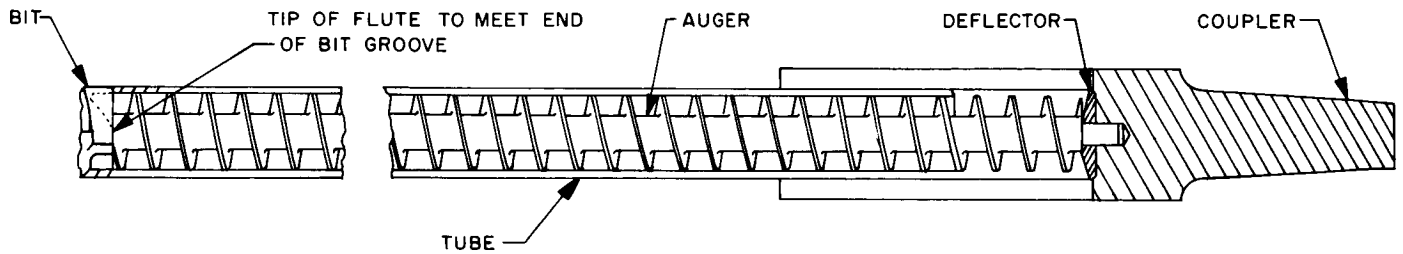
Fig. 6.   Cross section of extractor bit
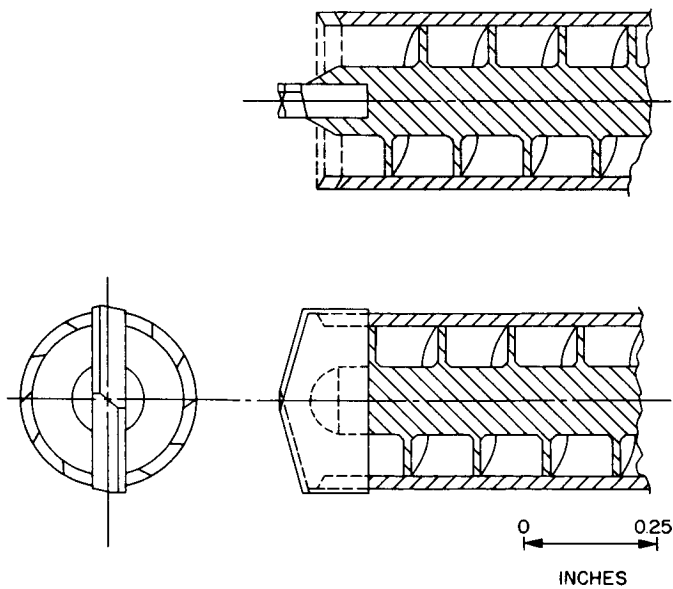
Fig. 7.   Cross section of acqui-
sition end of modified
extractor bit
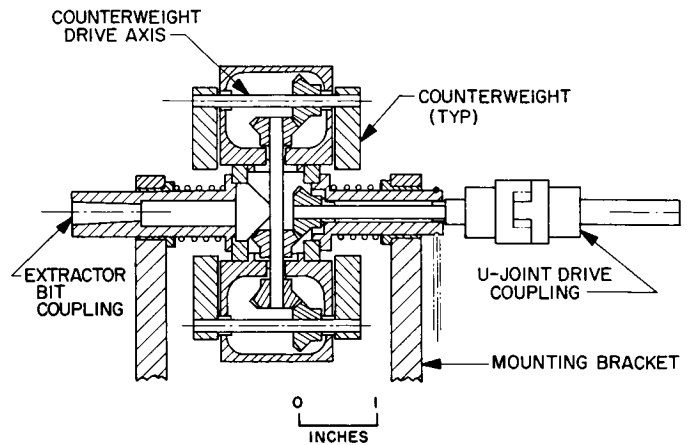
Fig. 8.   Cross section of test
extractor-vibrator

the specimen was attempted with the assembly, since this particular drive unit was designed to provide only the ideal sinusoidal motions required for sample acquisition and vertical transportation.

Essentially, the rig mechanism consisted of a screw integral with a sleeve, vibrating as a unit to become effectively a covered helical conveyor. The vibratory motion of the screw-sleeve assembly has linear and rotary components, causing every point on the extractor to trace a helical path. The effective up-slope travel per vibration cycle of a particle on the helical "inclined plane" is a function of the following factors:

1. Vibration frequency
2. Particle size, shape, and density
3. Helix angle and pitch of screw
4. Relative amplitudes of linear and torsional modes
5. Coefficient of friction between particle and helix surface

Vibration of the extractor causes the powder particles to move onto the flutes above the bit cutter. The vibration of the conveyor then causes each particle to move upward during the upward counterclockwise phase of the cycle; during the downward clockwise phase, the particle decelerates in a downward trajectory, landing on a point uphill from the original point of departure on the helical conveyor. Each vibration cycle causes each particle to travel upward on the helical conveyor.

Tests have been conducted with this rig to study, evaluate, and establish certain parameters that will be used in the design of an efficient and reliable Surveyor instrument. To simulate lunar-sample acquisition, these tests were made using samples of basalt rubble, quartz sand, pulverized rutile, and mixtures of these in particle sizes ranging from 1 mm to $< 37\mu$.

The main parameters studied in these tests were:

1. Drive speed. Input rotational speed (rpm) equals vibration frequency (cycles per minute).
2. Direction of drive forces. Among other things, the effective travel of a particle on the helical conveyor is a function of the relative amplitudes of the linear and rotary modes. The ratio of these amplitudes can be varied by changing the angle between the axes of rotation of the counterweights and the extractor axis. When the axes of rotation of the counterweights are perpendicular to the extractor axis, only linear vibration parallel to the

extractor axis occurs. If the rotation axes of the weights are set
at an angle other than 0 or 90 deg to the extractor axis, a rota-
tional couple results and produces a rotary mode in phase with the
linear mode. At the other extreme, when the counterweight axes
are parallel to the extractor axis, only rotary vibration occurs.

3. Specimen particle size and density.

4. Sample delivery. Depth of extractor bit in particulate material
   when delivery commences; sampling rate in cubic centimeters per
   minute.

5. Fractionation. Separation, if any, of particles of different
   densities and/or sizes from a mixture during acquisition and
   transport.

6. Angle of inclination of extractor axis to the local vertical.

Figure 9 shows curves of sampling rates vs drive speed (vibration frequency)
for various particle sizes and for drive angles of 45 and 60 deg. The observations
recorded from these tests may be summarized as follows:

1. The vibratory principle of particle transport appears feasible.

2. Coarse particles (e. g. , 20/30-mesh sand or basalt rubble) are
   transported at the greatest rate at a drive speed near 1900 rpm
   (approximately 32 cps frequency).

3. Fine particles ($< 100\mu$) are delivered at the greatest rate at drive
   speeds in excess of 2700 rpm (> 45 cps frequency).

4. High-density materials are transported at lower rates as com-
   pared with transportation of low-density material of equivalent
   sizes.

5. The mechanism functions most effectively when the vibration
   frequency is approximately 35 cps and the drive angle is about
   60 deg.

6. Fractionation in mixtures of coarse and fine, low- and high-
   density particles appears (by visual comparison) to occur at
   frequencies less than 2200 cpm; however, no visible separation
   was observed in the frequency range of 2200 to 2700 cpm.

7. Agglomeration of fine particles ($100\ \mu$ or finer) has been observed,
   but a large percentage of these appear to be readily dispersible in
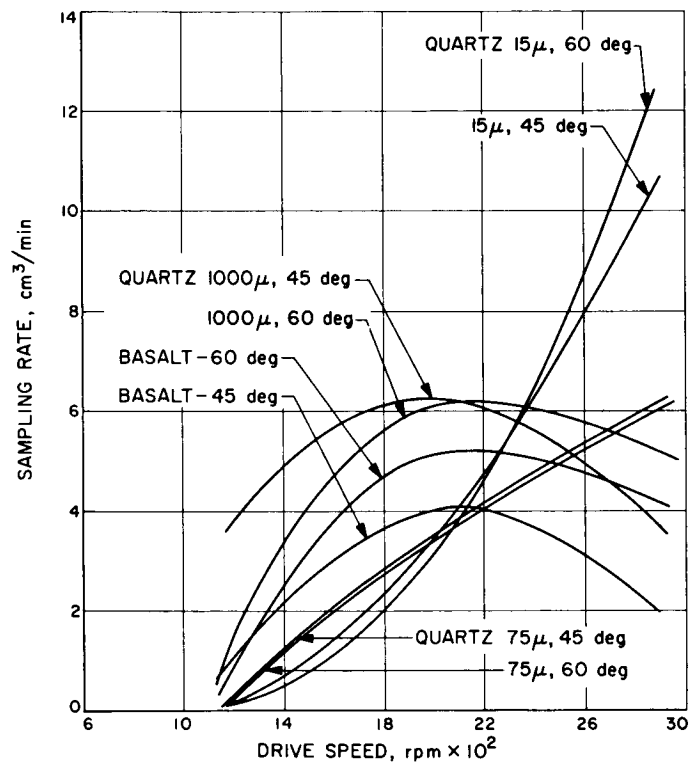
Fig. 9. Curves of sample-delivery
rate vs drive frequency of test
extractor

the receiving cup. It cannot be ascertained at this time whether the agglomeration occurs prior to acquisition, during transport, or at delivery.

8.   No change in delivery rates was observed when the extractor was run at a 15 degree inclination to the local vertical to simulate spacecraft tilt.

4.   Sample Extractor Subsystem

The vibratory motions required for rock cutting (impactor) and for vertical transporting (helical conveyor) are not simultaneously achievable with a single mechanism; therefore, to produce the greatest overall efficiency, it appears necessary to perform the cutting operation and the vertical conveying operation sequentially.

An extractor subsystem mechanism study was initiated to investigate the problems of combining the motions that are required for acquisition and vertical transport with the motions that are required for cutting into bedrock and then processing (pulverizing) the bedrock powder so as to satisfy requirements of XRD sample specifications.

This investigation will use the principle of the vibrating helical conveyor, which has been demonstrated as an effective mechanism for sample acquisition and vertical transport. The conveyor mode will be combined with the rotary-impact type of motions found effective for hard-rock drilling and pulverizing (see Hotz, Section III-B). Combination of the motions required to accomplish the objectives of the lunar sample extractor subsystem will obviously eliminate the need for separate drive mechanisms, will achieve the objectives with a minimum number of parts and, hence, will minimize trouble spots and increase reliability of the system.

The extractor subsystem mechanism to be used in studying this motion-combination problem has been designed, built, and is now undergoing tests. Figure 10 shows the assembled test rig. The major subcomponents of the mechanism are:

1.   A modified Syntron electric hammer drill, Model No. 10 A-RO. Electrically, the hammer is still a self-contained unit, meaning that it has a built-in control (selenium rectifier). The modification consisted of separating mechanically the hammer body from the handle and trigger-switch assembly which also houses the rectifier.
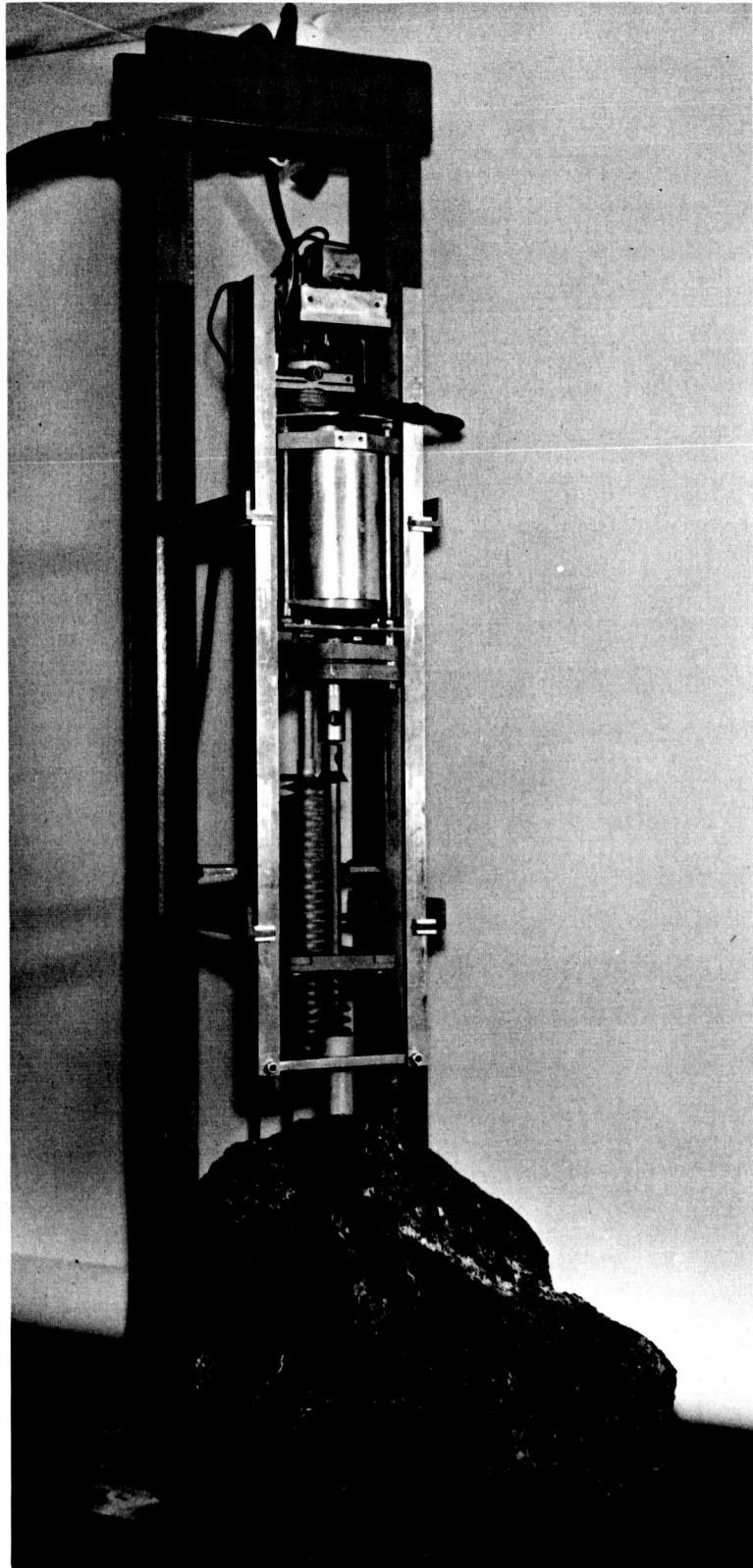
Fig. 10. Extractor subsystem
in operation

2. Extractor bit-cutter assembly. This is an improved version of the helical conveyor mechanism described in the above discussion on sample acquisition and vertical transport. Basically, the mechanism is the same vibratory helical conveyor. However, this extractor has been equipped with (1) a deflector for the delivered sample particles, to minimize delivery losses between the extractor outer tube and the receiving container; (2) a tapered shank designed to fit into the Syntron hammer chuck; (3) exposed flutes at the lower end to assist in the collection and acquisition of the processed sample; and (4) a bit-cutter capable of drilling into hard rock. The mechanism is shown in Figs. 11 and 12.

3. Feed drive motor and cam assembly. This unit provides the linear feed for the hammer-extractor assembly into the particulate surface material and into the bedrock. The cam is shaped to provide the sequential operations of rock cutting and processing as well as sample acquisition and vertical transport. The feed rate defined by the shape and the drive speed of the cam is commensurate with the rate of cutting the rock. The feed rate therefore becomes a function of the hardness of the rock.

4. Feed screw. The hammer-extractor bit assembly travels axially by rotation of the feed screw, which is directly controlled by the feed drive motor and cam assembly. The screw is enclosed in a sleeve and dust-bellows assembly to protect the threads.

5. Guide chassis. The chassis serves as guide rails for the hammer-extractor bit assembly.

6. Support frame. The spacecraft will provide this function.

The subsystem mechanism test rig is also designed to be used in investigating the entire sampling system, since it is designed to accept the sample transfer and presentation subsystem of the continuous-sampling scheme (discussed in Section III-E).

Tests have already been started to operate the mechanism on hard granitic rock and soft pumice rock. Preliminary observations noted are as follows:

1. Granitic rock sampling. Cutting and drilling is satisfactory on an engineering basis. The initial run was made at a feed rate

0   0.25
INCHES
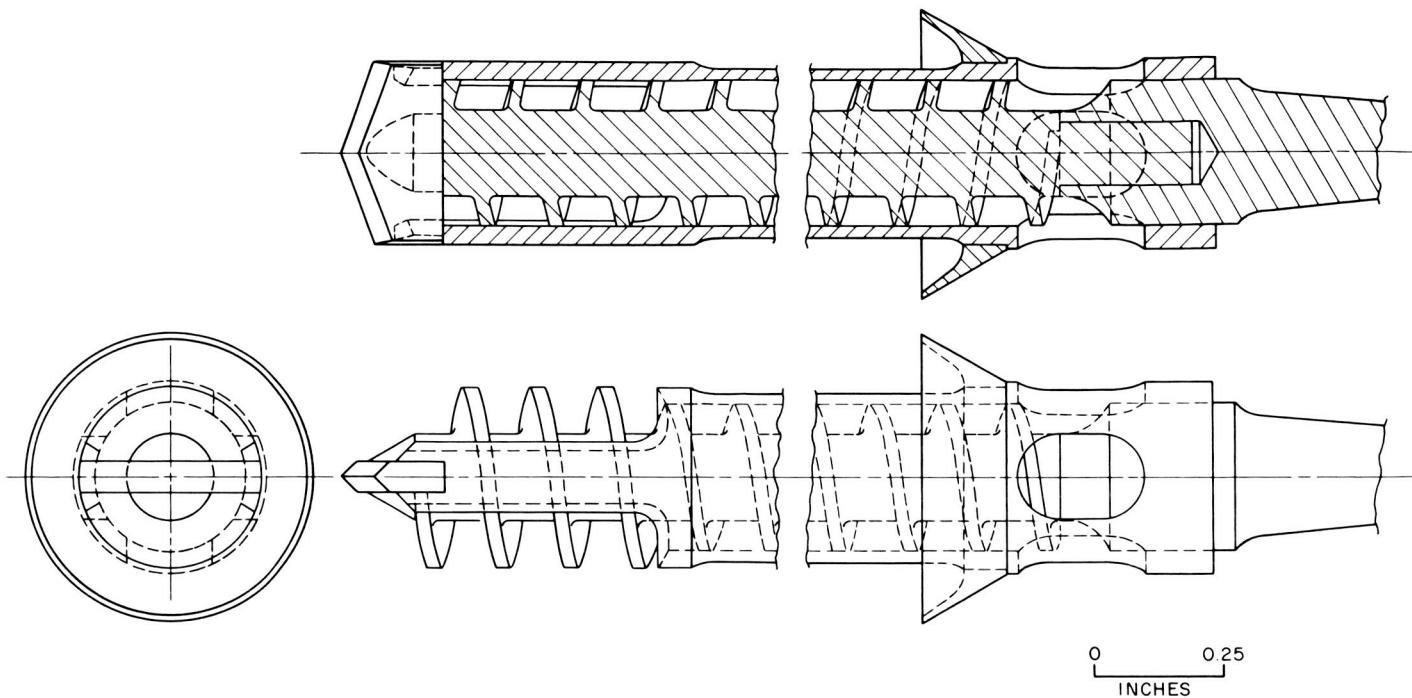
Fig. 11.   Cross section of improved version of extractor bit-cutter assembly
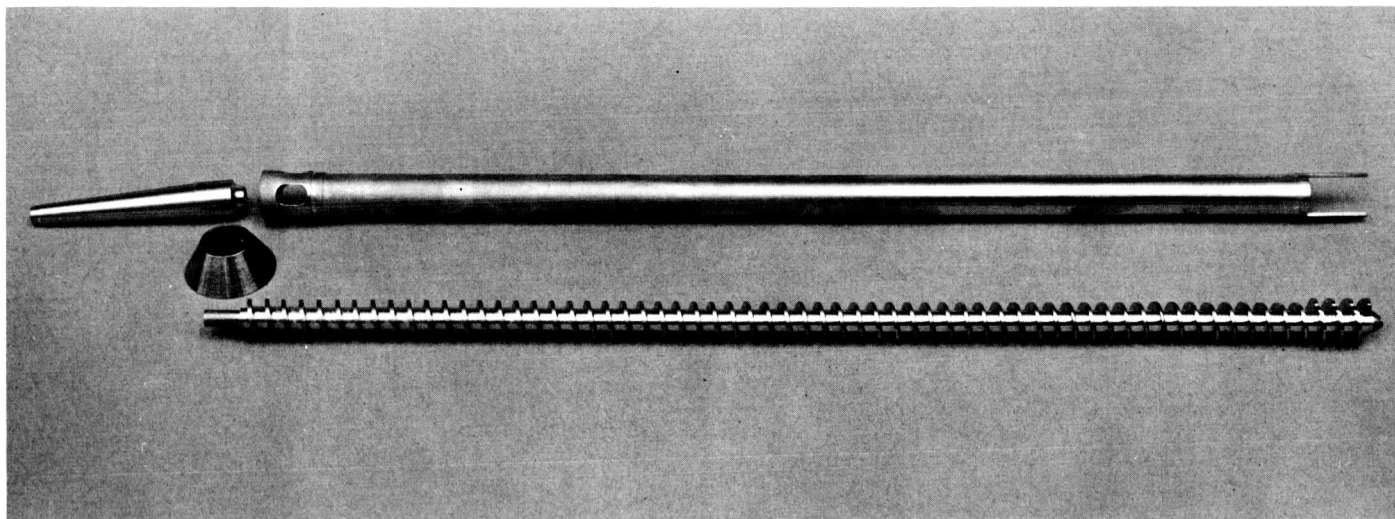
Fig. 12.   Components of extractor bit-cutter assembly

of 0.12 in./min. Sample delivery from the extractor openings commenced at a drill depth of approximately 1.0 in. At a depth of 2.5 in. the total sample transported and delivered from the extractor outlet was approximately 2.2 cm^3. Visual examination of the delivered sample showed that the particles were of uniform, finely pulverized size. No particles larger than 1 mm were observed. X-ray diffractometer analysis of a sample obtained from this test indicated a very satisfactory pattern and no degradation.

2. Pumice rock sampling. Cutting and drilling is very satisfactory on an engineering basis. Sample delivery from the extractor openings commenced at a depth of 1.0 in. The quantity of samples delivered (averaged through three runs) indicated an average depth of approximately 1.5 cm^3/in. and a recorded maximum amount delivered of about 6 cm^3 through a depth of 3.0 in. Visual examination of all samples extracted showed a mixture (unfractionated) containing some relatively coarse flakes and chunks interspersed in a matrix of finely pulverized particles of < 15-μ size. X-ray diffractometer analysis of two samples obtained from separate holes but from the same rock provided very good patterns and indicated satisfactory specimen quality. There was no outstanding difference in quality of the diffractograms for the two specimens analyzed.

Additional testing will be done, and samples collected will be sent for X-ray diffractometer analysis to determine the effectiveness of the entire process. As indicated, this mechanism test rig will be a component in a complete breadboard X-ray diffractometer-sampler system which is being fabricated.

5. Comments

The vibratory extractor approach appears to be a very promising solution to the sample production, acquisition, and transport phases of the sampling problem. However, considerable testing of an engineering prototype in an ultrahigh vacuum and, hopefully, at reduced gravity, must be done before its true potential can be assessed. The engineering prototype would be required to meet the weight, power, and material constraints.

REFERENCES

1. Inett, E. W., Engineering and Mining Journal, August 1956.

2. Paz, M., "Conveying Speed of Vibrating Equipment, " Paper 64-WA/MH-1 presented at the ASME Annual Winter Meeting, New York, November 29 to December 4, 1964. American Society of Mining and Metallurgical Engineers, New York, N. Y.

E. SAMPLE TRANSPORT AND PRESENTATION SYSTEM DESIGN

A. C. Dunk and U. A. Pineda

1. Introduction

Concurrently with the investigations into means of lunar bedrock drilling and sample extraction, a development program is being carried out to produce a mechanism that will transfer and present the sample delivered from the extractor assembly to the X-ray diffractometer (XRD).

The extractor will be assumed to deliver a continuous flow of material from the bottom of the hole to a discharge point above the lunar surface. The block diagrams shown in Figs. 1 and 2 are identical through operation 4, where the material appears at the discharge point from the extractor. The two block diagrams begin to differ at this stage. The transfer and presentation may be either a batch process (discrete-sampling system, see Fig. 1) or a continuous-flow process (continuous-sampling system, see Fig. 2). The sampling operations shown in the block diagrams are described below.

2. Continuous-Sampling Operations

a. Rock drilling. Cutting, chiseling, and/or chipping into the bedrock are means of sampling. The objective involves entry through particulate surface material and cutting into bedrock. The operation is to be done by impact motions, alone, or by combined rotary-impact motions for cutting into hard and/or soft rock.

b. Sample preparation. Preparation includes processing of cut rock by crushing and pulverizing into powder form in order to meet XRD requirements of specimen particle sizes of 100 μ or finer.

c. Acquisition. This phase is the collection of processed rock material (for subsurface specimens) and particulate material (for surface specimens) into a device preparatory to transporting or extracting vertically from the hole.

d. Extraction. Removing, transporting, or conveying the acquired processed material upward from the lunar surface or subsurface to the XRD level is vertical transportation of all collected material.

e. Delivery. This step constitutes discharging all extracted material from the extraction mechanism and dumping it onto a receiving conveyor.
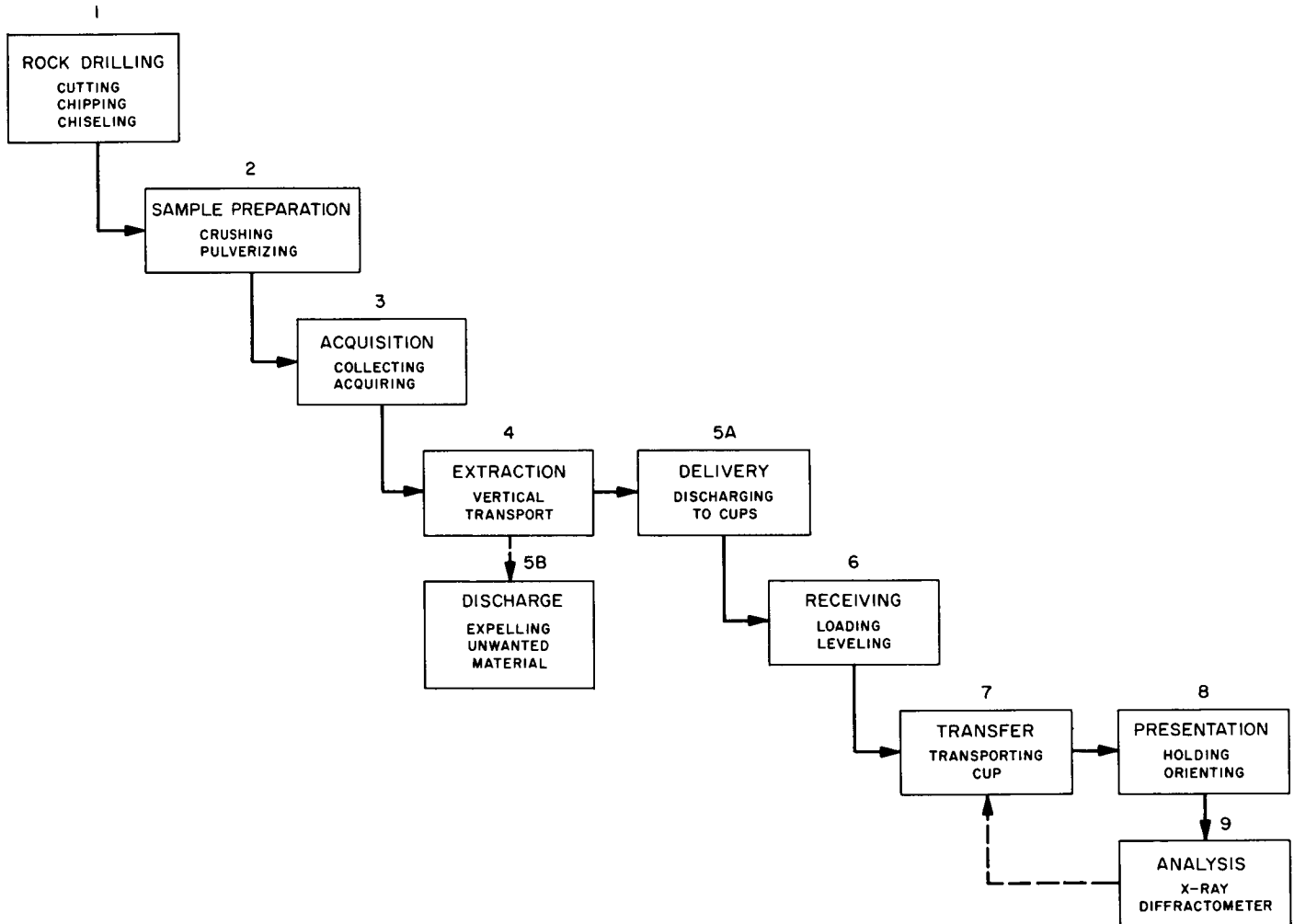
Fig. 1. Block diagram of operations in the lunar-material sampling
system: discrete sampling
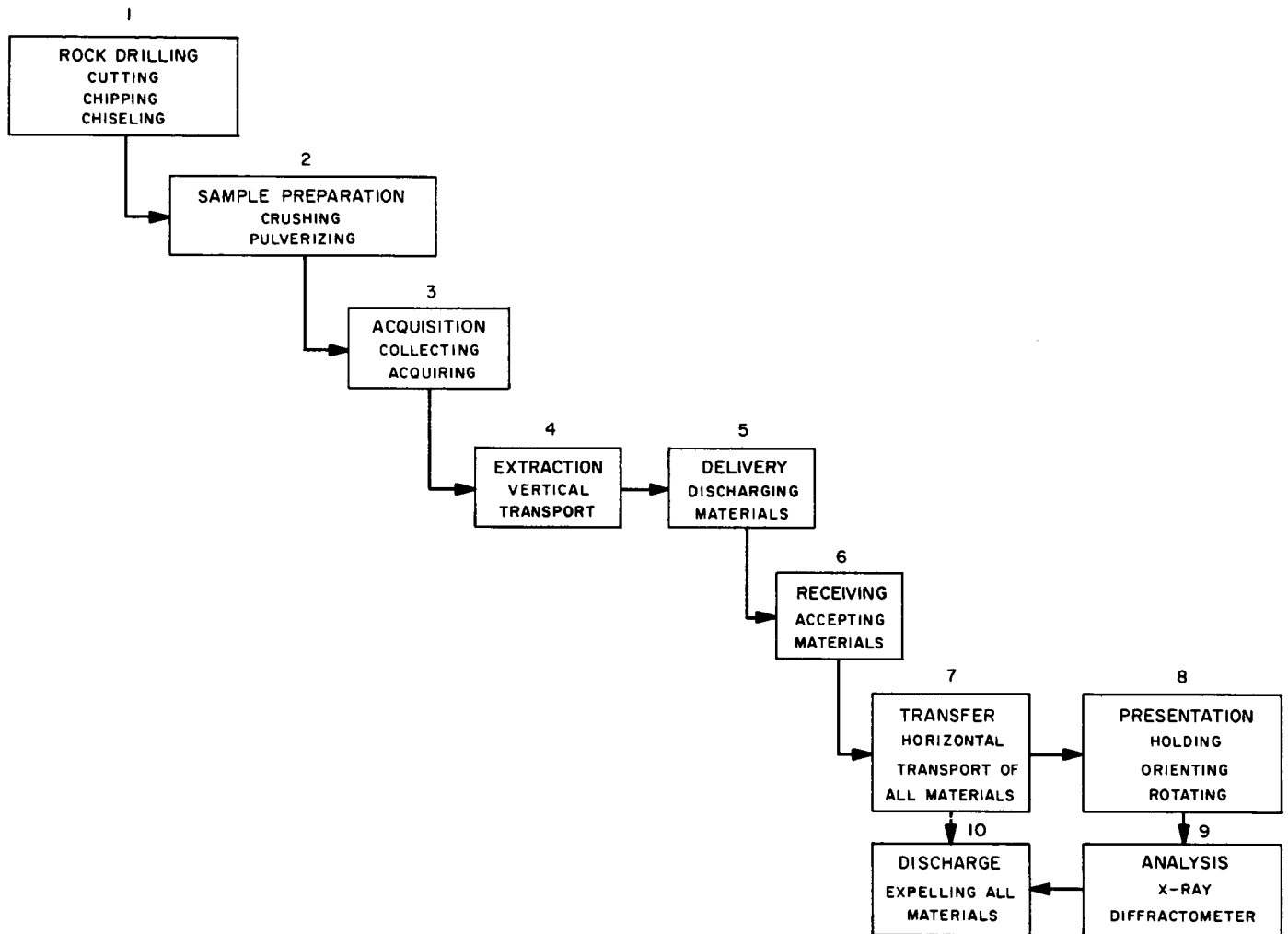
Fig. 2. Block diagram of operations in the lunar-material sampling
system: continuous sampling

f.   Transfer.   This operation involves receiving the lunar sample as it is delivered by the extraction mechanism and conveying the sample to the XRD station then, after the X-ray analysis, discharging the sample from the XRD and sampling systems.

g.   Presentation.   That portion of the lunar sample to be analyzed is held on the XRD viewing station and oriented by rotation through a range of angular positions at a specified rate for scanning by the XRD optics.

h.   Analysis.   The XRD analysis is conducted during the presentation sequence.

i.   Discharge.   Expulsion of all extracted materials, tested or untested, from the system to the environment is accomplished without contaminating the XRD sampling system components and parts.

3.   Discrete-Sampling Operations

In this scheme, the operations of rock drilling, sample preparation, acquisition, and extraction are the same as for those discussed under the description of continuous sampling. Other required operations are the following:

1.   Delivery.   Delivery is either the discharging from the extraction mechanism into separate containers when the discrete sample is required, or the discharging from the extraction mechanism and expelling from the system any collected and extracted lunar material not to be analyzed, without contaminating XRD sampling system components and parts.

2.   Transfer.   Discrete samples in separate cups are carried from the extraction delivery station to the XRD viewing station. The transfer process is reversible (i.e., all sample cups can be transferred to and from delivery and XRD stations. The device carries the Earth-reference sample as well.

3.   Presentation.   Presentation consists of holding the sample on the XRD focusing point and orienting by rotation through a range of angular positions at a specified rate for scanning by the XRD optics. The presentation is coupled to and synchronized with the XRD goniometer motions.

4.   Analysis.   The XRD analysis is conducted during the presentation sequence. Should initial XRD analysis of the lunar sample show an unsatisfactory reading due to insufficient sample in the

container, the transfer mechanism will return the cup and sample to the extractor delivery station for additional material and then carry the cup back to the XRD station for subsequent analysis. This sequence could be repeated several times.

Each approach has its advantages, difficulties, limitations, and disadvantages. The continuous-sampling (presentation scheme) approach permits an unlimited number of samples to be analyzed. It is conceptually simpler and, likely, is simpler to mechanize; however, it requires mechanical redesign of the diffractometer goniometer. It is the authors' opinion that it is unlikely to be seriously affected by fractionation, although contamination may be present. No mechanisms are required for handling sample cups. The problem of providing an Earth-standard sample can be solved, but the solution adds complexity.

The discrete-sampling system can handle the standard Earth-sample problem inherently without additional complexity; however, this approach is definitely limited (in this development program) to three samples, one of which is the standard. The main problems arise with the design of the mechanisms to fill the cups and transfer the cups to the diffractometer. Conceptually, this is a process which is very similar to the manual process of filling sample cups and loading them into the laboratory diffractometer.

4. Continuous-Sampling Mechanism

The design of the mechanism is based on the principle of the vibrating tray for particle conveyance. The tray is designed to receive and convey all the material delivered from the extractor. It will serve, also, as the sample holder for the X-ray diffractometer and, hence, must be designed to have the capability of being rotated through the required 2θ-range diffractometer viewing. The vibratory motion imparted to the tray must convey the particles, provide adequate cleaning of tray surfaces in order to prevent (or maintain at a very low level) contamination between phases of the continuous flow of sample particles, and cause zero fractionation in mixtures of different density shapes and/or particle size.

For the preliminary feasibility investigations and study of the problems of contamination and fractionation, a very simple device consisting of a spring-mounted tray, driven by a solenoid, was put together as shown in Fig. 3. The prime objectives of the tests using this simple assembly were to investigate first, the
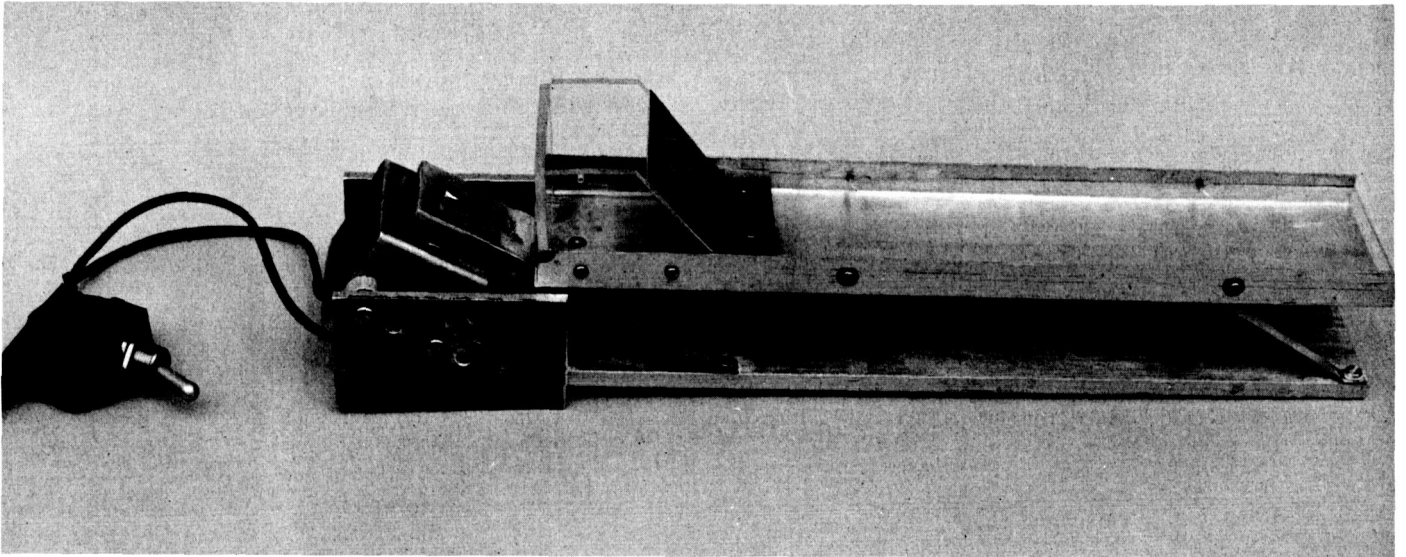
Fig. 3.   Transfer phase of vibrating-tray test rig

feasibility of the vibrating tray as a transfer device and equivalent sample cup, considering all possible spacecraft orientations relative to the local gravity axis; and second, the problems of fractionation and contamination.

Practically all tests relied on visual observations using samples of 20/30-mesh sand and 15-μ quartz. These tests have shown that the vibrating-tray principle is a potential means for sample transfer from the extractor delivery station to the X-ray diffractometer viewing station, even at the possible 15-deg spacecraft tilt. However, its effectiveness and reliability is yet to be determined and demonstrated in a simulated lunar environment. In view of the lack of control and adequate matching of the springs and the solenoid driver, this simple rig is not versatile enough to demonstrate the degree of effectiveness and reliability of such a scheme. However, it is considered that this rig will make it possible to show partial feasibility and give an indication of the extent of fractionation and contamination, if any, to be expected. Moreover, this rig was satisfactory as a means of revealing problems which would require further investigations in the development of this vibrating-tray scheme and as a means of determining whether to proceed with further evaluations using a more complete subsystem assembly.

Visual observations revealed that fractionation (in mixtures of 20/30-mesh sand and 15-μ quartz) and contamination are minimal for low-amplitude vibratory conditions. Insufficient friction between the 20/30-mesh sand particles and the metal surface was observed at high-amplitude vibration, and these particles were not conveyed when the tray was tilted to the 15-deg simulated spacecraft inclination to the local vertical. The very fine-powdered specimens are satisfactorily conveyed over a wide range of amplitudes; however, these fine particles may be subject to the contamination and agglomeration problem with high-amplitude low-frequency vibration modes of operation.

Further tests and more rigorous investigations must be made to evaluate the effectiveness and reliability of this scheme. For this purpose, a more complete assembly, embodying the vibrating-tray approach (in addition to all the required modes), has been designed and is in the final stages of manufacture and assembly. This mechanism, shown in Figs. 4 and 5, consists of the basic tray (with its vibrator drive), spring-mounted on rotatable blocks, and fitted with the required X-ray diffractometer viewing window (beryllium foil). The rotatable blocks are designed to position the tray to the required angle for the diffractometer optical scan. Initially, the rotation will be under manual operation; however, it is intended to have this motion coupled
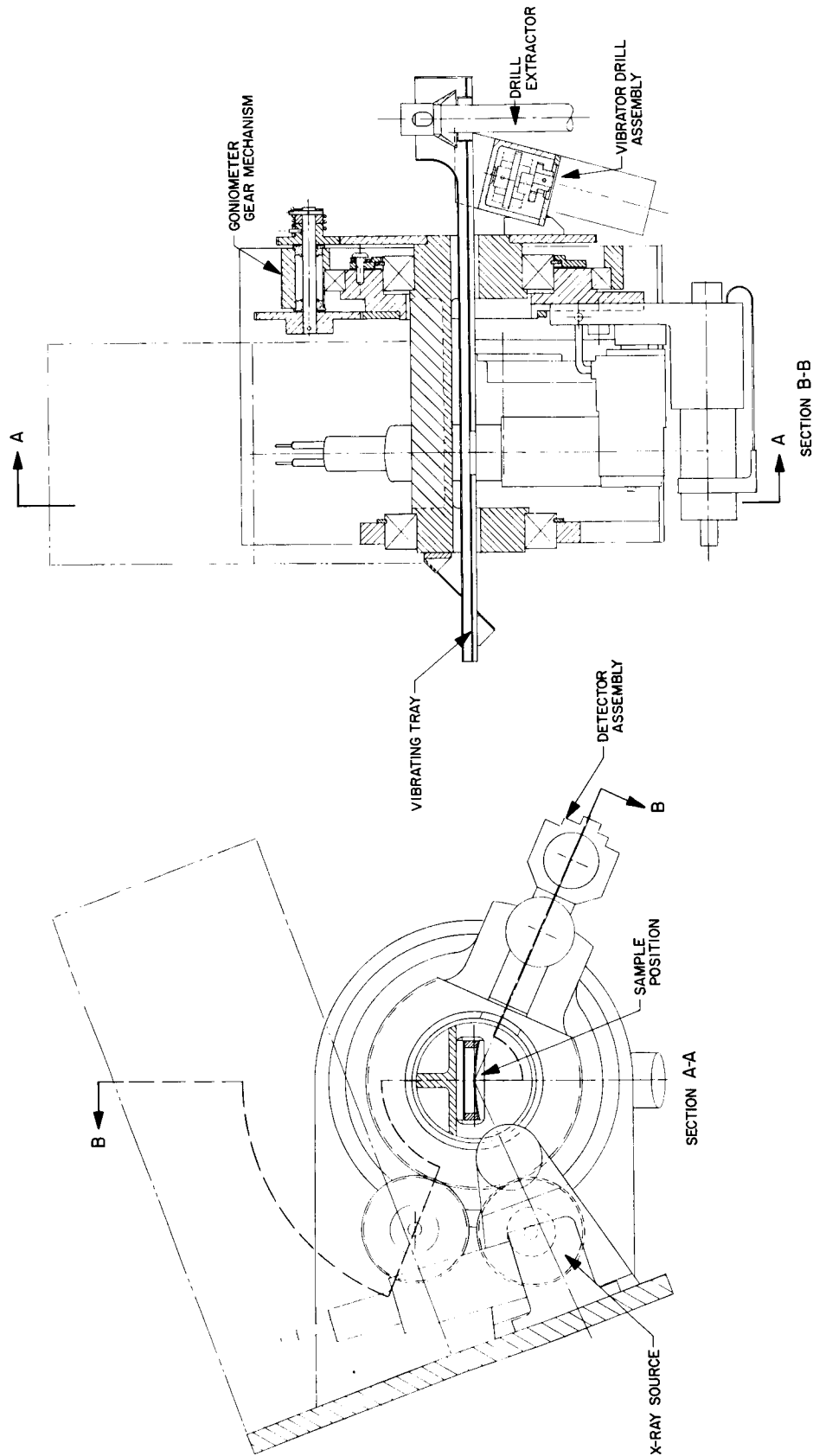
Fig. 4. Cross section of goniometer with transfer and presentation-tray mechanism: continuous sampling system
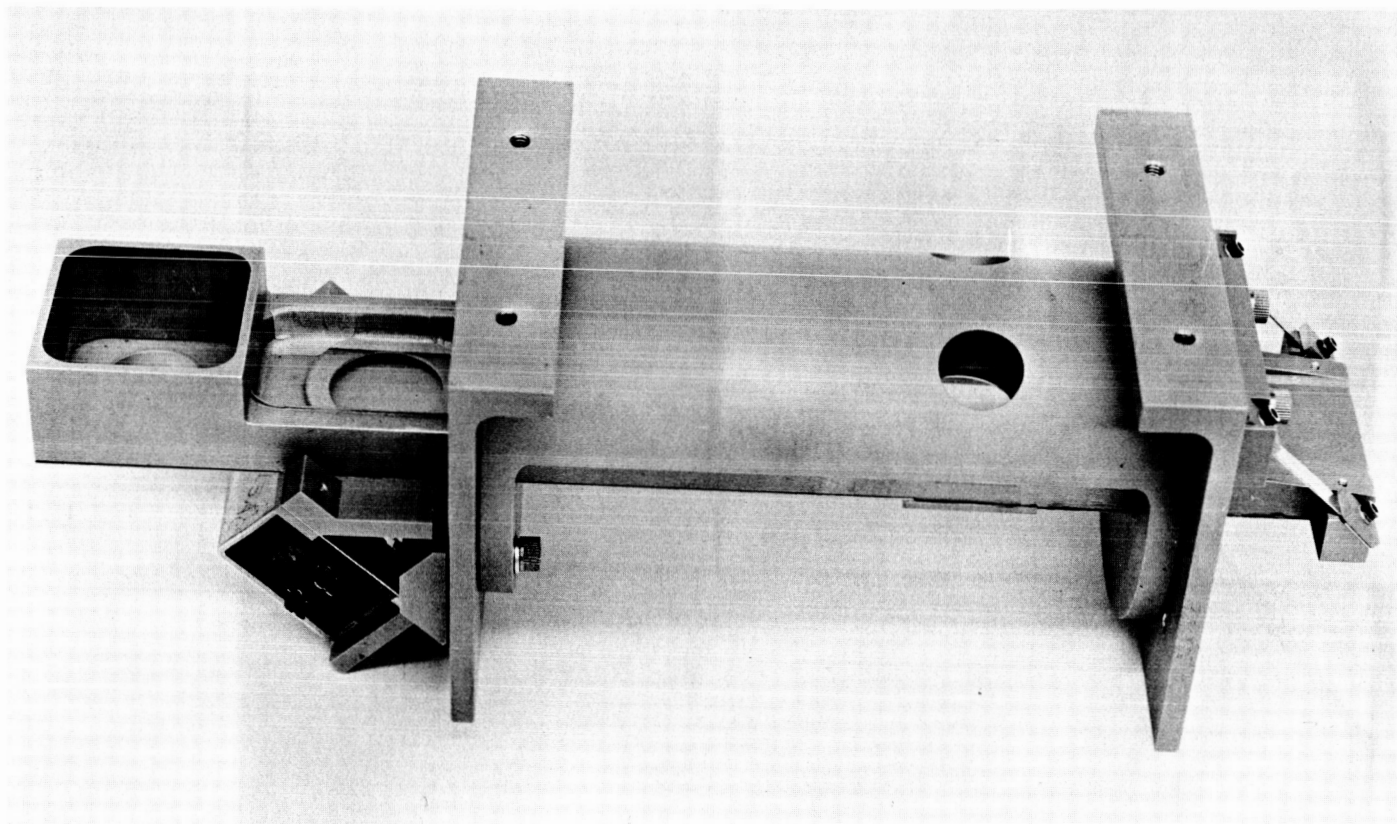
Fig. 5.   Transfer and presentation-tray mechanism assembly:
continuous-sampling system

to the goniometer drive mechanism of the X-ray diffractometer when the complete X-ray diffractometer tests are made. It is the intention of this development program to tie this subassembly to the extractor assembly to complete the lunar material sampling system (see Fig. 6).

The main problems, which are quite obvious at this time, and which will be the principal subject of the investigations, are as follows:

1. Collection of adequate sample material on the beryllium window (The quantity of sample and the sample density over the window area at all possible spacecraft orientations will be measured.)

2. Contamination between samples of a continuous flow of powdered rock and particulate surface material

3. Fractionation of mixtures of different particle densities, shapes, and/or sizes during the transfer sequence

4. Agglomeration of very fine particles

5. Carrying and presentation of Earth-standard samples

6. Compatibility of the required motions for transfer and presentation with those motions of the extractor subsystem mechanisms

7. Accuracy of sample presentation to the X-ray diffractometer

8. Effects of tolerances (dimensional and positioning) on diffractometer tests

In view of the apparent simplicity of the mechanism, an exhaustive study and evaluation of this scheme will be made for its possible use as the transfer and presentation subsystem of the lunar-material sampling system.

5. Discrete-Sampling Mechanism

In this approach the Earth-standard sample will be placed in the diffractometer prior to launch and will remain there until after calibration of the diffractometer at the lunar surface. A separate sampling system will prepare lunar samples in sample cups and subsequently position these cups as required in the sample cup holder on the goniometer of the diffractometer. This approach may have an advantage over the continuous-sampling approach if it becomes necessary to deploy only the sampling system and leave the diffractometer mounted on the spacecraft. This problem of interfacing with the spacecraft will require more study before an optimum choice can be made among the several possible interfacing schemes.
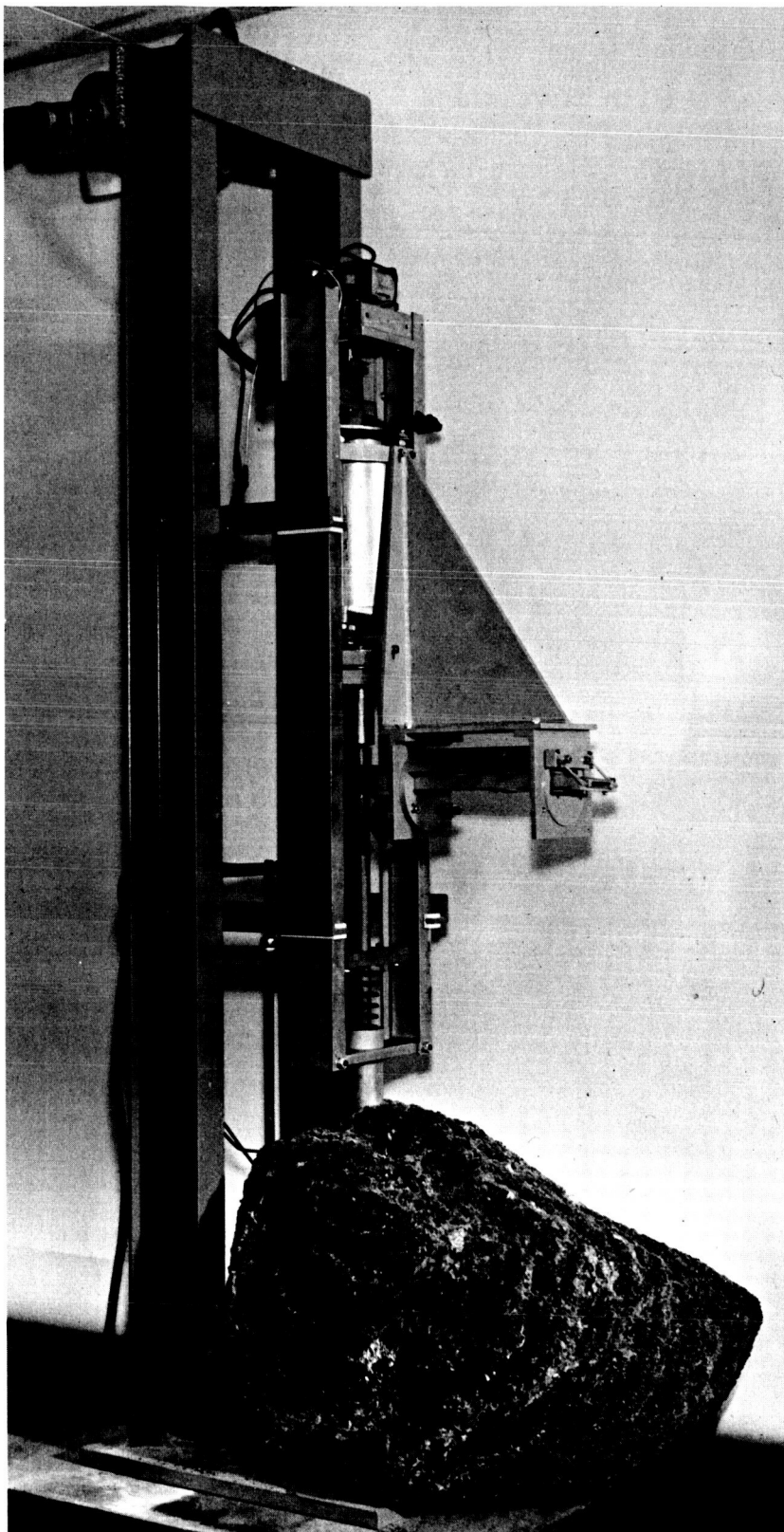
Fig. 6. Complete-sampling system test rig

One approach to a three-sample, discrete-sampling system has been designed; a proposed layout is shown in Fig. 7. This design requires that the diffractometer be deployed to the surface with the sampling system. Other deployment schemes will be studied later.

It is realized that such a scheme will require exhaustive study and evaluation before it is ready for consideration as a transfer and presentation subsystem of the lunar-material sampling system.
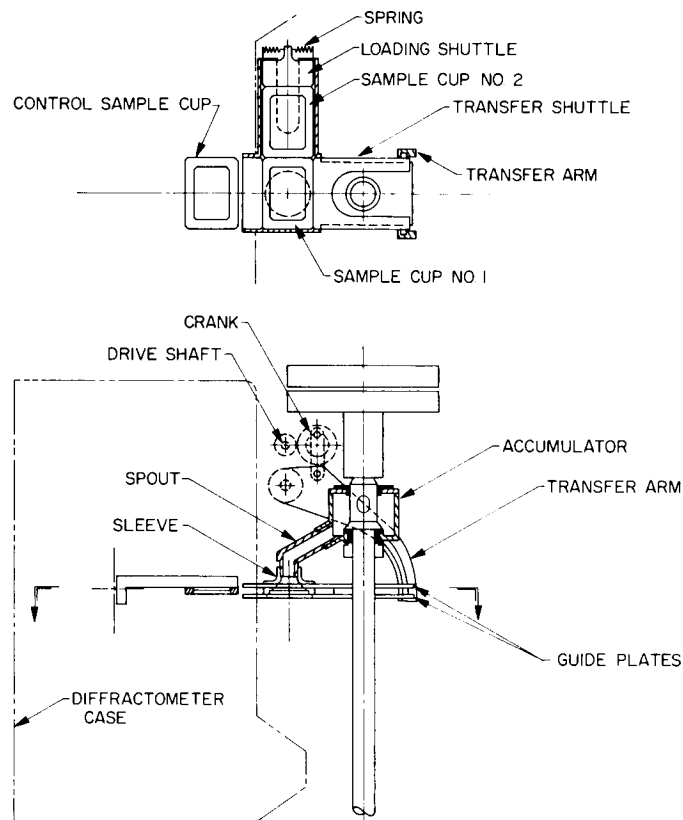
Fig. 7. Discrete-sampling system mechanism

F. PERFORMANCE OF MARK 1 SAMPLER MECHANISMS

D. B. Nash

1. Introduction

Samples prepared by various mechanisms under evaluation for the Mark 1 sampler system were examined to determine the suitability of these devices for preparation of good X-ray samples. The quality of the sample was judged by comparing their X-ray diffraction patterns with diffraction patterns obtained from optimum hand-prepared samples of the same material. Further examinations to determine why some samples were of better quality than others included particle-size analyses, heating experiments, and fractionation tests.

Parametric testing determined the drill bit, drill motions, and drilling rates which produce the best quality and most reproducible X-ray samples from hard rock. Over 200 test drillings were conducted on basalt and, on the basis of X-ray examination of these samples, an optimum set of drilling parameters were chosen; these data are discussed and summarized by Hotz in Section III-A.

2. Particle Size Vs X-Ray Diffraction Quality

The optimum drill parameters were chosen solely on the basis of the X-ray quality (peak intensity, resolution, background intensity) of samples produced by various combinations of parameters. In order to evaluate why certain parameters gave good results and others bad, particle-size analyses were carried out on three representative basalt samples ranging in X-ray quality from poor to very good. The results are summarized in Fig. 1, which shows histograms relating the volume percent of particles in various size-fractions; it can be seen that the best quality sample (top) has the least number of particles in the range < 20 μ.

In further efforts to determine why the sample with the largest percentage of particles below 20 μ gave the poorest X-ray quality, individual size-fractions of each of the three samples were X-rayed and their diffraction patterns compared; comparative data are summarized in Table 1. The results are neither striking nor conclusive because of a lack of comparative data on the original samples of No. 2 and No. 3. However, qualitatively, there is little difference between X-ray quality of bulk sample and individual size-fractions of the sample. In sample No. 2, the size-fractions (< 20, 20 to 30, 30 to 45 μ) give identical X-ray patterns. In sample No. 3, the coarser fractions give somewhat stronger peak intensity on the average than the fine fraction;
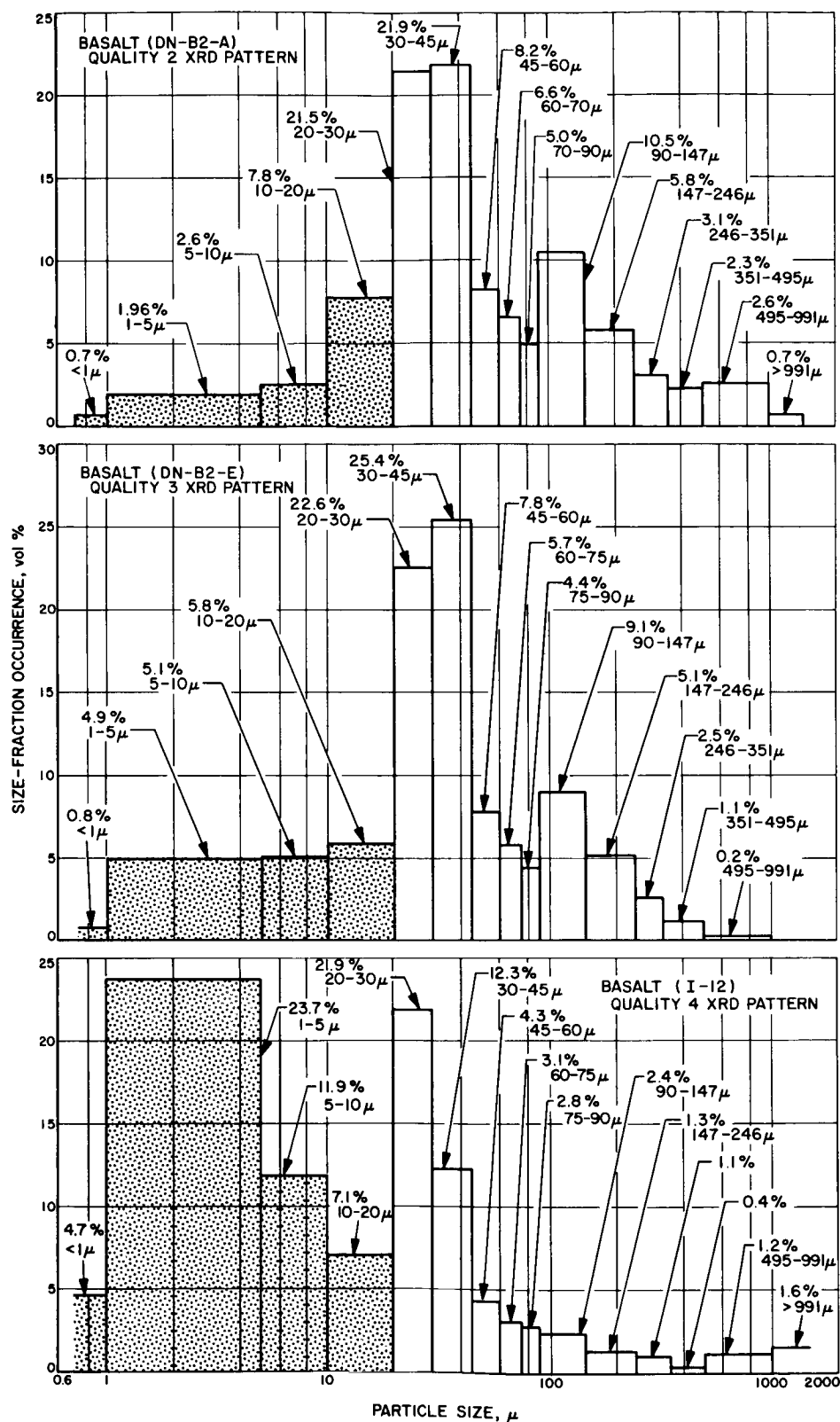
Fig. 1. Particle-size analyses of three basalt
samples: vol % within given size range

Table 1. Comparison of X-ray data quality and particle size for three samples of basalt

Sample No. 2 (DN-B2-A)					
Size fraction	$\dfrac{I_p}{27.7 \text{ deg-}2\theta}$	$\dfrac{I_p}{29.8 \text{ deg-}2\theta}$	$\dfrac{I_b}{29.0 \text{ deg-}2\theta}$	$\dfrac{I_p - I_b}{29.8 \text{ deg-}2\theta}$	Wt % of sample
Original	--	--	--	--	--
< 20 μ	> 200 ⎫	170	50	120	12.4
20-30 μ	> 200 ⎬ Off scale	158	44	114	21.5
30-45 μ	> 200 ⎭	170	40	130	21.9

No significant difference in X-ray quality except increased background with decreasing particle size. Differences in peak intensities equivalent to normal packing error. Comparison of original not possible because of different scalar; however, relative peak intensities appear equivalent.

Sample No. 3 (DN-B2-E)					
Original	--	--	--	--	--
< 20 μ	> 200 ⎫	190	48	142	15.8
20-30 μ	≫ 200 ⎬ Off scale	150	44	106	22.6
30-45 μ	⋙ 200 ⎭	145	42	103	25.4

No significant difference. Increased background in finer fraction due to concentration of magnetite. Qualitatively, 30 to 45 μ fraction gives higher intensity; may be explained by preferred orientation(?). Comparison of original not possible.

Sample No. 4 (I-12)					
Original	172	113	65	107	100.0
< 20 μ	173	132	67	106	42.7
20-30 μ	160	119	65	95	21.9
30-45 μ	189	127	65	124	12.3

No significant difference. Background slightly higher in finer fractions. Original matches < 20 μ-fraction exactly. Qualitatively, the coarser fraction gives best results.

in sample No. 4, there likewise is a tendency for higher peak intensity with the coarser particles. However, these differences are small and could be due to pre-ferred orientation of the primary phase, plagioclase, in the coarser fractions. There is a definite increased, although small, in background intensity with decreasing size-fraction in all three samples; this effect is most likely due to increased Fe-fluorescence from fine-grain magnetite concentrated in the finer fractions during sieving.

These data suggest the following conclusions: (1) poor-quality X-ray patterns result when the drill produces an excessive number of particles <20 μ in size; (2) even in properly comminuted samples, the X-ray results on drill-prepared samples would not be significantly improved by exclusion of particles greater than 20 μ.

3. Effects of High Temperature on Basalt Sample X-Ray Quality

During the initial drill tests with basalt to determine optimum drilling mode and operating parameters, some drill-prepared samples gave poor-quality X-ray patterns (i.e., weak and poorly resolved diffraction peaks). It was considered possible that frictional heating of the sample particles to temperatures around 500°C during the drilling operation may have been the cause. In order to evaluate this premise, sev-eral hand-prepared powdered samples of the basalt test material were heated in an oven (in ceramic crucibles) to temperatures of 400, 600, and 800°C, respectively. They were then X-rayed and their diffraction patterns compared with that of an unheated reference sample. The results are shown in Fig. 2. No change occurred at 400 or 600°C; however, at 800°C the sample reacted with the crucible and formed two new phases, sillimanite and tridymite.

The conclusion that can be drawn from this experiment is that temperatures of around 600°C do not affect powdered basalt samples greatly enough to change their X-ray diffraction characteristics. Thus, temperatures developed during drill-acquisition of basalt X-ray samples could be as high as 600°C for short durations without any damaging effects to the X-ray quality of the sample. It should be made clear, however, that this conclusion applies only to basalt; other rocks, such as those composed of hydrous minerals, could be severely altered by heating to 600°C.

4. Drill-Specimen Quality from Various Rock Types

Since the optimum drill parameters were determined using basalt, only, as a test material, it was necessary to test the versatility of the drill device on other kinds of rock. Ten common rock types were selected which differ in hardness,
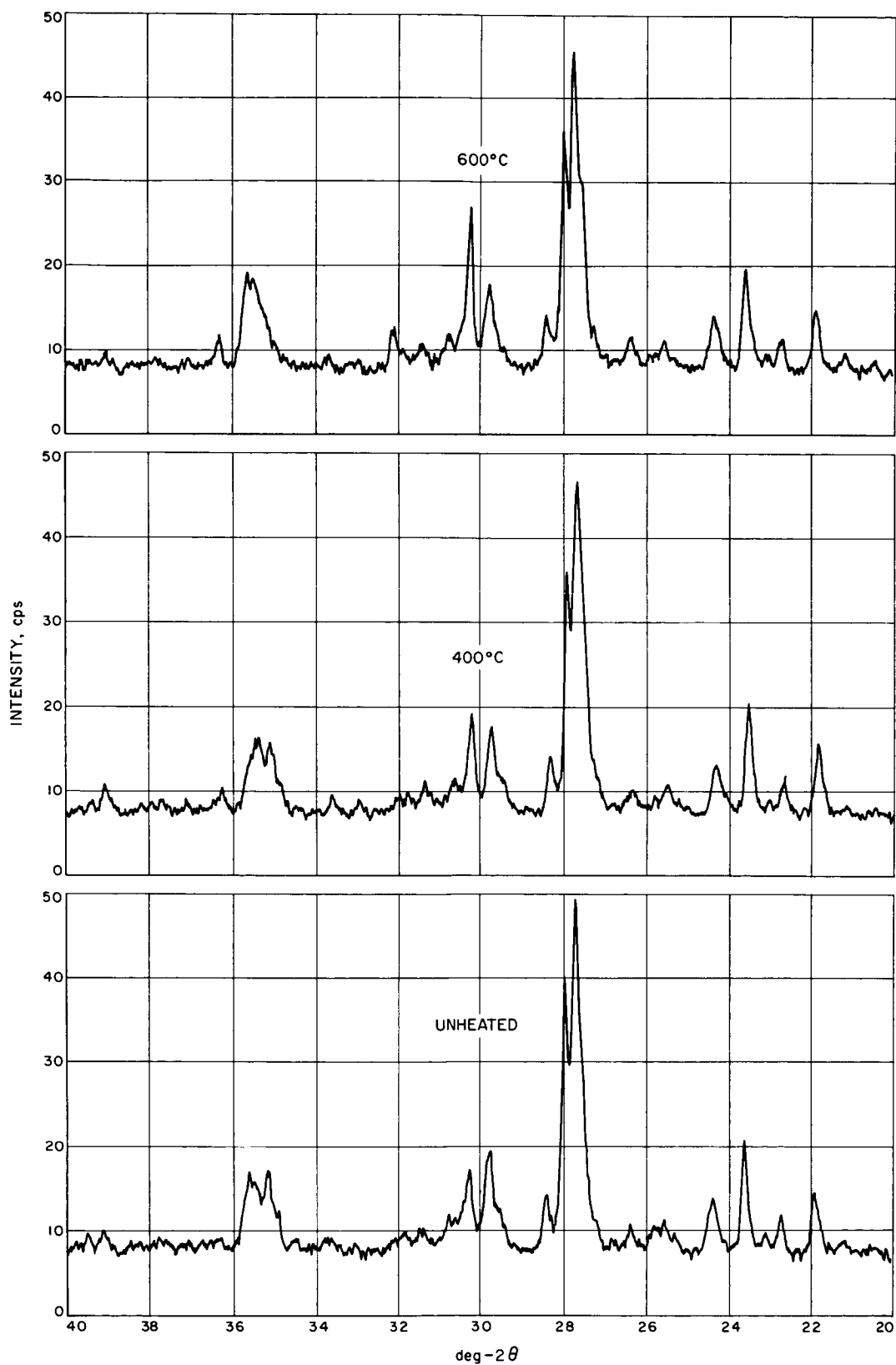
Fig. 2. Comparison of X-ray diffraction patterns of powdered basalt samples at various temperatures

texture, grain-size, porosity, chemical composition, mineral composition, and degree of crystallinity. The rocks selected were: granite, basalt, gabbro, dunite, serpentine, quartzite, pumice, scoria, and marble. Multiple samples were obtained by drilling from each rock type using the following drill parameters:

Drill mode:	combined rotary-impact
Rotation rate:	10 rpm
Impact rate:	160/sec
Load:	20 lb
Cutting edge:	30-deg face, 45-deg cutting angle
Bit material:	carboloy
Bit diameter:	1/2 in.

Three sampling factors were investigated by comparison of the X-ray diffraction patterns obtained from each of the multiple drillings:

1. Comparison of drill-sample XRD pattern with pattern from hand-prepared standard
2. Reproducibility of X-ray data for multiple drillings, each obtained by a freshly sharpened drill bit
3. Degradation of X-ray data quality for five consecutive drillings with the same bit, unsharpened between runs

A summary of the results of these tests is shown in Table 2.

Two principal conclusions can be made from the above comparison of X-ray diffraction patterns. First, on the average, the drill-prepared samples of all the rock types tested are equivalent in quality to the reference hand-prepared samples. In terms of peak-to-background ratios of representative diffraction peaks, the drill samples give values usually within a spread of approximately 15% of the reference, most being inferior to the reference, but some much better.

Second, reproducibility for multiple runs on the same rock was in general excellent, with percent deviation of peak-to-background ratios varying from 2.7% for quartzite to 16% for granite. There was no significant difference in reproducibility between samples prepared by five runs with the same drill and the samples prepared with a freshly sharpened drill for each run; this comparison indicates that the particular drill type used for these tests does not degrade significantly in drilling efficiency with multiple runs, regardless of the rock type sampled.

Table 2. Comparison of X-ray diffraction patterns of rotary-impact drill samples

Rock type	Comparison to reference of multiple runs, Ref = 100%	Comparison of $I_p - I_b$ for multiple runs	
		Three runs with sharp bit each run, % deviation	Five runs with same bit for all runs, % deviation
Granite	83	16	12
Dunite	95	3.4	11
Basalt	66	4.5	9
Gabbro	51	11	
Serpentine	114	5.1	
Quartzite	150	2.7	No
Marble	87	8.5	Data
Scoria	112	6.7	Obtained
Obsidian	93	3.7	
Pumice	100	9.7	
Average	95.3		

5. Penetration Rate and Powder Yield of Rotary-Impact Drill vs Rock Type

Rates of penetration were measured for the rotary-impact drilling mode on ten different rock materials. Drill parameters for these tests were:

1/2-in. No. 883 insert, 30-deg face

Hammer-type bit with 45-to-45-deg edge angle

Impact rate, 160/min

10 rpm

20-lb load

The results are as shown in Table 3.

Table 3. Penetration rates and powder yield rates for rotary-impact drilling on ten different rock materials

Rock type	Penetrated rate, in. /min rate	Average deviation, 3 runs		Powder yield, cm^3/min
		in. /min	%	
Quartzite	0.022	0.001	4.5	0.17
Granite	0.044	0.007	15.9	0.32
Gabbro	0.054	0.006	11.1	0.52
Obsidian	0.055	0.015	27.3	0.32
Dunite	0.055	0.003	5.4	0.47
Basalt	0.061	0.004	6.6	0.41
Serpentine	0.091	0.005	5.5	0.67
Scoria	0.137	0.048	35.0	0.92
Marble	0.200	0.030	15.0	1.5
Pumice	6.20	0.9	14.5	12.9

Penetration-rate data for a given drill mode can be of great use in aiding diagnosis of rock data from the diffractometer; for example, one might be able to distinguish between solid basalt and vesicular scoria, both of which give identical X-ray patterns but, due to different textures, have different penetration resistance. The same would be true for obsidian and pumice.

Considering the yield rates for drilled powder it is possible to determine the drilling time required to yield the 2 cm^3 minimum powder-volume for various rock types for a satisfactory X-ray sample. Time required for ten different rock types are recorded in Table 4.

Table 4. Drilling time for required samples of various rocks

Rock type	Drilling time for 2 cm³, min
Pumice	0.15
Marble	1.34
Scoria	2.18
Serpentine	2.98
Gabbro	3.84
Dunite	4.26
Basalt	4.88
Obsidian	6.26
Granite	6.26
Quartzite	11.6

6. Shapes of Particles Produced by Impact Drilling

Microscopic examination of particles of two basalt samples produced by rotary-impact drilling reveals that not only particles of various sizes are produced, but also particles of various shapes. Three shapes were noticed:

Equant: approximately equal diameter in all directions
Slivers: long and slender, needle-like
Slabs: blade-like, disk-like

A definite particle shape distribution was related to the size distribution of the two samples, as shown in Table 5. The original grain size of the rock was about 100 μ, and this is reflected in the results above; in general, particles in the drilled aggregate of size < 100 μ were equant and monocrystalline, while particles > 100 μ were slivers or slabs and polycrystalline. It is thought that these variations in particle shape have no net effect on the X-ray quality of the samples since, by volume, over 75% of the particles are less than 100 μ in size and are equant. Even though

Table 5. Relationship of particle shape to particle size distributions

Size range, μ	Particle shapes	
	Sample No. 2, (DN-B2-A)	Sample No. 3, (DN-B2-E)
< 20	Equant	Equant
20-30	Equant	Equant
30-45	Equant	Equant
45-60	Equant	Equant
60-75	Equant	Equant
75-90	Equant	Equant
90-147	Most equant, some slivers	Some slivers
147-246	Abundant slivers	Slivers, slabs, equants
246-351	Slivers and slabs	Most slabs, some slivers
351-495	Slabs	Slabs
495-991	Slabs	Slabs
>991	Three large chips	(No particles)

there may be strong preferred orientation of the coarse non-equant particles, the polycrystalline nature of each particle results in no preferred orientation of constituent crystal grains.

7. Fractionation Test of Vibratory Extractor

The vibratory sample extractor device (Dunk and Pineda, Section III-C) was tested for the amount of fractionation it produces in polyphase particle aggregates by operation in prepulverized aggregates of particles with differing density and shape but equal size. The particle parameters and test results are shown in Table 6.

From this test the following conclusions can be made concerning the behavior of particles as they are vibrated up the helical transport column.

Table 6. Comparative fractionation in particles of different densities and shapes: results of test of vibratory sample-extractor device

Material	Shape	Density	Weight ratios quartz/test particle		Fraction-ation, %
			Original	After test	
Quartz	Round	2.7	0.89	1.13	27
Tremolite	Tabular	3.0			
Quartz	Round	2.7	0.63	0.53	14
Rutile	Round	4.2			
Quartz	Round	2.7	0.95	0.64	33
Forsterite	Round	3.2			
Quartz	Round	2.7	5.87	20.5	247
Muscovite	Platy	2.8			

First, for particles of equal size (0.5 to 1.0 mm) and shape, heavier particles are enriched, lighter particles depleted. The degree of fractionation is moderate, with a change in particle ratio of about 15 to 30%.

Second, for particles of equivalent size and density, but different shape, the round grains are enriched, flat grains depleted. The degree of fractionation is moderate to severe; it is moderate for tabular particles (27%), severe for platy particles (247%).

These results, of course, apply only to the particular conditions of this test; further tests should be made with the extractor operating on finer-size particles at various vibration frequencies to determine which vibration mode gives minimum fractionation. If fractionation can be held below an acceptable level (see below), then

the vibrating-column type of sample transport mechanism could be further considered as a possible component for the XRD sampling system.

8. Effects of Fractionation on X-Ray Data and Recommended Fractionation Limit

Fractionation of any kind will give data that do not represent the original rock. In particular, it changes the relative peak intensities of polyphase diffraction patterns; therefore, quantitative determination of phase abundances in the original rock will be erroneous. Other factors besides fractionation, however, can produce similar apparent effects (e. g. , preferred orientation, contamination), and thus it would be unrealistic to require zero fractionation of the sample during preparation if the other factors cannot be controlled to an equivalent accuracy. Thus, even though all sample inadequacies result in cumulative errors in data, some fractionation can be tolerated without degrading the data to an unreliable level. Based on the expected overall accuracy of quantitative determinations, an acceptable level of fractionation for the Mark 1 experiment is about 15% or less. That is, the abundance ratio of any two phases in a polyphase particle aggregate should not be altered by more than 15% during sample acquisition, transport, and transfer.

IV.   ADVANCED DIFFRACTOMETER DEVELOPMENT

A. SEEMANN-BOHLIN OPTICS FOR X-RAY POWDER DIFFRACTOMETRY

J. A. Dunne

1. Introduction

Currently in progress, as a portion of an advanced X-ray diffraction program at the Jet Propulsion Laboratory, is a study of possible optical arrangements for powder diffractometry. The reference arrangement is that presently employed in a flight diffractometer[1] developed for JPL by Parrish at Philips Laboratories [Fig. 1(a)]. The first alternative arrangement to be considered is the focusing diffractometer design [Fig. 1(b)] originally proposed by Arndt (Ref. 2). The Arndt diffractometer utilizes the focusing geometry proposed by Seemann (Ref. 3) and Bohlin (Ref. 4) for powder camera work. A number of Seemann-Bohlin camera configurations have been successfully employed as, for example, those described by Westgren (Ref. 5). With the introduction of the Bragg-Brentano (Ref. 6) parafocusing arrangment by Lindemann and Trost (Ref. 7) and Friedman (Ref. 8), the Arndt diffractometer design was largely abandoned. Successful commercial instruments, such as the Norelco diffractometer developed by Parrish (Ref. 9), have utilized the parafocusing design. The principal disadvantages of the Arndt diffractometer lie in its poor performance at low angles, its mechanical pointing requirements, and the fact that the specimen-to-detector distance varies. The Arndt approach, however, offers two distinct features which are potentially advantageous in a flight diffraction instrument. The first of these is the use of a stationary specimen and source which provides considerable mechanical simplification. Secondly, there is the property that the entire diffractogram is displayed simultaneously on the focusing circle, offering the possibility of large power or time reduction through the use of a continuous or multiple detection scheme. This paper presents the results of a brief investigation of the geometric properties of the Seemann-Bohlin arrangement as compared with the conventional Bragg-Brentano diffractometer design. For a rigorous, theoretical treatment of specimen absorption and line displacements for the Seemann-Bohlin and Bragg-Brentano diffractometers, the reader is referred to a recent article by Kunze (Ref. 10).

---

[1] This device is described in detail by Parrish (paper in preparation) and Speed, et al. (Ref. 1).
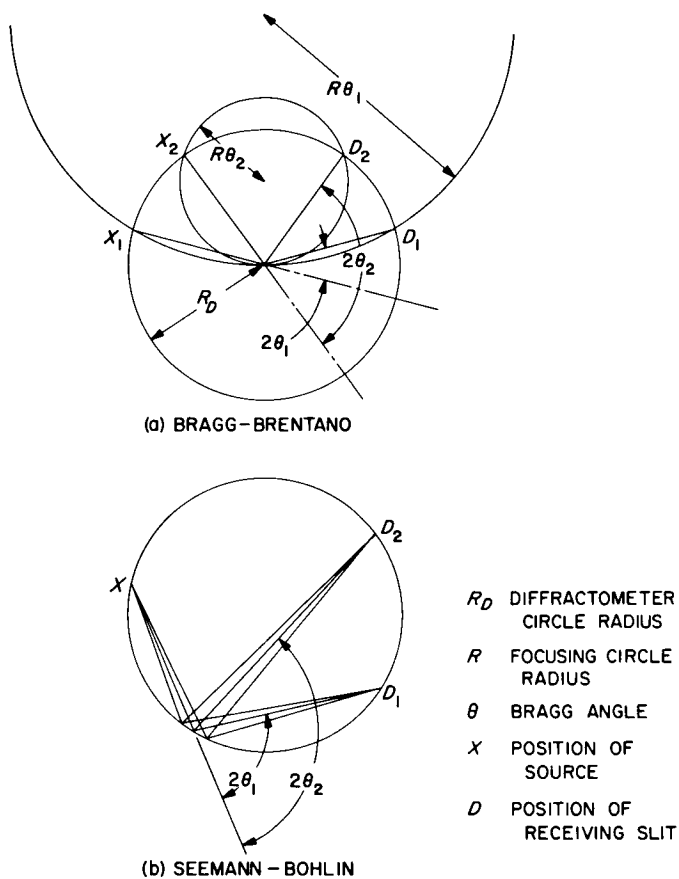
Fig. 1. Diagrammatic representation of the Bragg-Brentano and Seemann-Bohlin X-ray powder diffractometer optical arrangements

2. Resolution Relative to a Bragg-Brentano Diffractometer

The Seemann-Bohlin geometry is shown diagrammatically in Fig. 2. The general feature of the design is the utilization of true focusing in the principal plane of diffraction, which allows a large divergence angle with resultant gains in intensity per unit resolution. That is, the image of the source is formed at all positions along the focusing circle by beams diffracted from the sample. The mean angle of incidence β is defined as the angle made between the line AB and the tangent to the focusing circle at B. The diffraction angle 2θ is measured between the central diffracted ray BC and the central incident ray AB. The central angle BOC can be shown to be related to the Bragg angle θ by the following expression:

$$\psi = (4\theta - 2\beta) \tag{1}$$

The angular resolution of the instrument is considered to be given by

$$\Delta\theta_S = \Delta\theta_s + \Delta\theta_w \tag{2}$$

where $\Delta\theta_s$ is the projection of the source and $\Delta\theta_w$ is the projection of the detector slit on the focusing circle in deg-θ.

In Fig. 3(a) is shown the method for determining the quantity $\Delta\theta_s$ from the relations of the X-ray tube focal spot short dimension f, takeoff angle τ, angle of incidence in the specimen β, and radius of the focusing circle R. The projected size of the focal spot p in a direction normal to the central beam AB is given by

$$p = f \sin \tau \tag{3}$$

The projection of the focal spot on the focusing circle s is given by

$$s = \frac{p}{\sin \beta} \tag{4}$$

This extension in terms of the central ψ is given by

$$\Delta\psi_s = \frac{p}{R \sin \beta} \text{ rad} \tag{5}$$
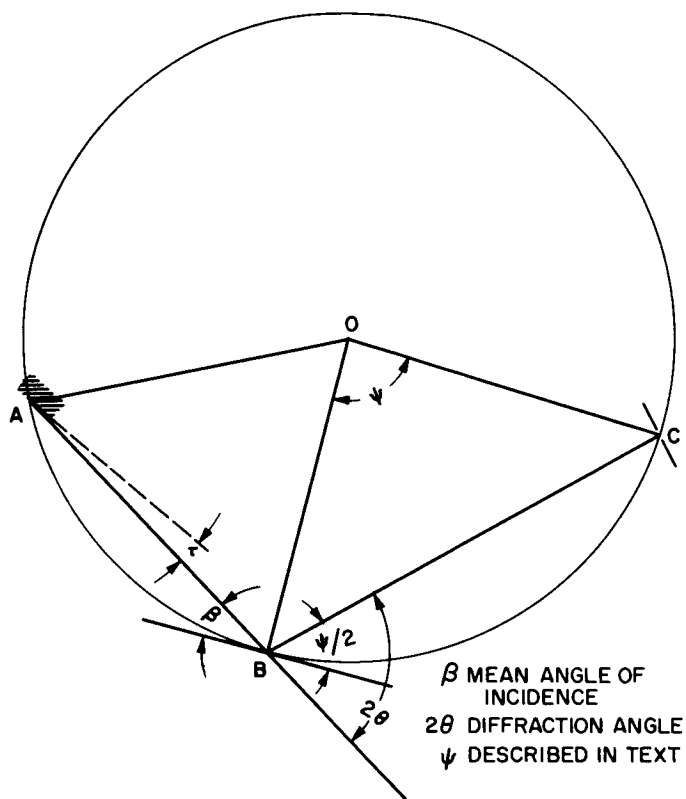
Fig. 2. The Seemann-Bohlin
geometry, defining terms
used in text
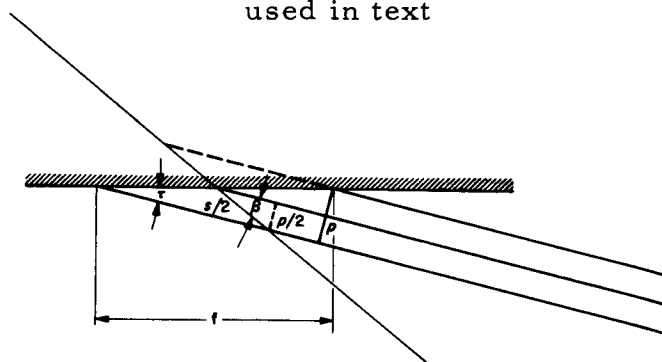
(a) SOURCE EXTENSIONS
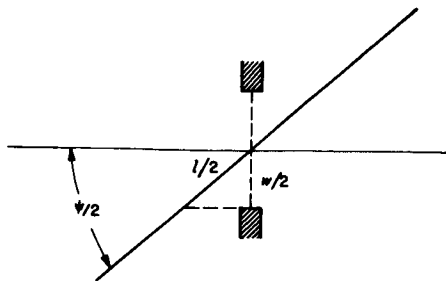
(b) RECEIVING-SLIT EXTENSIONS

Fig. 3. Diagrammatic representation
of the source and receiving-slit
extensions on the focusing
circle for the Seemann-
Bohlin arrangement

By Eq. (1), this extension for the Bragg angle is given by

$$\Delta\theta_s = \frac{p}{4R \sin \beta} \text{ rad} \tag{6}$$

By a similar argument, the receiving-slit extension $\Delta\theta_w$ can be derived [Fig. 3(b)]. The extension of the receiving slit in the focusing circle 1 is related to the slit width w as follows:

$$1 = \frac{w}{\sin (\psi/2)} \tag{7}$$

since $\Delta\psi_w = 1/R$ rad,

$$\Delta\psi_w = \frac{w}{R \sin (\psi/2)} \text{ rad} \tag{8}$$

Again referring to Eq. (4-1) and substituting,

$$\Delta\theta_w = \frac{w}{4R \sin (2\theta - \beta)} \text{ rad} \tag{9}$$

Thus, the angular resolution of the instrument can be expressed as

$$\Delta\theta_S = \frac{w}{4R \sin (2\theta - \beta)} + \frac{p}{4R \sin \beta} \text{ rad} \tag{10}$$

For the Bragg-Brentano geometry, the appropriate relations can be more simply derived:

$$\Delta\theta_s = \frac{p}{2R} \text{ rad} \tag{11}$$

$$\Delta\theta_w = \frac{w}{2R} \text{ rad} \tag{12}$$

and

$$\Delta\theta_B = \frac{p + w}{2R} \text{ rad} \tag{13}$$

Using Eqs. (10) and (13), a comparison between the Seemann-Bohlin and Bragg-Brentano geometries can be derived--i.e., the resolution ratio $\Delta\theta_B/\Delta\theta_S$ as a function of the Bragg angle. A series of curves showing this relationship, with the angle β as the parameter, are given in Fig. 4. In constructing those curves, the same quantities p, w, and R(p = w) were assumed for both geometries.

3. Intensity Ratios

In order to provide an estimate of relative intensities at comparable resolutions, an approximate integrated-intensity ratio, Eq. (14) was derived, based on a strictly geometric argument. The peak-intensity ratio corresponding to a given integrated-intensity ratio can be approximated by the application of the appropriate resolution ratio. The resultant peak-intensity-ratio equation is given in Eq. (15). The calculated peak-intensity ratios will be approximate because of uncertainties as to relative peak symmetries (a θ-dependent function) and the neglect of absorption in the specimen and the air path. It will be noted that the equation predicts the ratio I_S/I_B to attain a maximum at $2\theta = \beta$, while in fact the ratio must be zero due to infinite sample-absorption path length ($2\theta - \beta$ is the angle of emergence of the diffracted ray). This results from the neglect of specimen absorption, the effects of which become profound as 2θ approaches β. In practice, however, 2θ cannot equal β since the receiving slit moves into the sample edge at $2\theta = \beta + a$. An additional increment is added to the minimum attainable 2θ by the shadowing of the receiving slit by the specimen edge. This increment is equal (in deg-2θ) to $w/(4R \sin a)$. In the deviation of Eq. (14), extensions normal to the plane of diffraction were assumed to be equal, and sample receiving-slit and anti scatter slit widths to be appropriate to the Soller-slit vertical divergence angles. X-ray tube power is assumed the same for both instruments.

$$\frac{I_S}{I_B} = \frac{\tan a_S}{\tan a_B} \frac{s'_B}{s'_S} \frac{s''_B}{s''_S} \frac{w_S}{w_B} \times \frac{p_S}{p_B} \frac{\tan d'_S}{\tan d'_B} \frac{\tan d''_S}{\tan d''_B} \tag{14}$$
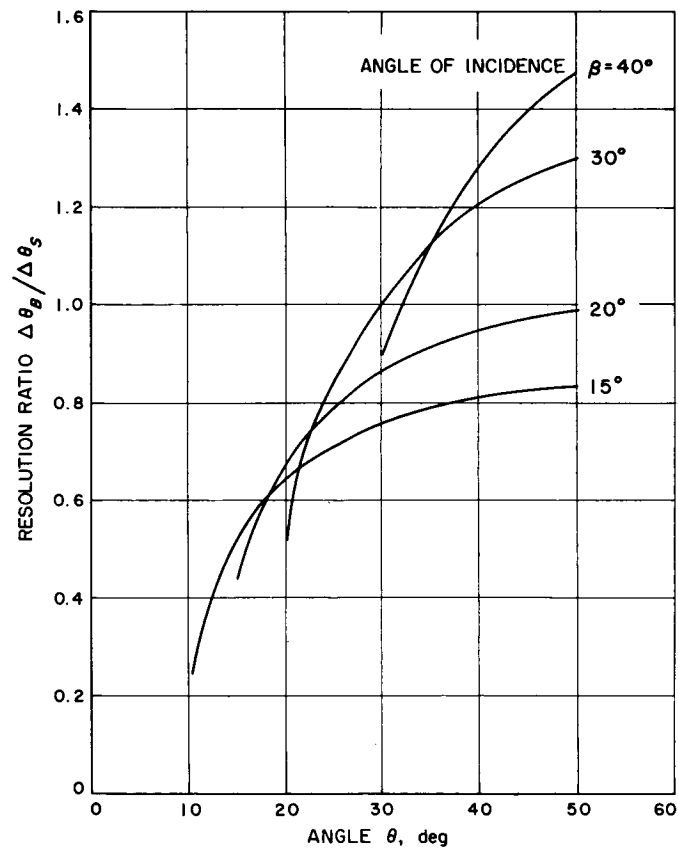
Fig. 4. Resolution ratio $\Delta\theta_B/\Delta\theta_S$
vs θ for β

where

$$\frac{I_S}{I_B} = \text{integrated intensity ratio}$$

a = divergence half-angle

s' = specimen-to-focal-spot distance

   = R_B for Bragg-Brentano

   = $2R_S \sin \beta$ for Seemann-Bohlin

s'' = specimen-to-receiving-slit distance

   = R_B for Bragg-Brentano

   = $2R_S \sin(2\theta - \beta)$ for Seemann-Bohlin

d' = divergence Soller slit half-angle

d'' = receiving Soller slit half-angle

p = projected focal spot width

w = receiving-slit width

β = angle of inclination of mean incident ray to tangent to focusing circle at specimen center

$$\frac{I_S}{I_B} \text{(peak)} = \frac{\tan a_S \tan d'_S \tan d''_S R_B w_S p_S (p_B + w_B)}{\tan a_B \tan d'_B \tan d''_B R_S w_B p_B \left[w_S \sin\beta + p_S \sin(2\theta - \beta) \right]} \qquad (15)$$

Figure 5 is a plot of I_S/I_B and $\Delta\theta_B/\Delta\theta_S$ vs θ with source and receiving-slit size the parameter. In this case, a value of 15 deg was chosen for β, with R, d', d", and w the same for both instruments. In varying the parameters, w was maintained equal to p. In other words, where $w_S = 0.6 w_B$, $p_S = 0.6 p_B$. Divergence angles of 10 and 3 deg were chosen for the Seemann-Bohlin and Bragg-Brentano instruments, respectively.

4. Experimental Data

Experimental comparison was made between instruments of the types discussed above. Table 1 lists the pertinent parameters of the test instruments. Bragg-Brentano data were provided by N. Nickle and were taken on a flight diffractometer of the type described by Parrish (in preparation) and Speed (Ref. 1). Seemann-Bohlin data, provided by A. Metzger and R. A. Shields of JPL, were taken on an Arndt-type diffractometer, constructed under the direction of H. Schnopper of
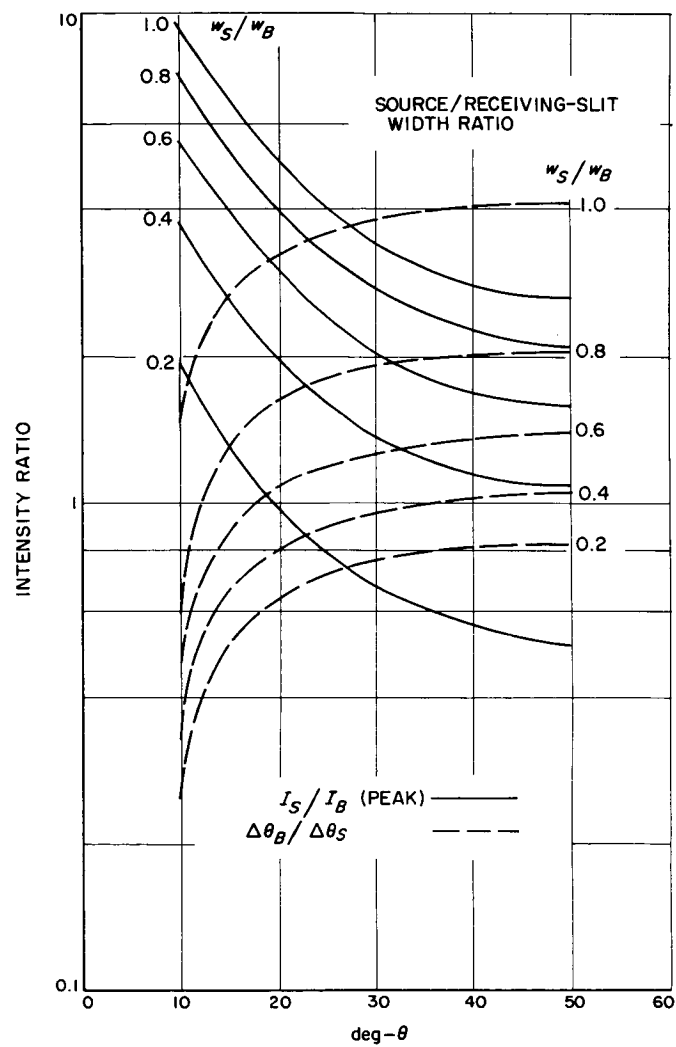
Fig. 5. Intensity ratio I_S/I_B vs θ for source and receiving-slit width ratio for w_S/w_B

Cornell University. Figures 6 and 7 present curves calculated from Eqs. (10), (13), and (15) for resolution and intensity ratios, respectively, using the instrument parameters listed in Table 1. Data points represent the measured values of these ratios. In Fig. 7, peak intensity ratios are plotted against the quantity $\left[(w_S/p_S) \sin\beta + \sin (2\theta - \beta) \right]^{-1}$ for convenience in drawing the calculated curve.

Figure 8 is a plot of observed background intensity vs the quantity $1/\sin^2 (2\theta - \beta)$, and is given to demonstrate the approximate validity of Eq. (17) for emergence angles > 10 deg.

Table 1. Pertinent parameters of the Bragg-Brentano and Seemann-Bohlin instruments

Parameter	Bragg-Brentano	Seemann-Bohlin
R, in.	3.35	5.0
w, in.	0.006	0.014
f, cm	0.04	0.04
τ, deg	8	6.3
β, deg	--	15
d', deg	2.32	7.2
d", deg	2.32	1.25
a, deg	1.7	4.8

5. Background Intensity

Based on the assumption that background intensity will vary inversely as the solid angle subtended by the receiving slit with respect to the specimen, the Seemann-Bohlin diffractometer background intensity should increase sharply with decreasing 2θ angle. In other words, background intensity for the Seemann-Bohlin diffractometer should be given by an expression of the following form

$$I_{b_S} = \frac{K}{s'^2} \tag{16}$$
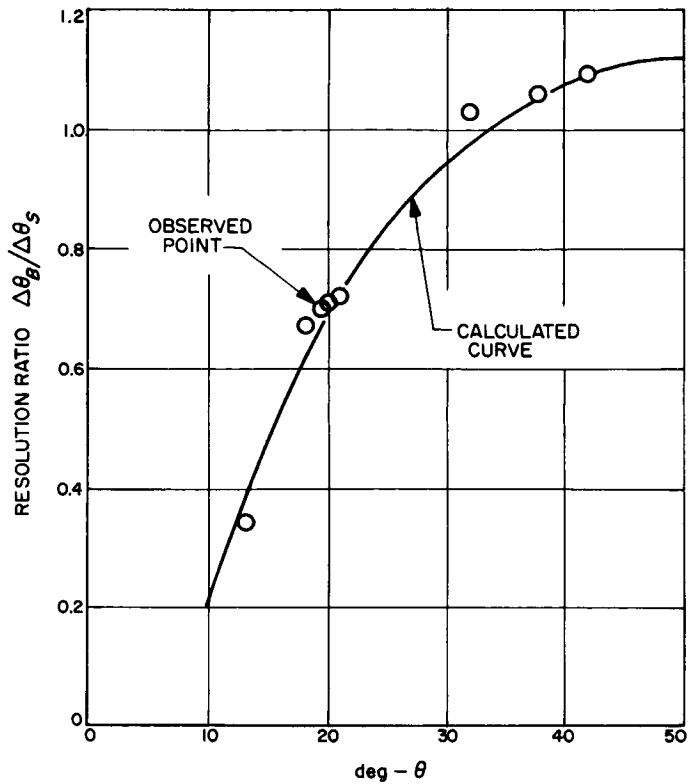
Fig. 6. Observed and calculated
intensity ratio vs θ for the
instrument parameters
listed in Table 1
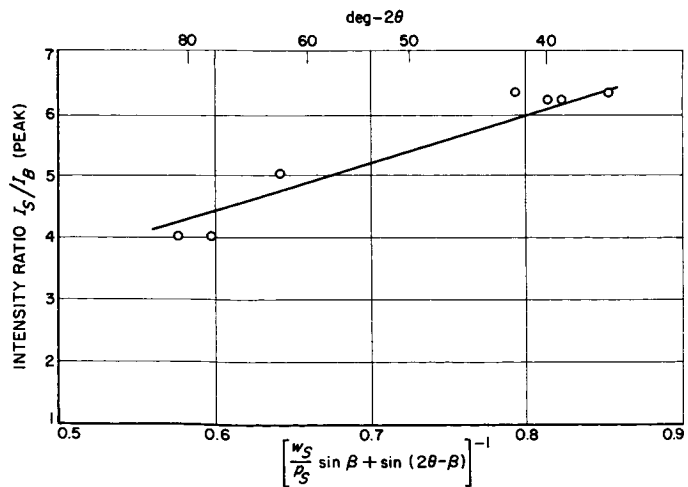
Fig. 7. Observed and calculated
intensity ratio vs $[(w_S/p_S)\ \sin\beta$
$+\ \sin\ (2\theta - \beta)]^{-1}$ for the
instrument parameters
listed in Table 1
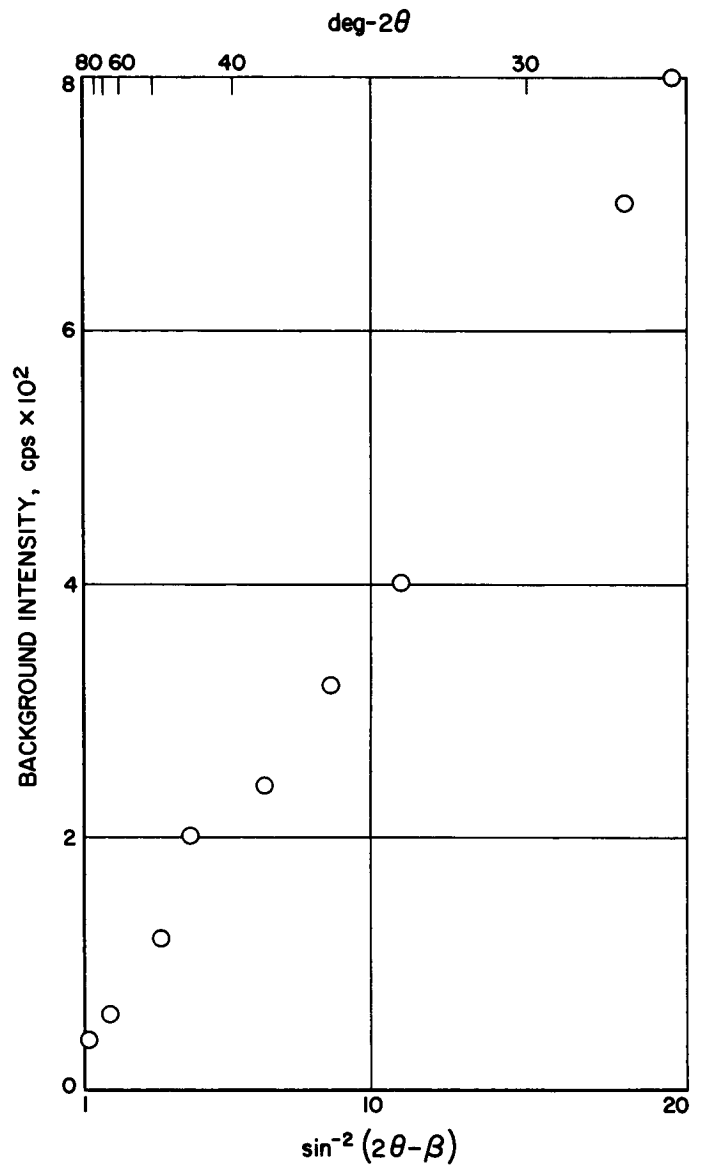
Fig. 8. Observed background
intensity data from Seemann-
Bohlin instrument (Table 1)
vs $\sin^{-2}(2\theta - \beta)$

When s' is as defined above $\left[= 2R_s \sin(2\theta - \beta)\right]$, the expression becomes

$$I_{b_s} = \frac{K^1}{\sin^2(2\theta - \beta)} \qquad (17)$$

with the constant of proportionality K^1 including the pertinent instrument and excitation parameters. As in the case of Eq. (15), the expression becomes increasingly inaccurate as 2θ approaches β, since the specimen cannot be considered a Lambert's law radiator.

6. The Low-Angle Problem

The optimum d-spacing range for the geological diffraction instrument is approximately 14 to 1.4 Å, which embraces the diagnostic peaks of major rock-forming and principal accessory minerals. This corresponds to an angular range (in deg-2θ) between 6 and 68 for CuK$_\alpha$, between 9 and 110 for CrK$_\alpha$ and between 11 and 157 for TiK$_\alpha$. At the sacrifice of information on the sheet silicates, silicate glasses, and a number of hydrous phases, one could consider a marginal range of 4.5 to 1.4 Å, giving a minimum 2θ of 20, 32, and 35 deg for Cu, Cr, and Ti, respectively. Further reduction of the observable 2θ range would result in data of questionable value in rock analysis. It is evident, then, that the ideal device for rock analysis should be capable of low Bragg-angle performance. Some idea as to the difficulty in adapting the Seemann-Bohlin geometry to this requirement can be obtained by the following example. In order to achieve resolution comparable with that of a Bragg-Brentano device of the same mechanical radius at 20 deg-2θ, β must be minimized and a correspondingly reduced, due to the small focal spot-to-specimen distance. Using values for β and a of 7 deg and 1/2 deg, respectively, with the resolution ratio set equal to 1 at 20 deg-2θ, the source and receiving-slit width ratio becomes 0.317, resulting in an intensity ratio as low as 0.2 at 50 deg-2θ. In short, it is clear that the requirement for optimum low-angle performance compromises the Seemann-Bohlin instrument. In fact, it would appear that a minimum 2θ cutoff of 20 deg is nearly at the limit of profitable utilization of this geometry in single detector powder diffractometry. There is, however, the possibility of developing some form of detector mechanism that would allow simultaneous detection of the diffractogram displayed on the Seemann-Bohlin focusing circle. If we assume the size of the detecting element to be equivalent to the width of the conventionally employed

receiving slit, the technique offers a power-time gain $R_\theta/\Delta\theta_w$, where R_θ is the scan range and $\Delta\theta_w$ is the width of the receiving slit in θ. For a scan range of 30 and a $\Delta\theta_w$ of 0.05 deg-θ, this becomes a gain for 600. An instrument offering simultaneous detection capability, then, could be slower by an order of magnitude than a competing device on a single detector basis, and still offer a power-time gain of 60; i.e., a diffractogram could be obtained in 1/60 the time using the same power, or in the same time using 1/60 the power. Simultaneous detection, however, clearly requires a technological breakthrough in the detector area. Short of this, there remains the " brute-force" approach of multiple detection, where the power-time gain is given by the number of detectors employed times the ratio of the speeds of the diffraction systems.

REFERENCES

1. Speed, R., et al., *Advances in X-Ray Analysis*, Vol. 8, Plenum Press, New York (in press).

2. Arndt, V. W., Ph.D. Dissertation, University of Cambridge, 1948.

3. Seemann, H., *Annalen der Physik* (Leipzig), Vol. 59, 1919, p. 455.

4. Bohlin, H., *Annalen der Physik* (Leipzig), Vol. 61, 1920, p. 421.

5. Westgren, S. F., *Transactions of the American Institute of Mining and Metallurgical Engineers*, Vol. 93, 1931, p. 13.

6. Brentano, J. C. M., *Proceedings of the Physical Society* (London), Vol. 37, 1925, p. 184.

7. Lindemann, R., and Trost, A., *Zeitschrift für Physik*, Vol. 115, 1940, p. 456.

8. Friedman, H., *Electronics*, Vol. 18, 1945, p. 132.

9. Parrish, W., *Science*, Vol. 110, 1949, p. 368.

10. Kunze, G., *Zeitschrift für Angewandte Physik*, Vol. 17, 1964, p. 522.

N65-34964

B. PRELIMINARY INVESTIGATION OF THE FEASIBILITY OF A RADIOISOTOPE
X-RAY SOURCE

J. A. Dunne

The present flight X-ray diffraction system employs a scaled-down version of a conventional X-ray diffraction tube as a source of X-rays. The production of X-rays by interaction of an electron beam with a metal target requires the application of a sizable accelerating potential across the tube in order to provide the charged particles with sufficient energy to photo-ionize the target atoms. In the case of CuK radiation, a minimum potential of 8.9 kV is required. Further, the efficient production of line spectra requires over-voltages in the order of two or three times the critical potential, and, as a result, a voltage on the order of 25 kV must be used for a Cu target X-ray tube. The major power user in the diffractometer system is the X-ray tube. Twenty-five watts is the theoretical minimum using the present X-ray optical design, neglecting power-supply efficiency losses and filament dissipation. Clearly, elimination of the X-ray tube would represent the maximum imaginable improvement in the diffractometer's engineering profile, not only in terms of power but, by the elimination of the 25-kV potential, reliability as well. Interest in a radioisotope X-ray source is based on this argument.

The first consideration here is the determination of the X-ray flux required (i. e. , the flux produced by the present conventional X-ray tube). Table 1 lists the results of three measurements and one calculation of the flux produced in a conventional tube at 25 kV, 1 mA. The roentgen output measurement was conducted at 50 kV, 20 mA; and has been extrapolated down to 25 kV, 1 mA on a $1/V^2 i$ basis, where V is accelerating potential and i is beam current. The measurement by N. Nickle was made on a lunar diffraction tube mounted in a standard Norelco diffraction goniometer; the data were corrected for attenuator-foil absorption and two geometrical factors, detector aperture size and Soller collimator angular aperture. The writer's first measurement was made on a standard Norelco diffraction tube using a 0.014-in. aperture in a 0.010-in. cold-rolled steel plate located 14-3/8 in. from the X-ray tube target. This measurement was corrected for attenuator foil absorption and geometrical factors.

The second of the writer's measurements consisted of a determination of the efficiency of diffraction of the incident beam by a quartz powder. The ratio of the integrated intensities of the incident and diffracted beams (measured at low power)

was found to be 2×10^{-5}. This ratio was then applied to the intensity normally observed in the lunar diffractometer. The mean beam flux so derived was then corrected for the pertinent geometrical factors, with the resultant 4π flux shown in Table 1. The efficiency calculation shown for comparison is valid only for the continuous spectrum,

Table 1. Values for 4π flux for Cu target X-ray tube operated at 25 kV, 1 mA

Roentgen output[a]	Photons/sec			
	Nickle	Dunne(1)	Dunne(2)	Continuum efficiency calculation
1×10^{13}	1×10^{12}	6×10^{12}	3×10^{12}	4×10^{12}

[a]Personal communication from Dr. S. Wytzes, Philips Gloeilampenfabrieken, Einhoven, Netherlands

and is included on the assumption that the line spectrum integrated intensity is approximately equal to that of the continuum for a Cu target at 25 kV.

The data in Table 1, although of questionable precision, suggest that a 4π flux in the 10^{12} to 10^{13} photon/sec range is necessary in order to match present diffractometer performance. The small allowable size of the source (i.e., in the order of the conventional focal spot dimension of 1×10 mm) places a serious constraint on the usable volume for K-capture sources. The result is that approximately 2×10^{2} curies in a volume of 10^{-3} cm^{3} is needed, necessitating a specific activity exceeding 10^{4} C/g. Isotopically pure Fe^{55} would come within an order of magnitude of this figure, but the listed specific activity of commercially available Fe^{55} indicates a concentration of the isotope of about one part in 10^{3}. Thus, the production of a source with around 1/5 of the conventional source flux would require an enrichment of commercially available Fe^{55} by 10^{3}.

Assuming such an enrichment process could be made 1% efficient, the cost of the resulting source would exceed $2 million in material alone, based on the commercial rate listed for the isotope. For direct production of a source of the appropriate strength, an isotopic concentration of Fe^{54} followed by activation for one year in a thermal neutron flux exceeding 10^{16} n/cm^{2}/sec is indicated. Although capable of

producing a sufficient rate of VK_α X-rays to satisfy the 4π flux requirements. ($> 3 \times 10^{13}$) protons/sec from target volume), Cr^{51} suffers from two drawbacks First of all, its spectrum also includes 300 keV γ radiation (about 9%). Second, the production of this isotope would require the isotopic separation of Cr^{50} (about 4% natural abundance) followed by a 3.1-month irradiation in a thermal neutron flux of 2×10^{17} $n/cm^2/sec$. Another approach to the problem might lie in the use of a β emitter as the source of electrons of appropriate energy to excite a transition metal target. It seems possible, in principle, to magnetically focus the β energy emitted over a large surface area onto a target area the size of the present focal spot. The difficulty is that the volume capable of producing nearly monoenergetic electrons is quite small, since electrons suffer energy losses in traversing matter and, therefore, monoenergetic electrons would be collected from a depth of only a few tens of angstroms. Tritiated αTi, for example, could be expected to produce enough 18-keV electrons to compete with a conventional source only if electrons could be collected from a surface area of around 10^7 cm^2. Direct introduction of H^3 into Cu (cuprous hydride), on the other hand, would produce a 4π flux of only 10^8 photons/sec.

On the basis of the preliminary calculations outlined above, the feasibility of the development of a radioisotope source suitable for use in a lunar X-ray diffractometer does not appear promising. However, investigation of this problem will continue in light of the impact such a development could have on spacecraft diffraction instrumentation.

N65-34965

C. TOTAL IRON ANALYSIS BY ANCILLARY NON-DISPERSIVE X-RAY FLUORESCENCE INSTRUMENTATION

J. A. Dunne

This article describes some preliminary investigations of the feasibility of total Fe analysis by non-dispersive X-ray fluorescence detection in an X-ray diff-ractometer. The primary radiation employed in the present lunar diffractometer, CuK_α, lies just on the short wavelength side of the FeK absorption edge, with the result that the efficiency of production of Fe fluorescence radiation in the diffraction sample is high. This same relationship also allows efficient discrimination against CuK_α scattered from the sample by the use of an Fe foil filter over the detector aperture.

The experimental arrangement employed in the fluorescence analysis meas-urements is shown in Fig. 1. An 0.015-in. Fe foil filter is held in position by a diffraction-slit cap cut out to a 1/2-in.-diam circular aperture. Figure 2 presents the data on the basis of which the foil thickness was chosen. The Fe/Q ratio repre-sents the ratio of measured intensity from Fe_2O_3 and quartz samples, respectively. The turnover in the Fe/Q ratio with foil thickness is caused by the increase of scattered hard continuum intensity relative to FeK_α. The mass absorption coefficient of Fe is about 30% lower for 16-keV photons (continuum peak) than for FeK_α photons. With a scintillation counter, there is some overlap between FeK_α and hard continuum pulse-amplitude distributions; the pulse height analyzer (PHA) is not entirely effective in removing the latter. It is evident, then, that the employment of a gas proportional detector and pulse height analyzer would push the Fe/Q ratio turnover to higher foil thickness, with an accompanying increase in achievable contrast.

Figure 3 shows fluorescence data collected on mixtures of Fe_2O_3 and quartz, with observed fluorescence intensity plotted against wt% Fe_2O_3. The arrangement shown in Fig. 1 was used, with a 0.0015-in. Fe filter foil and pulse height analyzer. The Cu target X-ray tube was operated at 25 kV constant potential, and 2 ma, using a 1-deg divergence angle and sample inclination of 40 deg (80 deg-2θ). The intensities shown in Fig. 3 should be considerably lower than those achievable on the present lunar instrument at 25 kV constant potential and 1 mA, owing to the smaller radius and larger divergence angle of that device. Therefore, the magnitude of the achiev-able fluorescence intensity will not be the limiting factor in the successful application of this technique to total Fe analysis. The slope of the calibration curve shown for the quartz-hematite mixtures varies from around 50-counts/sec/% near 100 wt %
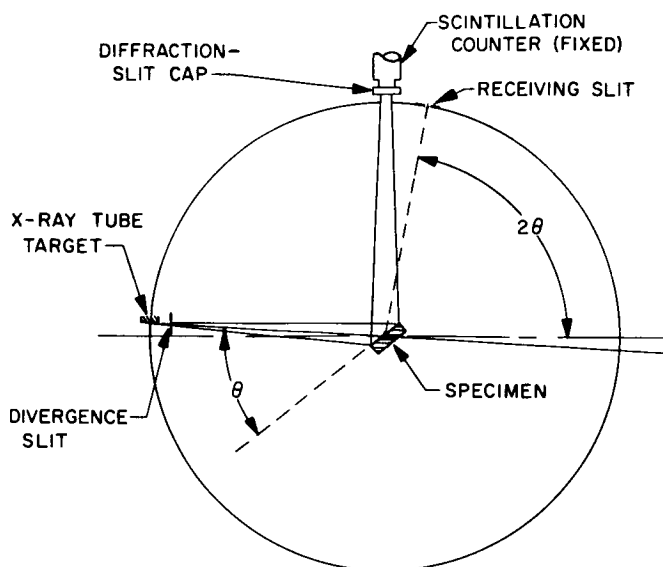
Fig. 1. Diagram of the apparatus
used in total Fe fluorescence
analysis
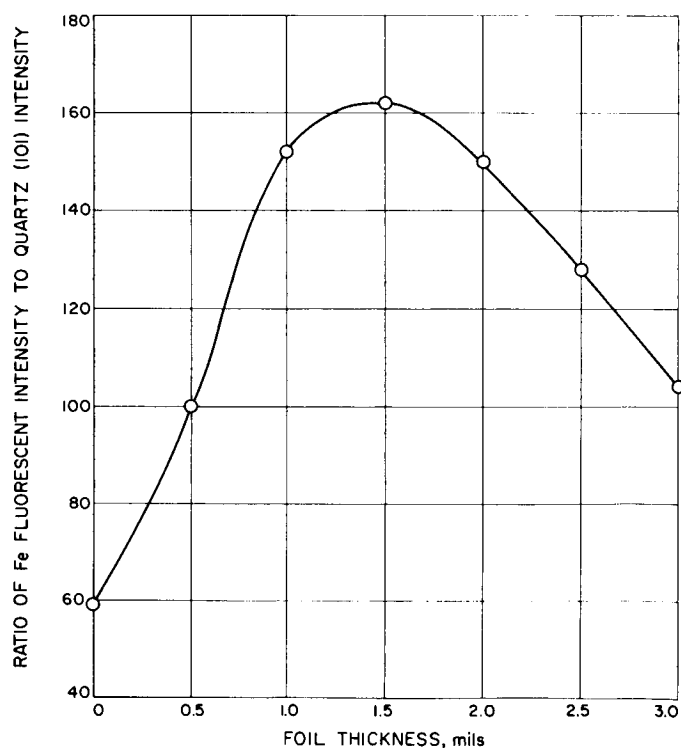
Fig. 2. Variation of the ratio
I_{Fe2O3}/I_{quartz} as a function
of filter-foil thickness
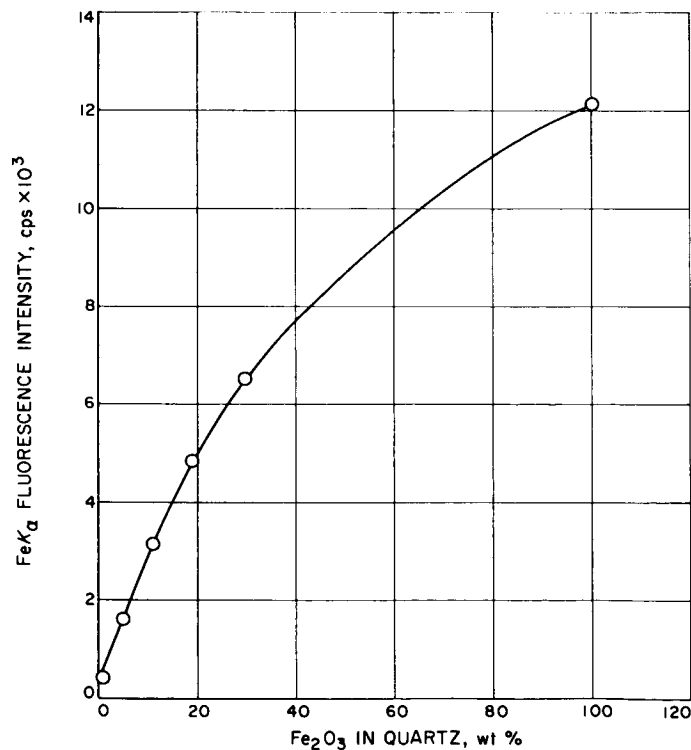
Fig. 3. Fluorescence intensity as
a function of wt % Fe_2O_3 in quartz

Fe_2O_3 to 370-counts/sec/% near zero wt % Fe_2O_3. The minimum detectable limit of Fe_2O_3 in this matrix is 7×10^{-3} wt % Fe_2O_3 for a 100-sec count accumulation time.

Although the fluorescence method outlined above has excellent sensitivity, it is subject to accuracy degradation due to matrix absorption variations. In other words, a given weight percent Fe in a highly absorbing matrix will produce a significantly lower fluorescence intensity than the same weight percent Fe in a weakly absorbing matrix. This effect is shown in Fig. 4, in which the fluorescence intensity measured using hematite-quartz mixtures and hematite-CaO mixtures is plotted against weight percent Fe. The quartz and CaO matrices were chosen because they represent extreme values of absorptivity for FeK_α for substances occurring commonly in rocks.

In order to make an approximate correction for matrix absorption, it is possible to introduce a fixed-volume fraction of a crystalline material to all specimens and to use the observed diffracted intensity as a matrix correction factor. Figure 5 shows the data given in Fig. 4 corrected by application of (200) line intensities observed from a constant-volume fraction of NaCl.

The principal difficulty with this approach is that it accounts only for the matrix absorption CuK_α and, therefore, requires a constant $\alpha_{CuK_\alpha}/\alpha_{FeK_\alpha}$ ratio for appropriate correction. The ratio of mass absorption coefficients (P) for CuK_α and FeK_α, respectively, is plotted against Z in Fig. 6. The ratio remains fairly constant for all elements shown except for Co, Fe, and Mn, which have K absorption edges between the two wavelengths. Therefore, the presence of significant quantities of any of these elements in the unknown sample will seriously affect the accuracy of the absorption correction. Iron, however, does not present a problem in this regard, since the absorption correction will be a function of the weight fraction of Fe in the sample and will, therefore, tend only to affect the slope of the corrected intensity vs weight percent calibration curve. The elements Co and Mn will, however, produce anomalously high corrected intensities. For small errors in P, it can be shown that the resultant corrected intensity relative error, dI/I, is proportional to dP/(P + 1). This means a relative error in corrected intensity of only 6% in a Cr matrix (P = 1.77).
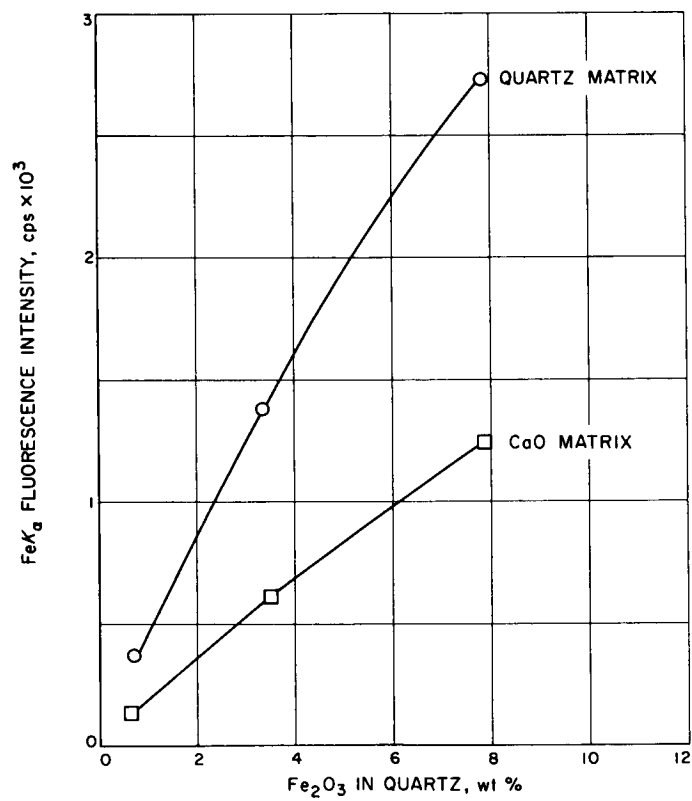
Fig. 4. Fluorescence intensity as
a function of wt % Fe_2O_3 in quartz
and CaO
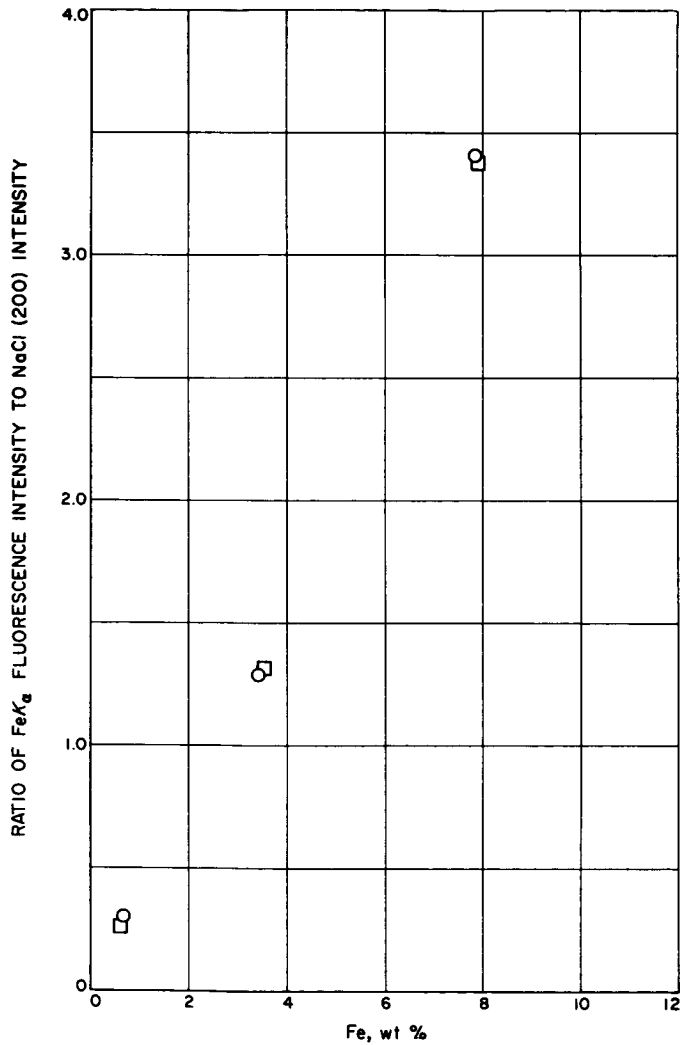
Fig. 5. Data shown in Fig. 4 correc-
ted for matrix absorption by the
application of NaCl(200)
diffraction peak
intensities
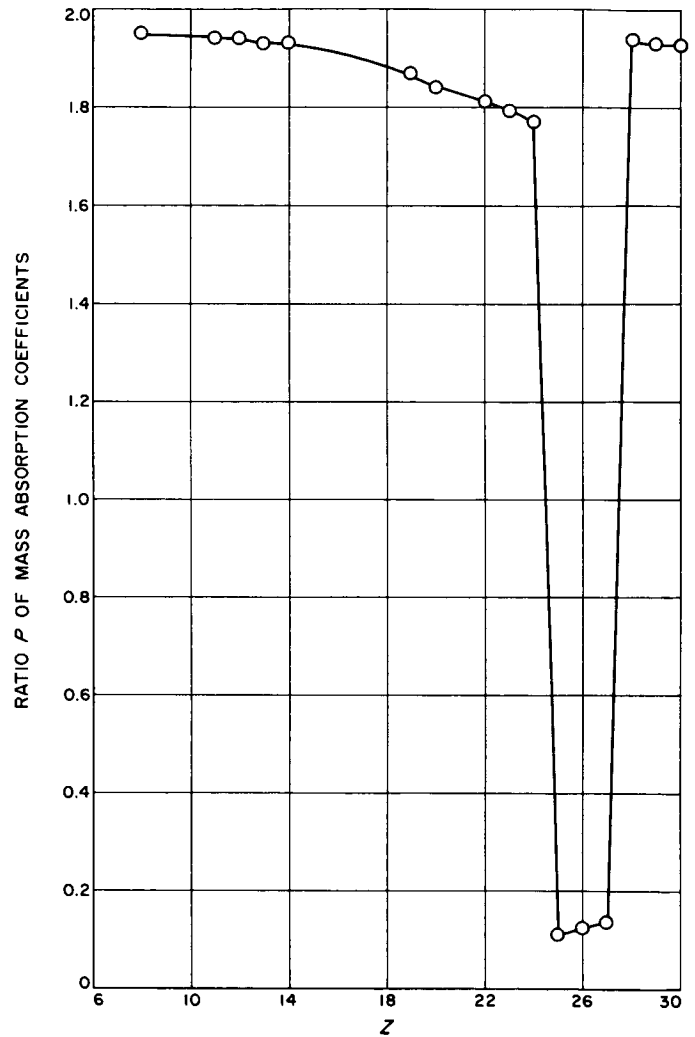
Fig. 6. The ratio of mass absorption
coefficients for CuK_α and FeK_α
$\mu/\rho(FeK_\alpha)$ $\mu/\rho(CuK_\alpha)$ as a
function of Z

An additional problem encountered in the application of this correction technique is the density uncertainty involved. The intensity of a line hkl from the ith component of a powder mixture is given by

$$I_{hkl} = \frac{AV_i}{\mu_m}$$

where A is a constant containing instrument and crystallographic parameters. The point is that the intensity is a function of the volume fraction of the ith component, which means that a knowledge of the sample density is required to add the standard as a weight fraction. Even if one adds a measured quantity (by volume or by weight) to a fixed volume of the unknown sample, the problem remains, since now a knowledge of the sample density is required to compute the dilution correction, which is a function of weight fraction. The magnitude of this error will, of course, be a function of the relative quantity of the standard required and the range over which the sample density can fluctuate. For the more common igneous rocks, the bulk density varies from 2.6 to 3.3. Using a nominal requirement of 10-wt % NaCl addition as an absorption standard, the probable maximum dilution-correction error (estimate of NaCl weight fraction) becomes ±1-wt % NaCl, which leads to a dilution correction error of only ±1% of the amount present. This error can, however, become large in the case of certain meteorites.

The final problem in the application of this technique is related to the nature of the crystalline material employed as the standard. Two important properties make NaCl attractive as a standard. In the first place, it has some strong reflections. In the second place, it is readily soluble and, therefore, easily removed from the samples to which it is added; this attribute is significant in laboratory work. However, NaCl does present difficulties in terms of peak-intensity reproducibility and relative peak amplitudes in different matrices. These problems are presently under investigation.

Another approach to the matrix correction problem is that of the internal fluorescence standard. In this case, the density uncertainty would be resolved, since the observed standard intensity would be a factor of weight fraction rather than volume fraction. Hence, an unspecified quantity of a weighed sample-standard mixture can be examined without ambiguity. The selection of the appropriate internal standard is, however, specific to the desired element, which is not true in the case

of a diffraction standard. Hence, while Co is appropriate for Fe analysis, it would not be so for Al, due to the presence of a number of absorption edges between Co and AlK_α. In addition, the method is subject to an ambiguity in the presence of significant quantities of Mn in the matrix, because Mn which has an absorption edge between Co and FeK_α. Therefore, for a truly accurate Fe fluorescence analysis in the presence of Mn, one must measure Mn fluorescence intensity in order to make a second-order absorption correction as well as measuring the fluorescence intensity of the Co internal standard. Finally, it is evident that the sample must be cobalt-free.

In terms of absorption correction, then, both the fluorescence and diffraction internal standard schemes require either the absence of, or an analysis for, Mn and Co in the matrix. The fluorescence internal standard technique avoids certain of the difficulties (ρ uncertainty, line-intensity variation) characteristic of the diffraction internal standard.

A third general absorption correction method is available--i.e., the estimation of a matrix absorption correction factor on the basis of the phase assemblage as determined by diffraction. Here, the principal uncertainties consist of the phase compositions, which in some cases cannot be determined (Na:Ca ratios in plagioclase feldspars, for example), the presence of moderate amounts of glass in the specimen, and the accuracy with which the relative abundance of the phases can be determined.

Uncorrected Fe fluorescence intensities obtained on a series of igneous rock specimens provided by D. Nash are presented in Fig. 7. These rocks represent a small portion of Nash's collection of 96 analyzed specimens which will provide material for the testing of the analytical techniques outlined here.
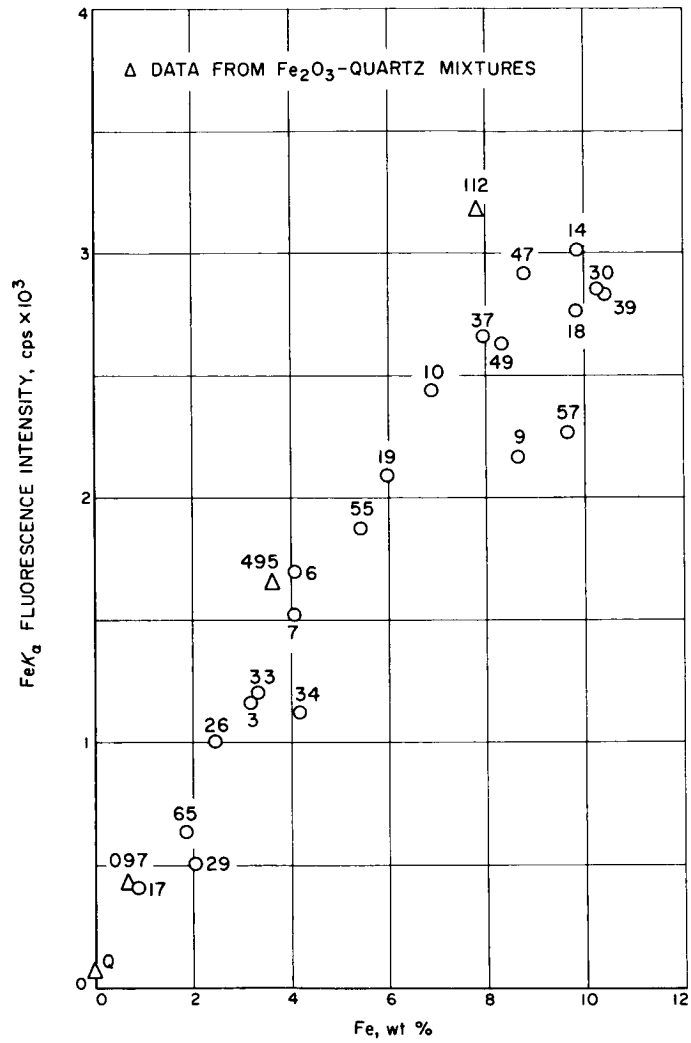
Fig. 7. Fluorescence intensity as
a function of wt % Fe for some
natural rock samples

V. X-RAY MINERALOGY AND PETROLOGY

A. SOME ASPECTS OF QUANTITATIVE ANALYSIS OF ROCKS BY X-RAY DIFFRACTION

Robert C. Speed

N65-34966

1. Introduction

A part of our studies in diffractometry is devoted to assessing the degree to which the nature of rocks can be ascertained by X-ray diffraction and how the capability of rock analysis varies with instrument and specimen variables. This paper summarizes some general relations in rock analysis by X-ray diffraction.

Rocks are generally assemblages of several crystalline phases, each of which has a characteristic diffraction pattern that is easily distinguished from patterns of other rock-forming minerals. Rocks formed by the quenching of melts are composed of glass of composition equivalent to a crystalline assemblage or they are composed of a mixture of both crystals and glass. Glass produces a broad X-ray maximum, the angular position of which is a function of composition. Rock diffraction patterns are a superposition of the individual phase patterns.

The fundamental petrologic data from which the origin of a rock may be interpreted are the composition, relative abundance, ordering, and geometry of phases in the assemblage. The geometric relations cannot be determined by X-ray diffraction. The ability of the method to provide the other data depends on three chief factors: instrumental and operational parameters, specimen preparation, and mineral assemblage.

1. Instrumental and operational parameters. The quality of diffraction data is judged by conventional terms--resolution (or line width), peak intensity, and signal/noise ratio. These functions are governed by many variables, among which are: radiation wavelength, source geometry and intensity, monochromaticity of radiation, collimation in vertical and horizontal planes, sample absorption, sample curvature relative to focus-circle curvature, divergence angle, receiving-slit width, Bragg angle, detector efficiency, dead time, pulse-amplitude discrimination, scan rate, stability of power supplies, electronics, and others.

2. Specimen preparation. The quality and reproducibility of diffraction data are strongly dependent on the way the specimen has been prepared. The variables are: particle-size distribution,

contamination, fractionation, surface geometry, porosity, thickness, and preferred orientation.

3. Mineral assemblage. Natural phases present a wide range in difficulty of identification in the presence of other phases. The variables are: line intensities, line positions, diffuse scattering and fluorescence, and mass absorption coefficient for each phase relative to values of these factors for the matrix (i.e., other minerals in the rock). Furthermore, the degree and number of allowable chemical substitutions and ordering states in a phase affect the ability to make full descriptions of rocks by X-ray diffraction alone.

The following sections consider rock analysis with assumed conditions of high X-ray flux and electronic stability, and optimum specimen preparation.

2. Minimum-Detection Limit

The minimum-detection limit (MDL) of a phase in an assemblage varies with the intensities of the strongest lines and with the composition of the bulk assemblage. The MDL of a diffraction peak is given by an intensity

$$I_p - I_b = QI_b^{1/2} \tag{1}$$

where I_b is the background intensity, I_p is the total intensity at the same angle; Q is a constant expressing the confidence level and should generally be 3 so that a probability of greater than 99% exists that the counting change is not simply random background variation. The background consists largely of two components. The first is relatively unmodified source radiation scattered from the specimen and optical elements. This background component cannot be removed by pulse-height analysis. A copper source is employed in the Mark 1 lunar prototype; the scattered background is about 50 cps at $2\theta > 25$ deg, but increases at lower angles.

The second component is fluorescent radiation generated in the specimen. With incident CuK_α radiation, the fluorescent background is chiefly proportional to the Fe content of the specimen. This is because Fe is near the CuK absorption edge, and it is the only principal constituent of rocks that is a high absorber of CuK_α. The MDL for iron-free minerals is related simply to the Fe content and the pulse-amplitude resolution for the detector employed. The FeK_α component increases the total background

by about a factor of 2 for a pure-iron specimen on the Mark 1 prototype with a detector resolution of 15% and CuK_α loss of about 10%. Other fluorescent radiation from common rocks (calcium and potassium) are effectively removed by pulse-height analysis. However, the MDL of iron-bearing minerals changes also as a function of the composition of the mineral at constant total Fe in the specimen as the peak intensity at constant mineral abundance will change through loss of CuK_α by Fe absorption.

The MDL of a phase also depends on line positions of the associated phases. If the intensity of the strongest peak of a mineral cannot be measured because of superposition of peaks from other minerals in the rock, less intense peaks that are not overlapped must be used. For a given background, detection of these peaks requires a higher abundance of the phase. It is probable that one of the three highest peaks of most minerals will be clearly delineated in most rocks. Table 1 summarizes MDL values for the three strongest peaks of common rock-forming end members in a matrix of the same mass absorption coefficient for the Mark 1 prototype with a scattered CuK_α background of 50 cps.

3. Phase Identification and Description

The approximate angular positions of intense lines in a rock diffraction pattern can generally be rapidly categorized in terms of mineral series by experienced investigators. For most igneous rocks and meteorites, these minerals are limited to olivine, pyroxene, feldspar, quartz, and iron oxides (plus free Fe and FeS in meteorites). Identification of one phase will generally limit the possibilities for the associated phases if the assemblage is in equilibrium. Nonequilibrium assemblages can frequently be detected rapidly either by the existence of strong lines from phyllosilicates, zeolites, and other hydrates at low angles or by an association of phases that cannot coexist at equilibrium.

The positions of the reflections of many of these phases vary systematically over a small angular range with compositional variation of the phase. In principle, therefore, accurate determination of the line positions for each phase by measurement relative to nearby lines of a standard can indicate the composition of the phase. Some phases which may be in major abundance, however, form solid solution series which are ternary or even more complex. Compositional determination in such cases is difficult unless each chemical substitution manifests changes in only one cell parameter while values of other parameters are constant or independent of the particular substitution. The degree of ordering or thermal state also affects line positions in some phases and, in the absence of other data, may confuse compositional

Table 1. Approximate minimum-detectable limits of common rock-forming phases in the Mark 1 prototype in matrixes of similar mass absorption coefficient α

Phase	Source	Composition	Peak intensities, wt %			Mass absorption coefficient, α
			Strongest	Second strongest	Third strongest	
Quartz	Lovelock, Nev.	SiO_2	0.5	3.6	4.2	35
Albite[a]	Amelia Courthouse, Va.	$NaAlSi_3O_8$	0.7	4.8	9	33
Anorthite[b]	Grass Valley, Calif.	$CaAl_2Si_2O_8$	2.3	3.3	13	53
Sanidine	Synthetic	$KAlSi_3O_8$	4.0	5.0	7	49
Forsterite	Synthetic	Mg_2SiO_4	3.0	3.7	4.0	32
Fayalite	Rockport, Mass.	Fe_2SiO_4	15	23	27	191
Enstatite	Bamle, Norway	$MgSiO_3$	1.7	2.9	15	33
Ferrosilite	--	$FeSiO_3$	--	--	--	153
Diopside	Synthetic	$CaMgSi_2O_6$	3.0	6	10	58
Hedenbergite[c]	Elba, Italy	$CaFeSi_2O_6$	7	16	22	--
Magnetite	Franklin, N. J.	Fe_3O_4	7	18	20	237
Iron	Synthetic	Fe	7	35	58	324
Rhyolitic glass	Glass Mt., Calif.	--	16	--	--	49[d]
Basaltic glass	Little Lake, Calif.	--	24	--	--	72[d]

[a] Actual specimen composition An_1

[b] Actual specimen composition An_{93}

[c] Actual specimen composition $Ca_{47}Fe_{47}Mg_6$

[d] Values from Tatlock (Ref. 1)

analysis. The degree of ordering in one phase may be suggested, however, by the types of associated phases or by grain size in the rock. In the absence of textural data, however, the thermal state of the specimen will be difficult to determine uniquely.

The resolution and intensity of the diffractometer make up the third factor that limits compositional determination by X-ray diffraction. These two instrument variables, respectively, control the geometrical and statistical precision with which a particular point on the line profile can be determined and, hence, the uncertainty of a binary composition as a function of phase abundance. The point to be considered in rock analysis should be the peak maximum because of abundant overlaps of diffraction lines in rock patterns. Other geometric factors and misalignments can be neglected if a standard with reflections of known positions near those of the specimen in question is employed as a reference.

For a symmetrical diffraction peak with linear limbs in the upper half of the profile,

$$\frac{d\theta}{dI} = \frac{\theta_{1/2}}{I_p - I_b} \tag{2}$$

and

$$dI = \epsilon_I = 2Q\left(I_p + I_b\right)^{1/2} \tag{3}$$

where

$\quad I_p$ = total peak intensity

$\quad I_b$ = background intensity

$\quad \theta_{1/2}$ = angular width of diffraction peak at half height

$\quad \epsilon_\theta (= d\theta)$ = uncertainty in angular position of peak maximum

$\quad \epsilon_I$ = uncertainty in intensity at peak maximum

$\quad Q$ = probability coefficient

Therefore,

$$\epsilon_\theta = \frac{2Q\theta_{1/2}\left(I_p + I_b\right)^{1/2}}{I_p - I_b}$$

(4)

Figure 1 shows plots of ϵ_θ vs I_p as given by Eq. (4) for values of half-widths of the Mark 1 prototype and laboratory diffractometers (Table 2). Three values of the parameter I_b are used to include expected extremes of background intensities. Lower bounds for I_p in Fig. 1 are provided by the minimum detectable peak intensity (Eq. 1) so that I_p (minimum) $= I_b + QI_b^{1/2}$. In general, the statistical angular error is large for phases with peaks of low intensity and phases of low abundance and when high confidence is desired. This is best shown by comparison of ϵ_θ values of Fig. 1 with values of $\Delta 2\theta$ for certain lines which shift progressively with binary chemical substitutions as given in Table 3.

Table 2 shows that the statistical error decreases as the slit is widened and the intensity is increased at constant power. The effect of increasing the half-width on the angular error by increased slit width is comparatively small.

By combining the data of Fig. 1 and Table 3, and using knowledge of absolute line intensities, an estimate can be made of the uncertainty with which composition and abundance of a phase may be determined by any given line shift and peak intensity. This is illustrated in Fig. 2 for the olivine series where the olivine abundance is varied in a matrix which has a mass absorption coefficient α approximately that of an average basalt ($\alpha \approx 74$). The curves are based on line intensities of olivine end-members in 100% abundance measured on the Mark 1 diffractometer and on calculations according to Eq. (6) which is given below together with an explanation of the shapes of the curves. The curves represent a background intensity of zero. In practice, the approximate peak intensity and angular position of olivine(130) and the average background level at a nearby angular position are determined from the diffraction chart. These values allow ϵ_θ, the angular uncertainty, to be obtained from Fig. 1; ϵ_I, the uncertainty in peak intensity, is calculated from Eq. (3). Entries of the measured values of $I_p - I_b$ and deg-2θ of the diffraction line bounded by $\pm(\epsilon_I/2)$ and $\pm(\epsilon_\theta/2)$, respectively, in Fig. 2 will define a rectangle of statistical uncertainty of abundance vs composition. For example, an olivine(130) peak with average intensity of 300 cps and peak position of 31.74 deg-2θ (equivalent to forsterite$_{80}$-fayalite$_{20}$) in a basalt matrix would have uncertainties of 30% in abundance, -10 mol % in composition,
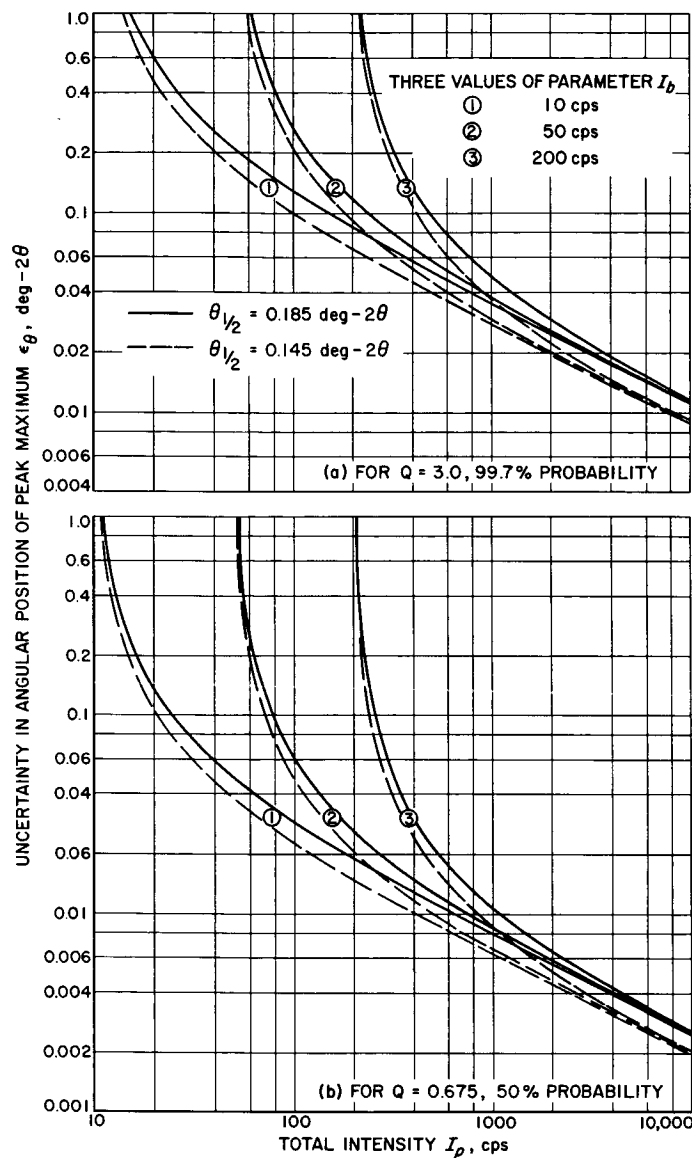
Fig. 1. Statistical angular uncertainty vs total intensity for angular width of peak at half height and background intensity

Fig. 2. Intensity of (130) reflection of olivine vs olivine composition and peak position of (130) for various olivine abundances in a basaltic matrix (α = 74)
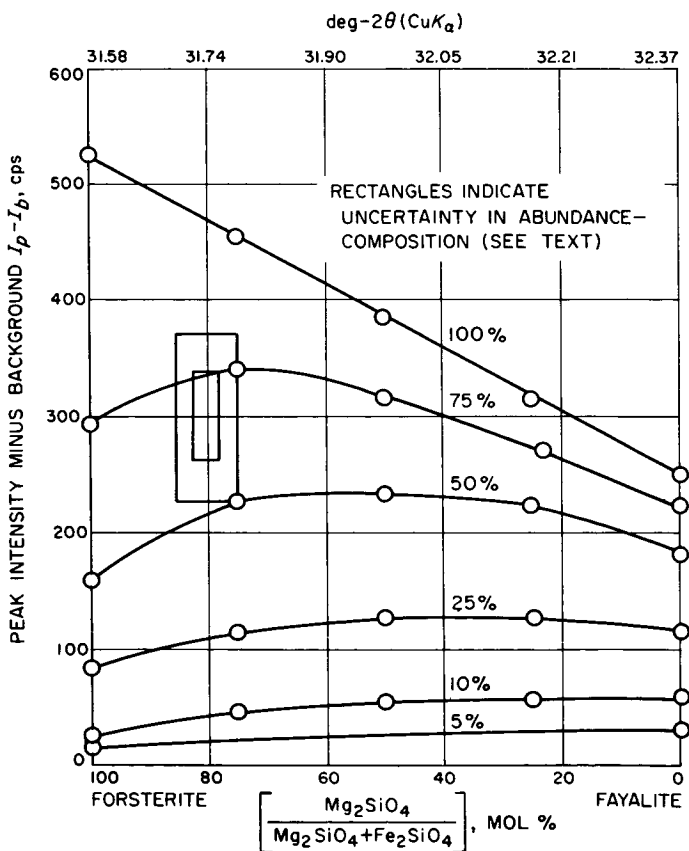
Table 2. Optical and performance data for Mark 1 and standard diffractometers, showing relation of peak intensity and receiving-slit width

Instrument	Linear-slit width, in.	Specimen-to-slit distance, cm	Angular-slit width, deg-2θ	Peak half-width $\theta_{1/2}$, deg-2θ	Peak intensity I_p, cps	X-ray tube voltage, kV	Anode current, ma
Mark 1	0.006	8.5	0.100	0.185	4300	25	1
Standard	0.006	17.0	0.050	0.0155	4350	38	18
Standard	0.006	17.0	0.050	0.0155	3340	34	16
Standard	0.006	17.0	0.050	0.0155	2350	30	14
Standard	0.003	17.0	0.025	0.145	2400	38	18
Standard	0.003	17.0	0.025	0.145	1800	34	16
Standard	0.003	17.0	0.025	0.145	1260	30	14

Table 3. Line shifts in some binary systems

Phase	Solution	Line(s)	Δ deg-2θ
Plagioclase (low state)	$NaAlSi_3O_8 - CaAl_2Si_2O_8$	$(1\bar{3}1) \wedge (131)$	1.13
Olivine	$Mg_2SiO_4 - Fe_2SiO_4$	(130)	0.79
Clinopyroxene	$CaMgSi_2O_6 - CaFeSi_2O_6$	(310)	0.62
Alkali feldspar	$KAlSi_3O_8 - NaAlSi_3O_8$	$(\bar{2}01)$	1.03
Orthopyroxene	$MgSiO_3 - FeSiO_3$	(060)	1.97
Iron spinels	$Fe_3O_4 - FeCr_2O_4$	(400)	0.09
	$Fe_3O_4 - Fe_2TiO_4$	(400)	0.74
	$Fe_3O_4 - MgAl_2O_4$	(400)	1.61

for 3σ confidence as shown by the larger rectangle of Fig. 2. The smaller rectangle shows the uncertainty for the same conditions at 1σ confidence. The uncertainty rectangles, of course, are larger at lower values of I_p and/or higher values of I_b. Diagrams similar to Fig. 2 can be constructed for line shifts of any mineral in any matrix.

The angular interval over which a line moves with a chemical substitution can be simply calculated by combining the Bragg equation with the equation relating the interplanar spacing and Miller indexes. For isometric substances, the following derivative is obtained.

$$\frac{d\theta}{da_0} = \frac{2 \sin \theta \tan \theta}{\lambda \left(h^2 + k^2 + l^2 \right)^{1/2}} \tag{5}$$

Equation (5) indicates that the angular shift for unit change in cell dimension, a_0, is greatest at high angles and, of course, low index reflections. It is assumed that the derivative is linear for ideal mineral solutions (the low-state feldspars are not ideal). Zen (Ref. 2) pointed out that cell edges in such solutions should follow a cube-root law, but experimental data in the literature indicate that most line shifts are linear, or nearly so. For non-isometric phases, a similar relation is expressed by partial derivatives $(\partial 2\theta / \partial x)_{y, z, \alpha, \beta, \ldots}$ where $x, y, \cdots$ are cell parameters.

4. Mineral Abundances

The intensity of diffraction from a mineral is a function of its composition and concentration, and the certainty with which peak intensities can be related to mineral concentration depends on the precision of the intensities as controlled by instrumental and specimen-preparation factors and, also, on knowledge of the associated phases. Considering here only the latter factor, the peak intensity of a mineral in a mixture varies with the concentration of the mineral and the mass absorption coefficients of the mineral and the matrix. Relations are given by the equations

$$I_r = \frac{I_{x_i}}{I_{100}} = \frac{x_i (\alpha_i / \alpha_M)}{x_i (\alpha_i / \alpha_M) - x_i + 1} \tag{6}$$

and

$$I_z = \frac{I_M}{I_i} = \frac{a_i}{x_i(a_i - a_M) + a_M} \qquad (7)$$

as modified from Alexander and Klug (Ref. 3). I_r is the ratio of the intensity I_{x_i} of a peak of mineral i in concentration x to the intensity I_{100} of the same peak, where mineral i is in 100% concentration; a_i and a_M are the mass absorption coefficients of mineral i and the matrix, respectively; and I_z is the ratio of the intensity I_M of mineral i in a matrix of a_M to the intensity of mineral i in a matrix of a_i, where the concentration of i is the same in both matrixes. Equation (6) shows that, in mineral assemblages with similar absorption coefficients, peak heights will change linearly with concentration. Equation (7) indicates that, for a given difference in a_i and a_M, the intensity ratio I_z will depart from unity progressively with decreasing concentration of i.

These relations are well illustrated in Fig. 2. Olivine of composition Fo_{75} has an absorption coefficient equal to that of the basaltic matrix (a = 75), and the change of peak intensity with abundance is constant for this olivine composition. For Fo_{100}, $a < a_M$ and I_z is negative; for Fo_0, $a > a_M$ and I_z is positive. The opposite slopes of the derivatives of intensity vs abundance for forsterite and fayalite produce the curve shapes of Fig. 2.

Table 1 gives the mass absorption coefficients for CuK_a for end members of rock-forming mineral series. The data indicate that, for iron-free assemblages, departures from linearity are relatively small. For example, the minimum value of I_z in mixtures of the iron-free minerals of Table 1 would be that of forsterite in diopside; the minimum detectable limit of forsterite (strongest peak) in a matrix where $a_{Fo} = a_M$ (such as enstatite) is about 3% for a background of 50 cps. The value of I_z for 3%-forsterite in diopside is 0.58, and the minimum detectable limit of forsterite in diopside is about 5.2%. Forsterite peaks in a 50-50 mixture of enstatite would be more intense by a factor of about 1.4 than those of forsterite in a 50-50 mixture with diopside. It is obvious, conversely, that the peak heights of diopside will be greater in a forsterite or enstatite assemblage than in an equivalent mixture of phases with a mass absorption coefficient that is similar to that of diopside (such as anorthite).

The data of Table 1 show that iron-bearing phases will greatly affect peak heights in mixtures by their strong absorption of copper radiation, and I_z values can be as low as 0.1. Consequently, it is important to assess the total Fe content of the specimen. This can be estimated from the iron fluorescence component in the background--as measured by background intensities at several pulse-height analyzer baseline settings in relation to the Cu distribution and low-energy counter noise--or by a discrete detector.

REFERENCES

1. Tatlock, D. B., <u>Rapid Quantitative Estimates of Quartz and Total Fe in Silicate Rocks by X-Ray Diffraction</u>, Professional Paper No. 424, U. S. Department of the Interior, U. S. Geological Survey, Washington, D. C., 1961.

2. Zen, E., "Validity of 'Vegard's Law,' " <u>The American Mineralogist</u>, Vol. 41, 1956, pp. 523-527.

3. Alexander, L. and Klug, H. P., "Basic Aspects of X-Ray Absorption in Quantitative Diffraction Analysis of Powder Mixtures," <u>Analytical Chemistry</u>, Vol. 20, 1948, p. 886.

N65-34967

B. DETERMINATION OF ABUNDANCE OF GLASS IN ROCKS BY X-RAY DIFFRACTION

D. B. Nash

Diffraction patterns of natural glasses consist of a single broad rise or maximum in the background between 12 and 40 deg-2θ (for CuK_α). The 2θ position of the maximum decreases and its intensity increases with increasing SiO_2 content of the glass. Determinative curves have been produced which relate the 2θ position to SiO_2 content for glass equivalents of igneous rocks and of the plagioclase mineral series (Nash, Refs. 1 and 2). The relative concentration of glass in a glass-crystal mixture, which can also be determined by diffraction, is the subject of the following discussion.

The intensity of the glass maximum is a function of four factors: (1) the concentration of glass in the rock, (2) glass composition, (3) mass absorption coefficients of the glass a_G, and crystalline matrix a_M, and (4) instrument parameters. The weight percent x_G of glass in a rock can be obtained from a ratio of the intensity of its diffraction maximum I_x, with that of glass of the same composition at 100% abundance I_{100}, according to the equation

$$x_G = \frac{1}{1 - (a_G/a_M) + (a_G/a_M)(I_{100}/I_x)} \tag{1}$$

which is modified from calculations by Speed [Eq. (6), Section V-A of this Report]. Measurements of I_x and I_{100} are made under identical instrumental conditions. The mass absorption coefficient of natural glasses can be calculated from an estimate of the glass composition obtained from the angular position of its diffraction maximum (Refs. 1 and 2). The abundance ratios and compositions of the crystals can be estimated from line intensities and positions, and an average mass absorption coefficient can be determined for the crystalline matrix.

If the ratio of absorption coefficients in Eq. (1) is about unity, x_G simply equals the ratio I_G/I_{100}. Figure 1 presents an example of equal absorptivity in the glass and crystalline matrix, and the change of the intensity of the obsidian maximum with concentration is nearly linear. On the other hand, the greater the difference in absorption coefficients, the greater the departure from linearity.

Calibration curves can be determined experimentally for combinations of glass and crystals of various compositions. An example is given in Fig. 2 where the
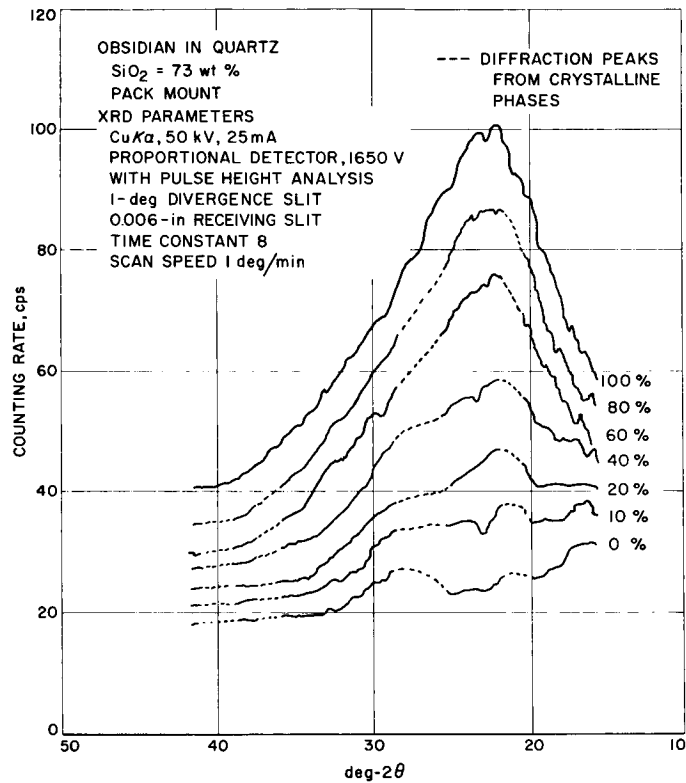
Fig. 1. Variation in intensity of glass
diffraction maximum with volume con-
centration of the glass in a glass-
crystal mixture
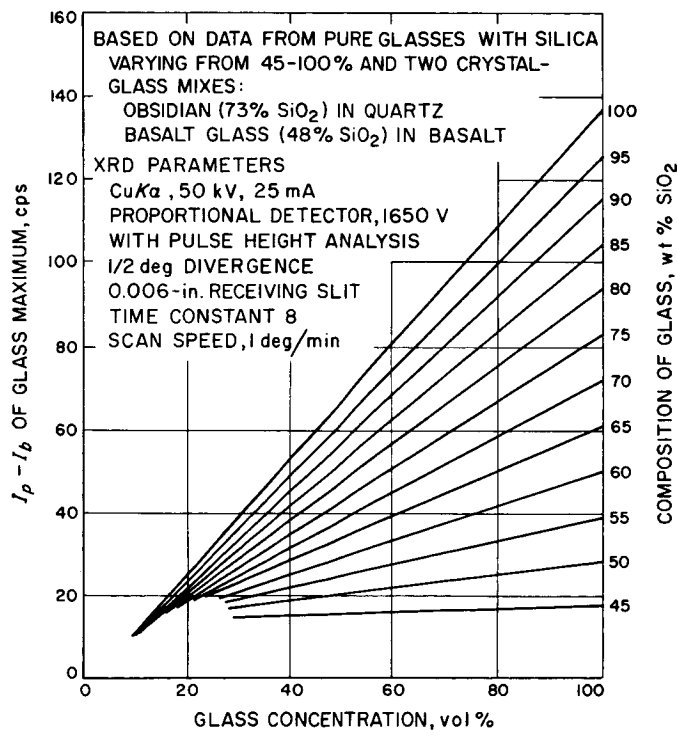
Fig. 2. Calibration curves relating
glass composition, concentration in
crystal-glass mix, and intensity of
the diffraction maximum for
glass-bearing igneous
rocks

intensity of the glass maximum and the SiO_2 composition determined from the diffraction chart allow a direct reading of the glass abundance for common calc-alkaline igneous rocks.

To use Fig. 2, one first measures the intensity $(I_p - I_b)$ of the glass maximum and its 2θ position (by intersection of straight lines through the slopes of the maximum); from another calibration curve, the 2θ position is converted to % SiO_2. Then the point of intersection of a horizontal line through the $I_p - I_b$ value and the appropriate sloping composition line yields the volume concentration of glass in the rock.

The minimum-detectable limits for a glass phase in a crystal matrix is about 15 to 30 vol % for hypocrystalline rock mixtures. Variations are a function of composition; for silicate glasses, the higher the silica concentration the stronger the diffraction maximum and, thus, the lower the minimum-detectable limit. Super-position of strong crystalline diffraction peaks upon the glass maximum make it difficult to distinguish the presence of glass in abundances less than 15 to 30 vol %. However, this is, in part, a function of the resolution of the diffractometer and may be improved by special geometries.

REFERENCES

1. Nash, D. B., "New Techniques for Quantitative SiO$_2$ Determination of Silicate Materials by X-Ray Diffraction Analysis of Glass," Advances in X-Ray Analysis, Vol. 7, Plenum Press, New York, 1963.

2. Nash, D. B., "Glass-Maximum X-Ray Diffraction Technique for Determining Silica Content of Igneous Rocks and Anorthite Content of Plagioclase Minerals," Abstract from the National Meeting (Miami, Florida, November 1964) of the Geological Society of America (New York, N. Y.).

C. STUDIES OF THE ROCK-FORMING OXIDES BY X-RAY DIFFRACTION

R. C. Speed

1. Introduction

The rock-forming oxides form a group of related minerals which occur in virtually all rocks in moderate to small quantities. This group has been largely neglected by petrologists until recent times, but current investigations indicate that the oxide group can provide valuable data on the thermodynamic conditions of rock formation (Refs. 1 and 2). It has been commonly assumed that detection and compositional determination of these minerals during bulk-rock analysis by X-ray diffraction with Cu radiation is difficult, if not impossible. This paper presents preliminary results of studies aimed at showing quantitatively the detection levels and the degree to which compositions can be determined in the oxide group by X-ray diffraction.

The oxidation state of iron in lunar specimens will be an exceedingly important indication of lunar processes. Oxidation states similar to those in most igneous rocks on Earth will indicate crystallization under oxygen fugacities (fO_2) which are largely the result of H_2O dissociation (i.e., magnetite-hematite to quartz-fayalite-magnetite fO_2 fields at magmatic temperatures). An indication of the existence of H_2O on the Moon would have considerable bearing on theories of internal lunar processes. If, however, the oxidation state is very low, the Moon may have negligible H_2O, or the $H_2(C, S, Fe)/H_2O$ ratio may be much higher on the Moon than the Earth.

2. Phase Relations

Thirteen of the fifteen phases considered here occur in the system FeO-Fe_2O_3-MgO-Al_2O_3-Cr_2O_3-TiO_2. The chemical positions and names of the important minerals in this system are illustrated in octahedral space in Fig. 1(a). The rear apex of the octahedron is occupied by TiO_2, and the only ternary subsystem on the back side of the octahedron which is abundant in rocks is FeO-Fe_2O_3-TiO_2. This subsystem is set apart in Fig. 1(b). The phases indicated in Fig. 1 can be employed as components in a complex of binary systems which are classified in Table 1.

The α spinels occur in almost all rocks; this group of minerals is outlined in Fig. 1(a) by a trigonal prism within the octahedron. Solid solution is apparently complete within this group. The titaniferous spinel, ulvospinel, is intersoluble with magnetite, but its relations with the other spinels is not certain; ulvospinel is considered here as a spinel end-member, but is not included in the prism of complete-solid solution. Experimentally determined temperatures of solvus maxima in binary

(a.) CHEMICAL POSITIONS AND NAMES
OF IMPORTANT MINERALS IN
THE SYSTEM

Cr_2O_3

CHROMITE

MAGNESIOCHROMITE

TiO_2
RUTILE

<510

FeO
WUSTITE

MgO
PERICLASE

HERCYNITE

Al_2O_3
CORUNDUM

SPINEL

860°C

MAGNETITE

MAGNESIOFERRITE

Fe_2O_3
HEMATITE

FeO

ULVOSPINEL ILMENITE $FeTi_2O_5$

TiO_2
RUTILE

$Fe_{1-x}O$
WUSTITE

600

1150

MAGNETITE

950

PSUEDOBROOKITE

(b.) LEFT LOWER REAR FACE OF
OCTAHEDRON SHOWING PHASES IN
SYSTEM $FeO-Fe_2O_3-TiO_2$

TEMPERATURES: KNOWN SOLVUS, °C
HEAVY LINES: KNOWN SOLID SOLUTIONS
OTHER THAN IN SPINEL FIELD
DASHED LINES: DEFINE SIX-COMPONENT
SPINEL FIELD OF COMPLETE SOLID
SOLUTION

Fe_2O_3
HEMATITE

Fig. 1. Natural phases in the system $FeO-Fe_2O_3-MgO-Al_2O_3-Cr_2O_3-TiO_2$

Table 1. Structural classification of binary systems in the system
$FeO\text{-}Fe_2O_3\text{-}MgO\text{-}Al_2O_3\text{-}Cr_2O_3\text{-}TiO_2$

Structural class	General formula[a]	Substituents[b]	Lattice[c] symbol
α spinel	$AX \cdot B_2X_3$	$(FeO, MgO) \cdot (Fe_2O_3, Al_2O_3, TiO_2)$	F
γ spinel	$A_{3-5}B_5X_{4-5}(S \leq 1)$	(Fe_3O_4, Fe_2O_3)	F
Rhombohedral	B_2X_3	$(Fe_2O_3, Al_2O_3, FeO \cdot TiO_2)$	R
Magnesiowustite	AX	(MgO, FeO)	F

[a]A, divalent cation; B, trivalent cation; X, oxygen

[b]Molecular substituents in general formula in parentheses

[c]F, face-centered cubic; R, rhombohedral

spinel systems are shown in Fig. 1(a). It is probable that no solvus exists in a spinel couple in which the FeO/MgO ratio changes at constant B_2X_3 composition. Natural spinels are, thus, either homogeneous solutions--stable under wide temperature variations, or preserved metastably--or a pair of coexisting exsolved phases. Compositions of natural spinels almost invariably lie within the spinel solution field; that is, end members are rare in nature. Therefore, natural spinels contain iron in two oxidation states, and the equilibrium composition of spinels at fixed-cation composition is a function of oxygen fugacity (fO_2) and temperature (T). For a given cation composition, the composition of the equilibrium spinel is a function of the minimum Gibbs free energy (ΔG) where

$$\Delta G = RT \ln fO_2 \tag{1}$$

In all these phases, the partial molar volume is small, and solid pressure has a negligible effect on the equilibrium. For any given initial spinel solution composition, a change in oxygen fugacity will require crystallization of another phase as the spinel changes composition. These associated phases will be in either the magnesiowustite (for decreasing fO_2) or rhombohedral oxide (for increasing fO_2) series of Table 1, and both series have either complete or partial solid solution where the composition is a function of fO_2 and T. It should be added that in rocks with excess SiO_2, these associated phases may form silicates (i.e., MgO, FeO, Al_2O_3).

Where two oxide series coexist (i.e., spinel + rhombohedral or spinel + magnesiowustite), two solutions to Eq. (1) will be obtained, and temperature and fO_2 can be determined uniquely. The composition of a single homogeneous spinel will indicate the temperature at or above which the spinel crystallized. The same temperature information will be obtained from an exsolved spinel pair if the compositions and relative abundances of the two phases can be determined. In the latter case, as well as one where the existence of two spinels is known and the composition of one is estimated, the temperature at which exsolution was completed will be indicated.

The γ spinels are metastable phases which form by low-temperature (300-550°C) oxidation of ferrous spinels. These phases can be considered as solutions of the rhombohedral series and the spinel series (Ref. 3).

Non-oxidized metal phases may occur in rocks which crystallize under exceedingly low values of fO_2; the meteorites and basaltic dikes that have intruded coal beds are examples. In the meteorites, the metal compositions are largely in the

system. Fe-Ni.   Two phases, α and γ, may exist; the Fe/Ni ratios of these phases are functions of temperature. Identification of both phases and determination of the composition of one phase will provide a crystallization or exsolution thermometer.

3.   X-Ray Data on Oxides

Natural rock-forming oxides are rarely pure end-members; that is, they are solutions within the compositional fields of Fig. 1 and could not be easily employed to obtain X-ray data for the oxide group. It was thus necessary to prepare synthetic oxides in order to obtain end-member X-ray data. For the oxygen-fugacity-dependent spinels, oxygen-buffered hydrothermal synthesis was employed using the buffer fugacities given by Eugster and Wones (Ref. 4). Sealed Ag tubes were used for the charge container; the solid buffer was iron-wustite. Because pure ulvospinel occurs at fO_2 values that are lower than are practically achievable in this apparatus, the spinel produced in this experiment was Usp_{83}-$Magnetite_{17}$. The ferric phases were prepared at atmospheric pressure in air. The iron-free phases were synthesized hydrothermally.

Table 2 summarizes the conditions of formation of these minerals, together with their X-ray data, which include line positions and intensities and background intensities. The X-ray data were taken with a Norelco laboratory diffractometer[1] set so that the intensity of quartz(101) was similar to that obtained with the Mark 1 lunar diffractometer. The intensity of the quartz peak was measured before and after each oxide run; oxide intensities were thus normalized to account for instrumental drifts. This correction, which amounted to 20% or less, was due chiefly to slight changes in detector voltage relative to a rather narrow PHA window. The PHA baseline was set at the pulse-amplitude minimum between Cu and Fe distributions. The loss of $CuK_α$ intensity by pulse-height analysis was less than 10%, as indicated by comparing diffraction peak intensities with and without PHA.

Replicate specimens of some minerals were run; the spinels are generally equant and show little preferred orientation. Reproducibility of the intensity of the strongest peak (311) is within 7%; some peaks are more reproducible, others less.

Background readings were taken at 25 and 50 deg-2θ with the PHA baseline set below the $FeK_α$ distribution. Line positions were measured relative to NaCl(200)

---

[1]Diffractometer parameters: $CuK_α$, 40 kV, 10 mA; 1-deg divergence; 0.006-in. slit, 2 Soller slits; time constant, 2; xenon proportional counter at 1700 V and 16% resolution; Ni filter (0.0006 in.).

Table 2. Conditions of formation and X-ray data for rock-forming oxides (plus alloys)

MDL of rock-forming oxides, wt %

Matrix, background and diffractometer	Spinel (311)	Hercynite (311)	Magnesio-chromite (311)	Chromite (311)	Magnesio-ferrite (311)	Magnetite (311)	Ulvospinel (311)	Periclase (200)	Corundum (104)	Hematite (104)	Ilmenite (104)	Pseudo-brookite (220)	a Fe (110)
1. Rhyolitic (quartz-albite-sanidine) $a = 39$													
I_b(std) = 10	1.1	1.3	0.8	1.0	0.7	0.8	0.9	0.7	2.6	0.8	1.4	1.1	0.5
I_b(M1) = 50	2.3	2.7	1.8	2.2	1.5	1.7	2.0	1.5	5.3	1.7	3.0	2.3	1.1
2. Basalt (labradorite-clinopyroxene) $Ca_{50}Mg_{25}Fe_{25}$ $a = 72$													
I_b(std) = 30	2.8	4.1	2.6	3.1	2.2	2.4	2.8	2.2	7.5	2.8	4.4	3.5	1.5
I_b(M1) = 70	4.0	6.2	3.8	4.6	3.2	3.6	4.1	3.3	10.8	4.1	6.5	5.2	2.3
3. Periodotite ($Fo_{90}En_{90}$) $a = 46$													
I_b(std) = 20	1.3	2.1	1.3	1.5	1.1	1.2	1.4	1.1	3.9	1.4	2.2	1.7	0.7
I_b(M1) = 60	2.4	3.7	2.3	2.8	1.9	2.1	2.5	2.0	6.7	2.5	4.0	3.0	1.4
4. Ferrogabbro (fayalite-hedenbergite-andesine) $a = 115$													
I_b(std) = 50	5.3	8.0	5.0	6.1	4.1	4.7	5.5	4.4	14.3	5.3	8.5	6.9	3.0
I_b(M1) = 90	7.1	11.0	6.8	8.5	5.7	6.5	7.5	6.0	19.0	7.1	11.8	9.6	4.3

Matrix components listed occur in equal quantities.

$MDL = 3I_b^{1/2}$

mixed with the oxide. Lines beyond ~70 deg-2θ are not recorded in Table 2 because this is the probable limit for lunar and planetary experiments.
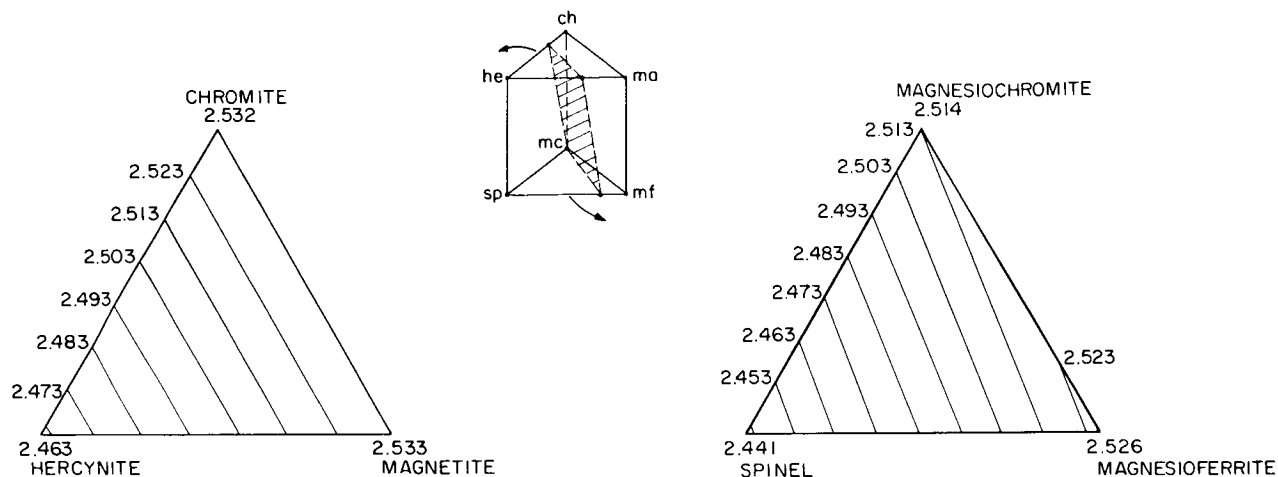
The structural classification of oxides (Table 1) is based on differences in allowable chemical substitutions and on space lattice types. Within each oxide class, all possible phases have X-ray reflections of the same indices. Because each phase in a class has a different composition, however, the cell volumes and structure factors vary continuously throughout the class. Thus, the angular position and intensity of a given reflection change as a function of composition. Experimental data indicate that these changes with composition are approximately linear (Refs. 1 and 2).

The change in cell volume, hence line position, with composition in a 7-component system (such as the spinels) is obviously not monotonic. Figure 2 shows the shift of (311), the strongest reflection, with composition in a spinel field where TiO_2 is absent. This 6-component field forms a trigonal prism (as shown in Fig. 1(a) where the end members occupy the prism apexes. Solid solution is continuous throughout this field. The top and bottom surfaces of the prism are shown with the intersection of planes of equal values of $d_{(311)}$. This reflection is chosen because it has both the lowest MDL value of spinel lines and the maximum shift with composition. Determination of $d_{(311)}$ from an X-ray diagram will then limit the composition of an unknown spinel to compositions that lie on the surface of equal $d_{(311)}$ within the prism of Fig. 2. This is equivalent to an uncertainty in composition indicated by the plane space lying between lines of equal $d_{(311)}$ on the two triangles of Fig. 2. There is an infinite number of lines lying between the bounding values, positioned as a function of the ratio of FeO/MgO in the spinel. It is thus clear that at least two other variables must be employed for a unique solution of composition in this system.

Compositions in the binary system, magnetite-ulvospinel, however, can be determined uniquely if contents of Mg, Al, and Cr are small. Spacings in this series are at higher values than those of equivalent reflections in the 6-component system discussed above. Analyses of natural ulvospinel-magnetite solid solutions indicate that this oxide series is low in MgO, Al_2O_3, and Cr_2O_3 (Ref. 1).

Figure 3 shows line shifts in the rhombohedral series of oxides. The intersolubility of ilmenite and corundum is unknown. Therefore, the size of the field of allowable compositions within the triangle and, hence, the range of compositions which have the same interplanar spacing, are unknown.

Table 3 presents minimum detectable limits for the strongest reflection of each of the rock-forming oxides in different matrixes. The matrixes were selected

CHROMITE
2.532

2.523
2.513
2.503
2.493
2.483
2.473
2.463
HERCYNITE

2.533
MAGNETITE

ch
he   ma
mc
sp   mf

MAGNESIOCHROMITE
2.514

2.513
2.503
2.493
2.483
2.473
2.463
2.453
2.441
SPINEL

2.523
2.526
MAGNESIOFERRITE

TRIANGLES ARE TOP (LEFT) AND BOTTOM (RIGHT) OF TRIANGULAR PRISM (CENTER)
DEFINING SPINEL SYSTEM
EACH VALUE OF $d_{(311)}$ DEFINES A SURFACE WITHIN THE PRISM
LINES ON TRIANGLES INDICATE INTERSECTIONS OF SURFACES WITH TOP AND BOTTOM OF PRISM

Fig. 2. Line shifts of $d_{(311)}$ (Å) in the 6-component spinel series

CORUNDUM
2.555

2.559
2.669
2.706
2.718
2.730
2.741
2.752
ILMENITE

2.706
HEMATITE
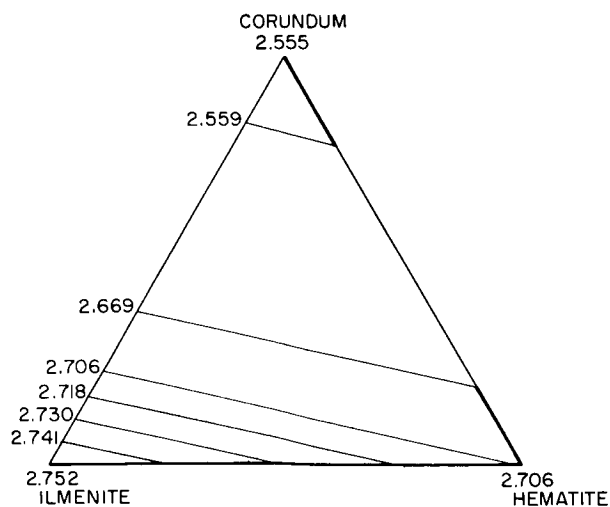
KNOWN SOLID SOLUTION INDICATED BY HEAVY LINES
INTERSOLUBILITY OF CORUNDUM AND ILMENITE UNKNOWN

Fig. 3. Line shifts of $d_{(104)}$ (Å) in
the rhombohedral oxides

lunar (M1) diffractometers

d, Å	(hkl)	I_{p-b}, cps	d, Å	(hkl)	I_{p-b}, cps	d, Å	(hkl)	I_{p-b}, cps	d, Å	(hkl)	I_{p-b}, cps	d, Å
2.020	(422)	151	1.6498	(511)	651	1.5575	(440)	755	1.429			
2.041	(422)	62	1.665	(511)	120	1.570	(440)	150	1.443			
2.083	(422)	17	1.700	(333)	176	1.604	(440)	258	1.473			
2.095	(422)	27	1.713	(333)	92	1.614	(440)	107				
2.095	(422)	60	1.7095	(511)	150	1.612	(440)	200				
2.105	(422)	18			121		(440)	148				
2.134	(422)	34	1.742	(333)	97	1.642	(440)	133	1.508			
1.742	(116)	458	1.602	(018)	37	1.512	(214)	177	1.406	(300)	272	1.375
1.844	(116)	150	1.696	(018)	32	1.600	(214)	88	--	(300)	94	--
1.869	(116)	127	1.727	(018)	25	1.635	(214)	59	1.506	(300)	48	1.470
2.405	(321)	42	1.914	(331)	66	1.969	(002)	65	0.861	(232)	55	--

2

x-forming oxides in four matrixes for approximate background levels of laboratory (std) and

Reflection (hkl)	Intensity I_{p-b}, cps	Interplanar spacing d, Å	(hkl)	I_{p-b}, cps	d, Å	(hkl)	I_{p-b}, cps	d, Å	(hkl)	I_{p-b}, cps	d, Å	K_α	(hkl) K_{α_1}	I_{p-b}, cps
(111)	470	4.67	(220)	552	2.860	(311)	1730	2.441	(222)	37	2.334		(400)	1405
(111)	--		(220)	270	2.885	(311)	423	2.463					(400)	67
(111)	446	4.82	(220)	77	2.950	(311)	560	2.514					(400)	305
(111)	49		(220)	118	2.470	(311)	308	2.532					(400)	53
(111)	27		(220)	190	2.962	(311)	510	2.526					(400)	113
(111)	27		(220)	122	2.971	(311)	334	2.533	(222)	20	2.424		(400)	83
(111)	36		(220)	124	3.010	(311)	336	2.576	(222)	23	2.465		(400)	69
(111)	154	2.434	(200)	2095	2.106	(220)	930	1.4885						
(111)	--	2.486	(200)	--	2.153	(220)	--	1.523						
(012)	416	3.482	(104)	595	2.555	(110)	245	2.382	(113)	613	2.089		(024)	256
(012)	113	3.690	(104)	322	2.706	(110)	242	2.522	(113)	75	2.210		(024)	116
(012)	82	3.747	(104)	247	2.752	(110)	131	2.545	(113)	49	2.240		(024)	70
(200)	109	4.89	(220)	303	3.485	(230)	225	2.750	(301)	61	2.455		(131)	63
(110)	240	2.026	(200)	29	1.434									
(111)	2880	2.036	(200)	1102	1.764									

2

Table 3. Minimum detectable limits of roc

Phase	Composition	Space group	Temp, °C	Conditions of formation		Duration, days	Mass absorption coefficient		Background		Fe, Atomic %
				Log fO_2, bars	Pressure P_t, bars		$^a CuK_\alpha$	$^a FeK_\alpha$	25 deg-2θ, cps	50 deg-2θ, cps	
Spinel group											
Spinel	$MgAl_2O_4$	Fd3m	a				25.5	49.3	6	6	0
Hercynite	$FeAl_2O_4$	Fd3m	800	-18.8	1000	2	69.73	49.50	190	198	14.3
Magnesiochromite	$MgCr_2O_4$	Fd3m	1000	--	1000	2	84.9	155.0	80	80	0
Chromite	$FeCr_2O_4$	Fd3m	800	-18.8	1000	2	129.2	155.2	115	122	14.3
Magnesioferrite	$MgFe_2O_4$	Fd3m	1000	atm	atm	16	112.0	44.7	285	290	28.6
Magnetite	$FeFe_2O_4$	Fd3m	b				156.3	44.9	285	295	42.9
Ulvospinel	Fe_2TiO_4[e]	Fd3m	800	-18.8	1000	2	133.6	81.2	163	173	28.6[a]
Magnesiowustite group											
Periclase	MgO	Fm3m	1000	atm	atm	2	25.5	43.3	7	7	0
Wustite	FeO	Fm3m	d				180.5	48.8	--	--	50.0
Rhombohedral group											
Corundum	Al_2O_3	R$\bar{3}$ c	1000	atm	atm	2	25.4	49.8	27	12	0
Hematite	Fe_2O_3	R$\bar{3}$ c	1000	atm	atm	2	146.6	44.0	315	317	40.0
Ilmenite	$FeTiO_3$	R3	b				114.6	94.2	88	100	20.0
Other											
Psuedobrookite	Fe_2TiO_5	Bbmm	1000	atm	atm	4	118.1	244.7	190	185	25.0
Alloys											
α Fe (Ni)	--	Im3m	c	--	--	--	350.0	76.0	235	265	100(-94)
γ Ni (Fe)	--	Fm3m	c				48.0	94.0	152	165	0(-94)

[a]National Bureau of Standards, synthetic

[b]Tem-Press, Inc., synthetic

[c]Baker's Analyzed Reagent (unheated)

[d]Not synthesized; data from ASTM (8-11% Fe_2O_3)

[e]Non-stoichiometric composition (83% Fe_2TiO_4; 17% $FeFe_2O_4$)

to represent both the most common rocks and the extremes of likely mass absorption coefficients. The absorption added by the minimum detectable amount of the oxide is not included in the matrix absorption coefficient and would raise the matrix coefficient by 3% or less. The values of MDL depend on the intensity of the reflection and on the difference in mass absorption coefficients of the mineral in question and the matrix. The intensity at the MDL is equal to $3I_b^{1/2}$ where I_b is the background intensity which, of course, varies with each matrix. Equations (1) and (4) in Section V-A give the numerical relations used in these calculated MDL values.

Table 4 gives the average normative weight percent contents of pure magnetite and ilmenite in common igneous rocks (data taken from Nockolds, Ref. 5) for comparison to MDL values of oxides in Table 3. The normative amounts of these minerals, however, do not represent the actual amounts of the rock-forming oxides in these rocks because in norm calculations all TiO_2 in the chemical analysis is assigned as ilmenite and all Fe_2O_3 as magnetite. Much of the TiO_2 is actually in the spinel phase, and MgO and Al_2O_3, which are frequently abundant in natural spinels, are assigned to the silicates. Thus, in most cases, the actual abundance of oxides is greater than normative abundance. Exceptions occur in alkaline rocks where TiO_2 exists in silicates and also occur in highly oxidized rocks where Fe_2O_3 is abundant in silicates; in both these rock types, however, oxide contents are generally greater than in calc-alkaline or unoxidized equivalents.

4. Conclusions

Following are some preliminary conclusions on the capability of analyzing rock-forming oxides by X-ray diffraction.

First, the average abundance of oxides in common rocks is considerably higher than the minimum-detectable limits of oxides for these rocks as given in Table 3. The existence of an oxide series in a rock should thus be determinable by X-ray diffraction. Where an originally homogeneous oxide has exsolved into coexisting phases with discrete reflections, detection of either phase may be marginal in some rocks. Superposition of silicate reflections on the few strong lines of the oxides will impair identification.

Second, determination of line spacings of spinels in rock powders allows a broad categorization of compositions by increasing d values (Fig. 2) as follows:

1. $MgAl_2O_4$ (spinel proper)
2. Aluminous spinel series

Table 4. Normative wt % magnetite and ilmenite contents of common rocks

Rock type	Magnetite,[a] wt %	Ilmenite,[a] wt %
Average calc-alkaline rhyolite	1.9	0.5
Average alkaline rhyolite	1.9	0.3
Average dacite	3.3	1.2
Average tonalite	2.1	1.2
Average andesite	5.1	2.4
Average diorite	3.9	2.9
Thoeleite	4.2	3.8
Alkaline basalt	4.6	5.0
Average pyroxenite	3.5	1.1
Dunite	2.8	0.5
Average peridotite	3.7	1.5

[a]Percentages from Nockolds, Ref. 5.

3. Magnetite-chromite series and magnesian equivalents

4. Titaniferous magnetites (an approximation of the ulvospinel-magnetite ratio is possible here)

The peak intensities of phases in (3) and (4) are rather similar, and the intensities can roughly indicate the abundance of a phase in those categories. Further, the abundance of spinel proper ($MgAl_2O_4$) can be determined, but the aluminous spinel field has large changes of peak intensity with composition, and abundances cannot be estimated here.

If the spinel abundance is estimated, it is possible to use other parameters to delineate further the spinel composition. Bulk rock magnetic susceptibility and/or FeK_α background intensity could be employed. Use of either assumes that the Fe content of the other rock-forming phases is small. The compositions of the silicates should be known for appropriate FeK_α absorption corrections when the background intensity is used.

Third, in the laboratory, the oxides can generally be easily separated from the rock by virtue of their high density or magnetic susceptibility. Uncertainties in the abundance and matrix absorption are thus eliminated. It appears that unique compositions can be determined in each oxide series by the combination of line position, absolute intensities, and FeK_α background for oxide separates.

REFERENCES

1. Buddington, A., and Lindsley, D. H., "Iron-Titanium Oxide Minerals," *Journal of Petrology*, Vol. 5, 1964, pp. 310-357.

2. Turnock, A. C., and Eugster, H. P., "Fe-Al Oxides: Phase Relationships Below 1000° C," *Journal of Petrology*, Vol. 3, 1962, pp. 533-566.

3. Akimoto, S., Katsura, T., and Yoshida, M., "Magnetic Properties of $TiFe_2O_4$-Fe_3O_4 System and Their Change with Oxidation," *Journal of Geomagnetism and Geoelectricity*, Vol. 9, 1957, pp. 165-178.

4. Eugster, H. P., and Wones, D. R., "Stability Relations of the Ferruginous Biotite, Annite," *Journal of Petrology*, Vol. 3, 1962, pp. 82-125.

5. Nockolds, S. R., "Average Chemical Compositions of Some Igneous Rocks," *Bulletin of the Geological Society of America*, Vol. 65, 1954, pp. 1007-1032.

D.   THE MINIMUM DETECTABLE LIMIT OF HEMATITE IN QUARTZ BY DIFFRACTION AND FLUORESCENCE

J. A. Dunne

In the course of the experimental work described in Section IV-C of this Report, a comparison was made between diffraction and fluorescence techniques for the determination of the quantity of the iron-bearing fraction in a two-phase mix. The selected mixture was hematite (Fe_2O_3) and quartz. Figure 1 shows diffraction traces of the hematite(104) peak for 0.97, 0.46, 0.18 and 0.3 wt % hematite. Fixed-time data indicate a 100-sec accumulation time minimum-detectable limit of 0.03 wt % hematite in quartz using the (104) peak. This is approximately four times the MDL computed for the non-dispersive fluorescence analyzer described in Section IV-C. In a scanning mode, the data shown in Fig. 1 indicate an MDL around 0.1 wt % Fe_2O_3. The relative contrast obtained by the two techniques is shown in Fig. 2. The background intensity, shown for comparison, was obtained without using pulse-amplitude discrimination against the Fe fluorescence radiation. This does not, however, affect the MDL obtained by diffraction, since the background increment due to fluorescence is negligible at this level, as is evident in the data.

It has been demonstrated, then, that where iron exists in a single phase, that phase can be determined with the best sensitivity by use of the fluorescence technique. For mixtures containing more than one iron-bearing phase, however, the MDL for each phase will obviously be that obtainable by diffraction.
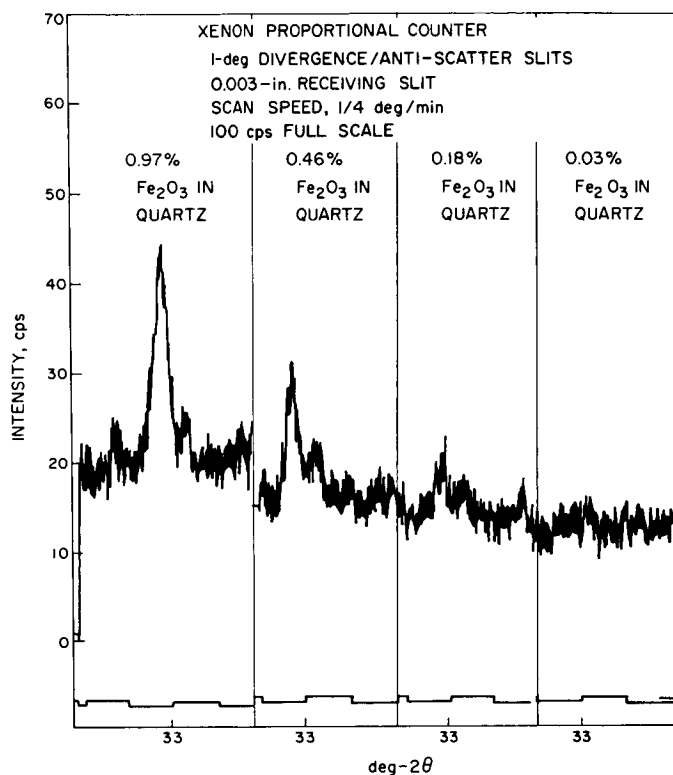
Fig. 1. Diffractometer scans of the hematite(104) peak for samples with 0.97, 0.46, 0.18, and 0.03 wt % Fe_2O_3 in quartz
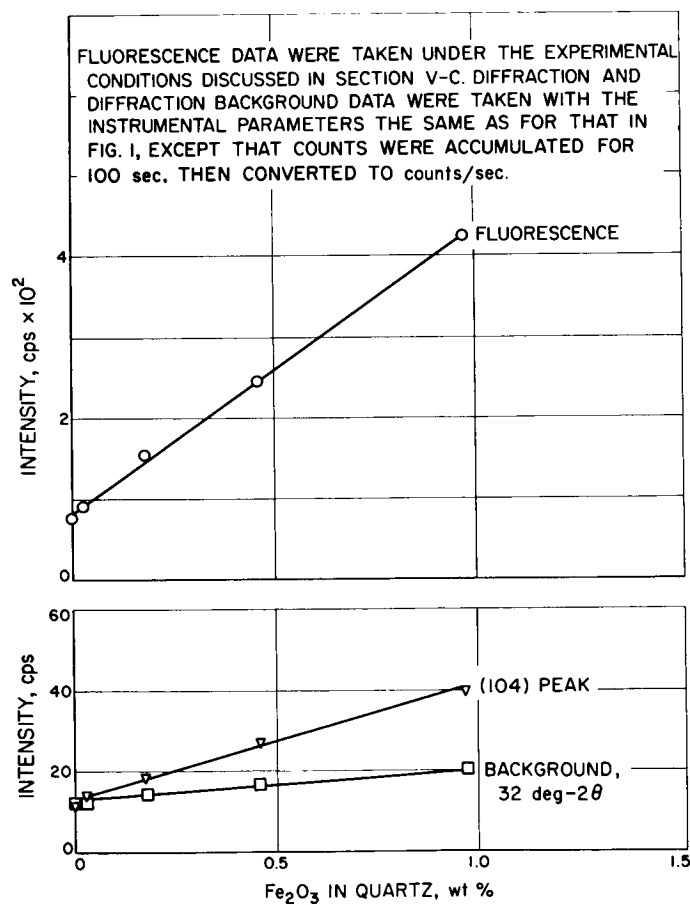
Fig. 2. Comparison of fluorescence, diffraction, and diffraction-background data taken on Fe_2O_3-quartz mixtures

E. X-RAY DIFFRACTION ANALYSIS OF RADIATION DAMAGED ROCKS

D. B. Nash

1. Introduction

Because the Moon's surface is exposed to solar corpuscular radiation, lunar surface rocks may have been chemically or structurally altered by the radiation. If so, analyses of lunar rocks by X-ray diffraction may be impaired. Consequently, laboratory experiments are being conducted to determine the effects of simulated solar-wind bombardment on igneous rocks. Preliminary results are presented here.

Samples of rock powder, single crystals, and iron-oxide powder were exposed to artificial proton beams[1] of energy up to 10 keV for durations of equivalent current of up to 10^6 yr exposure to solar wind on the Moon's surface. The samples were then examined by X-ray diffraction to detect changes during irradiation. The results indicate that moderate to radical changes can occur in both chemical and mineralogical composition of the samples as a result of the irradiation; extent of the changes varies with the original composition of the material.

2. Analysis of Artificially Irradiated Samples

Seven samples were investigated; they are listed along with the conditions and duration of irradiation in Table 1. A brief description of the results of each irradiation follows.

a. Iron-oxide powder. This powder of hematite composition (Fe_2O_3) was reduced to a mixture of magnetite (Fe_3O_4) and free-iron (α Fe) by H-ion irradiation equivalent to 10^5 yr of lunar exposure to solar wind. This transformation can be represented by the reaction

$$4Fe_2O_3 + 8H^+ \rightarrow 2Fe_3O_4 + 2Fe + 5H_2O \uparrow (+ \text{ net positive charge})$$
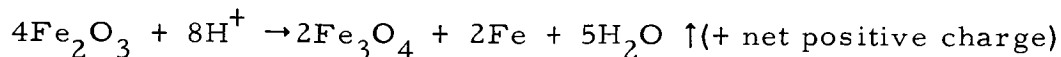
The X-ray result, of course, was a complete change in the diffraction pattern (Fig. 1) from one of the highly oxidized starting materials to one of the reduced products. Since FeK_α radiation was used for the diffraction analysis, no increase in background level resulted from concentration of the iron, as would be the case if CuK_α were the working radiation.

---

[1] Several of the sample irradiations were performed by G. K. Wehner and D. L. Rosenberg of Litton Systems, Minneapolis. Others were irradiated in the laboratory of the author at JPL.

Table 1. Summary of experimental data from simulated solar-wind exposure.

Original material	Sample configuration	Proton energy, keV	Equivalent lunar exposure age, yr	X-ray effects
Oligoclase[a]	Single crystal, cut para (001)	5	1.23×10^4	None--patterns before and after were identical.
Enstatite[a]	Single crystal, cut para (241)	5	0.88×10^4	Background increased 31%; peak/background decreased 12%.
Basalt[a] Plagioclase Clinopyroxene Magnetite	Powder, particles $<37\,\mu$	0.5	0.859×10^5	Background increased 8%; three weak augite peaks appeared near 54-58 deg-2θ.
Scoria (basaltic)[b]	Powder, particles $<20\,\mu$	0.5	10^6	Peak intensities decreased 25%; background increased slightly.
Greenstone[b] Chlorite Actinolite Epidote Plagioclase Quartz	Powder, particles $<20\,\mu$	0.5	10^5	Hydrous peaks decreased 30-50%; plag peaks decreased 50%; background increased slightly. Quartz peaks increased 100%.
Pumice[b] Rhyolite glass ($SiO_2 \sim 66\%$)	Powder, particles $<20\,\mu$	0.5	10^6	Glass "maximum" was less intense by 5% and had apparent 2θ shift of 0.5 deg-2θ.
Hematite[b] Fe_2O_3	Powder, particles $<20\,\mu$	0.5	10^5	Was complete change in pattern to that of magnetite + Fe.

[a]Irradiated by the author.

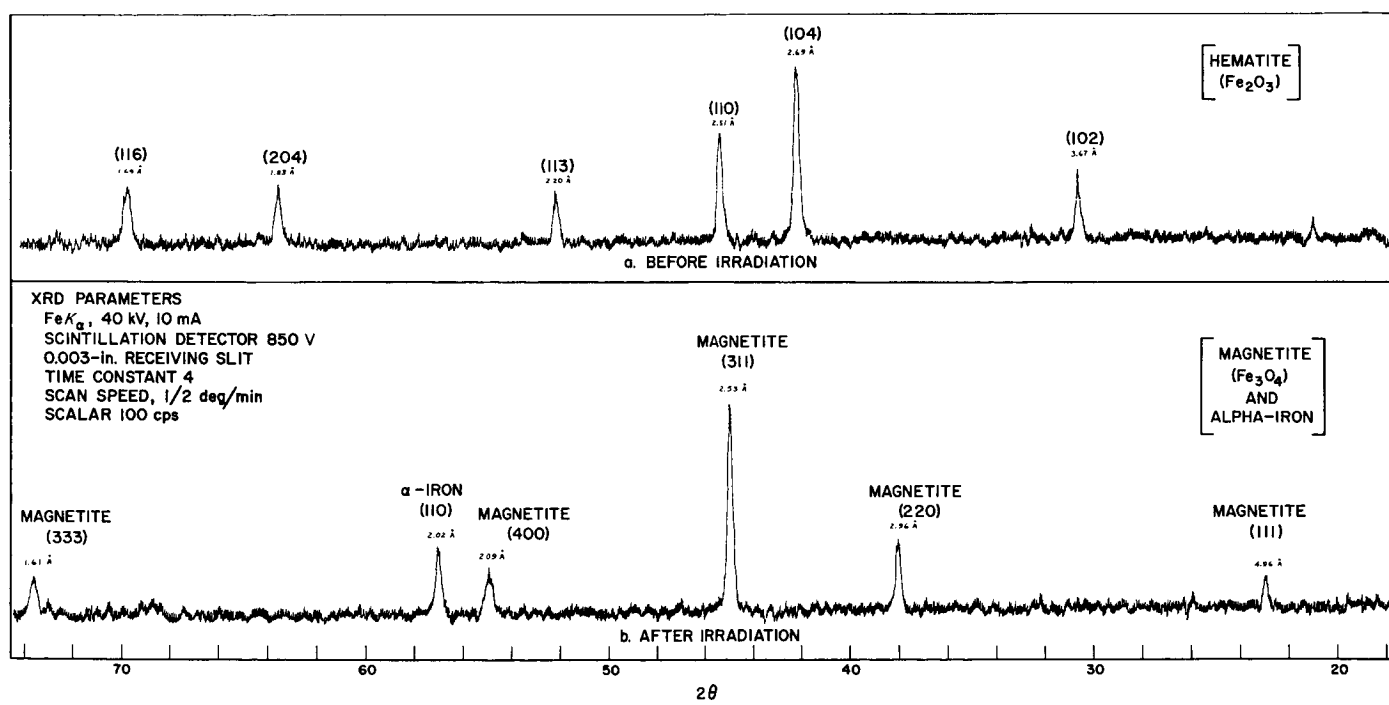[b]Irradiated by G. K. Wehner and D. L. Rosenberg of Litton Systems, Minneapolis.

Fig. 1. X-ray diffractometer patterns of original hematite and product magnetite and of α-iron after reduction by H-ion irradiation

b. Basalt powder. Two different basalt samples composed of plagioclase, clinopyroxene, and magnetite were irradiated. The first was exposed to an equivalent of 10^6 yr of 0.5 keV solar protons. No detectable change in composition or relative diffraction-peak intensity developed; however, the X-ray pattern (Fig. 2) showed an average decrease of about 25% in the absolute intensity of all diffraction peaks, but no peak broadening or angular shift. The cause of this intensity loss is uncertain; in general, an overall loss of diffraction peak intensity (assuming constant instrument parameters and sample configuration) indicates sample dilution. But dilution usually results in detection of the solvent by the presence of additional diffraction peaks or increased background level (from secondary fluorescence), neither of which occurred here.

Another powdered basalt specimen (Little Lake) was exposed to 10 keV protons for 10^5 lunar years. The only effect on the X-ray pattern was an 8% increase in background intensity due to reduction of magnetite to free-iron with consequent increase in Fe-fluorescence by the CuK working radiation. There was no loss in peak intensities, as in the other basalt sample, above, nor was there change in peak width or position. Several weak augite peaks appeared in the irradiated pattern between 54 and 58 deg-2θ; it is thought that these were "masked" in the original pattern by surface conditions of the powder which were subsequently altered during irradiation by sputter-cleaning of the surface.

c. Greenstone powder. Samples of greenstone powder, containing abundant hydrous minerals (chlorite, actinolite, epidote) and quartz and plagioclase, were differentially sputtered and, as a result, partially dehydrated; this is indicated on the X-ray patterns (Fig. 3) by a relative decrease in intensity of diffraction peaks of the hydrous phases and plagioclase, and an increase in intensity of quartz peaks. The hydrous phases and plagioclase, being structurally less stable (because of the highly altered condition of the original rock), were sputtered away more rapidly than the quartz, effectively concentrating the latter. There was no detection of new phases formed by the irradiation.

d. Pumice. This powder composed entirely of rhyolitic glass with SiO_2 content of 66 ±3 wt % (determined by the glass-diffraction technique, Ref. 2) was irradiated for an equivalent of 10^6 lunar years. Its diffraction maximum (Fig. 4) was slightly reduced in intensity and was apparently shifted to lower 2θ, suggesting a relative increase in SiO_2 to 72 ±3 wt %. Also, incident diffraction peaks of minor crystalline phases (from partial devitrification of the glass) in the original pattern

XRD PARAMETERS
CuK$_\alpha$, 40 kV, 20 mA
PROPORTIONAL DETECTOR 1650 V
I deg DIVERGENCE
0.003-in. RECEIVING SLIT
TIME CONSTANT 4
SCAN SPEED, 1/2 deg/min
SCALAR 200 cps

BEFORE

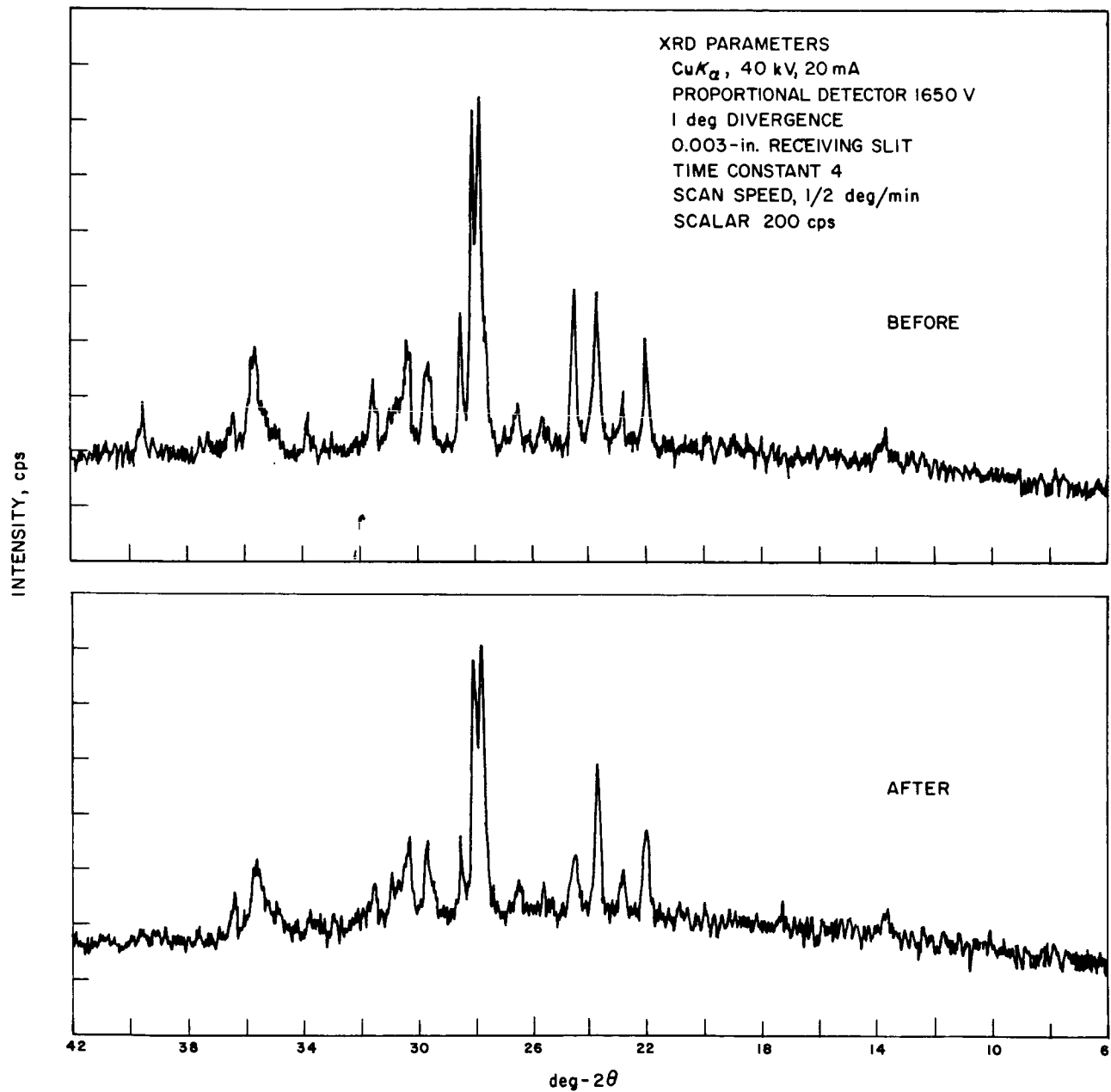AFTER

INTENSITY, cps

deg-2θ

Fig. 2. X-ray diffractometer patterns of basaltic scoria before and after H-ion irradiation equivalent to 10^6 years of lunar exposure to solar wind
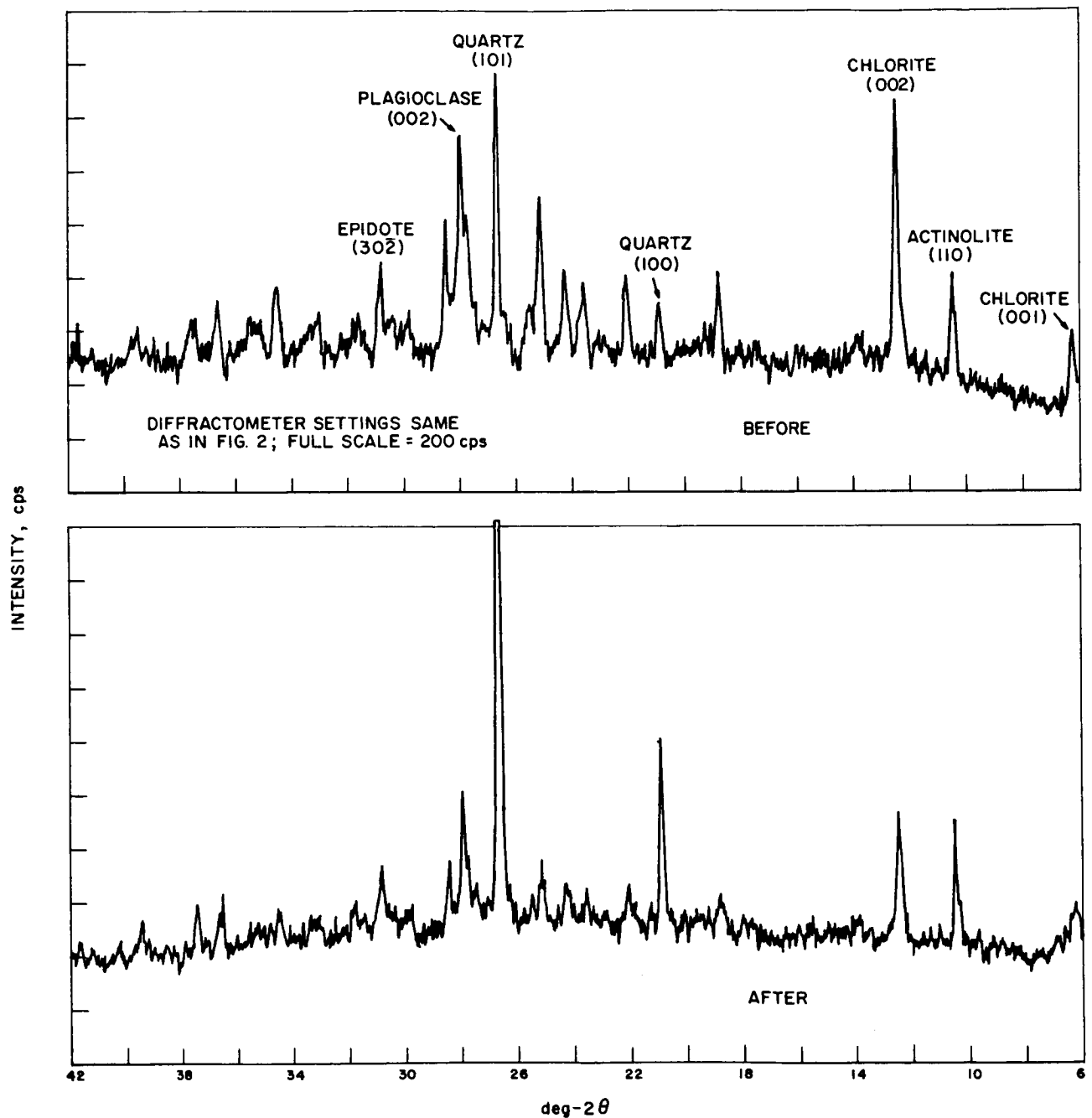
Fig. 3. X-ray diffractometer patterns of powdered greenstone (metabasalt, Ref. 1) before and after exposure to 0.5 keV H-ion irradiation equivalent to 10^5 years of exposure to solar wind
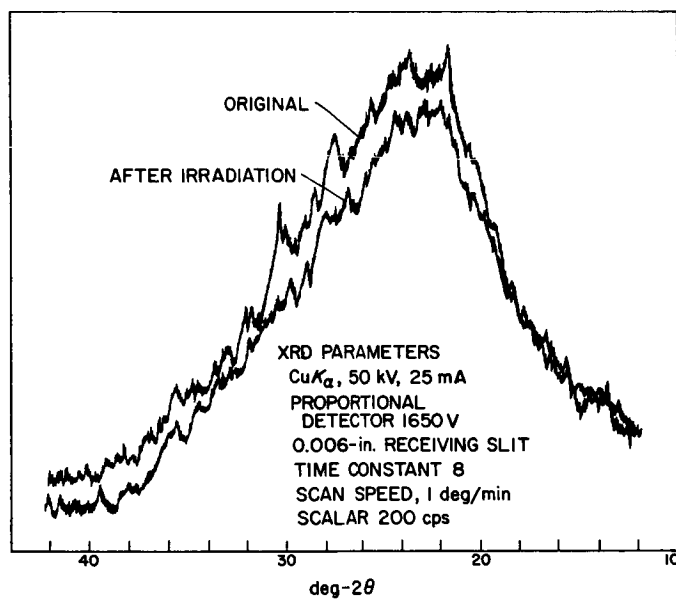
Fig. 4. X-ray diffractometer patterns
of pumice powder before and after
H-ion irradiation equivalent to
10^6 years of lunar exposure
to solar wind

are diminished in the irradiated pattern, suggesting loss or destruction of these phases by H-ion sputtering. The apparent shift in glass-diffraction maximum position could be due to dehydration and to consequent increase in SiO_2 content of the irradiated glass.

  e. Oligoclase and enstatite. Two single-crystal slabs, of oligoclase and enstatite, were exposed to 5 keV protons for the equivalent of 10^4 lunar years. The oligoclase was unaffected by the irradiation; its X-ray diffraction pattern afterward was virtually identical to the pre-exposure pattern. The enstatite was, likewise, nearly unaffected except for an increase in background level from 48 to 63 cps (31% increase) and a consequent decrease in peak/background ratio of 12%. In neither sample was there loss or gain of diffraction peaks; there were no peak shifts nor peak broadening.

3. Discussion of Results

  The foregoing examples show that X-ray diffraction data taken from rock samples may or may not be influenced by the previous irradiation history of the rock, depending on the original composition of the rock and the duration and energy of irradiation. There is no question that the diffraction method can detect changes in rocks resulting from irradiation; however, it is also clear that X-ray diffraction may not detect <u>all</u> significant effects of radiation. For example, X-ray diffraction was unable to detect the cause of strong surface darkening (Ref. 3) in three powder samples--scoria, greenstone, and pumice. Whatever the mechanism of darkening, it was outside the detection capability of the X-ray diffraction method. (Darkening of the hematite powder was clearly due to a phase change from red hematite to black magnetite and iron. The two single-crystal samples, oligoclase and enstatite were not visibly darkened.)

  The diffraction data from samples irradiated by protons for $\leq 10^6$ yr is not degraded in terms of X-ray quality (such as peak width, symmetry, etc.); these data merely reflect the chemical modifications and phase-abundance changes that are produced in the sample.

4. Implications to Lunar X-Ray Analysis

  On the assumption that the kind of radiation effects produced in this experimental study do occur on the Moon's surface, the following conclusions can be made regarding the effects of the radiation on the results to be obtained by X-ray diffraction analysis of lunar surface rocks:

First, anhydrous silicate phases (crystalline or glass) on the Moon's surface will be little affected by solar-wind exposure of one million years. The effects of longer exposure are, at present, undetermined.

Second, the experimental data suggest that hydrous silicate phases tend to be sputtered more rapidly than anhydrous and, thus, will be depleted in concentration by solar-wind effects. X-ray samples of the Moon's surface material may thus be deficient in hydrous and other soft phases relative to equivalent bedrock.

Third, iron-oxide phases in surface-exposed rock will be reduced to free-iron. Thus, diffraction patterns of surface material may have higher background level than bedrock equivalents.

Fourth, fresh bedrock will be unaffected by solar-wind radiation. Exposed bedrock (i.e., not covered by surficial debris) will be affected only to a depth of a few-hundred microns at the very most (Ref. 1). Therefore, since the XRD sampler must drill into a bedrock surface to a depth of at least 1/2 in. in order to obtain sufficient powder for an XRD sample, the relatively small damaged portion of the sample will likely be homogenized with the rest of the sample and its effects will be undetected.

Fifth, X-ray diffraction analysis of rocks affected by proton bombardment in a way similar to those in this investigation cannot prove that the rock has been irradiated. That is, there is nothing inherent in the diffraction patterns of irradiated specimens that clearly shows that radiation has produced the incurred effects. All the changes or differences detected in rocks by X-ray diffraction could be the result of processes other than sputtering or chemical reaction with a hydrogen plasma.

REFERENCES

1. Hines, R. L., "Ranges of 7.5-52 keV H_2^+, D_2^+, He^+, and Ne^+ Ions in Quartz," The Physical Review, Vol. 120, 1960, pp. 1626-1630.

2. Nash, D. B., "New Techniques for Quantitative SiO_2 Determination of Silicate Materials by X-Ray Diffraction Analysis of Glass," Advances in X-Ray Analysis, Vol. 7, Plenum Press, New York, 1963.

3. Rosenberg, D. L., and Wehner, G. K., "Darkening of Powdered Basalt by Simulated Solar-Wind Bombardment," Journal of Geophysical Research, Vol. 69, 1964, pp. 3307-3308.

N65-34971

F. X-RAY DIFFRACTION IN PLANETARY EXPLORATION

G. Otálora

Reliable data on the chemical constitution of the solar system are prerequisite for understanding the universe and for formulating hypotheses dealing with its origin. However, our present knowledge of its composition is fragmentary and leaves much to be desired.

Modern concepts that relate to the composition of the solar system derive from three principal sources: the makeup of Earth's crustal rocks, the study of meteorites, and spectral analysis of stellar radiation.

The rocks exposed on the Earth have well-known mineralogical and chemical characteristics, and it is believed that comparable rock systems will be found on other planets. Since meteorites are assumed to represent debris from a disintegrated Earth-like planet belonging to the solar system, they allow us to sample, in a hypothetical manner, the interior of such a planet. The presence of 66 of the 92 known elements in the Sun was established by spectral analysis, and valuable information on the nature of planetary atmospheres was also obtained; but spectroscopy can give us little quantitative information on composition of the planets, themselves.

The X-ray diffractometer is well suited to determine chemical identity of crystalline rocks, since each mineral component produces a characteristic diffraction pattern that is not altered by the presence of other minerals. By visual inspection or a programmed computer, it is possible to unscramble superposed patterns of crystal mixtures. It is also possible to measure relative abundance of minerals in a rock by comparing the intensity of selected reflections from the phases present.

Approximately 500 rocks have been examined to compare the mineralogy of the specimens with their respective X-ray patterns, and there is not great difficulty in the identification of the minerals present. Curves have been made to show the proportion of one mineral to another for the common rock-forming minerals that possibly occur on the Moon and terrestrial planets. Artificial samples with up to five minerals have been X-rayed to check the accuracy of the curves, which is better than ±10% for most combinations and under ideal conditions is within ±2%. Further refinements, such as measurement of cell dimensions, permit a fairly good approximation of the chemical composition of some mineral species.

In summary, X-ray diffraction techniques constitute the single most effective means for gathering data on the composition of the Moon and planets; from these data, it will be possible to postulate formative processes in the solar system.

NOMENCLATURE

NOMENCLATURE

a	divergence half-angle
CuK_α	copper X-radiation, K series, α lines
CuK_β	copper X-radiation, K series, β lines
d	interplanar spacing
(hkl)	Miller index of X-ray reflection
I_b	background intensity
I_p	total intensity
FeK_α	iron X-radiation, K series, α lines
MDL	minimum-detection limit
PHA	pulse-height analysis
sym	symmetry: The peak width at 1/2 peak minus background intensity is halved and the normal to this point extended down to a line whose width defines the resolution at 1/10 peak minus background intensity. Symmetry is then defined as the ratio of that segment of the line at higher angles to that segment at lower angles.
T	temperature
XRD	X-ray diffractometer
w/2	peak width at half maximum (deg-2θ)
w/10	peak width at one-tenth maximum (deg-2θ)
Z	atomic number
α	mass absorption coefficient
θ	Bragg angle
λ	wavelength
ρ	density (g/cc)